JOHANNES KEPLER
UNIVERSITÄT LINZ | JKU

TNF
Technisch-Naturwissenschaftliche
Fakultät

Interfacial effects in organic semiconductor heterojunctions

DISSERTATION

zur Erlangung des akademischen Grades

Doktor

im Doktoratsstudium der

Technischen Wissenschaften

Eingereicht von:
Philipp Stadler

Angefertigt am:
Institut für Physikalische Chemie

Beurteilung:
o. Univ. Prof. Mag. Dr. Dr. h.c. Niyazi Serdar Sariciftci (Betreuung)
Univ. Prof. Dr. Siegfried Bauer

Linz, Juli, 2011

Interfacial effects in organic semiconductor heterojunctions

PHILIPP STADLER
INSTITUTE FOR PHYSICAL CHEMISTRY

August 2011

Abstract

The field of organic electronics has systematically gained interest in recent years, technologically and scientifically advances have been made leading to practical applications such as organic light emitting diodes, organic field-effect transistors and organic photo-voltaic cells. In this thesis a fundamental study on organic molecules is presented targeting on interfacial effects at organic heterojunctions. Generally in organic electronic devices interfaces are considered as key parameters for achieving high performance applications. Therefore in this work the emphasis is to investigate layer-by-layer heterojunctions of organic molecules. Defined heterojunctions at inorganic III-V semiconductors form superlattices and quantum-wells, which lead to interfacial effects summarized as quantum confinement and two-dimensional electron gases. Although organic molecules differ in many aspects from their inorganic counterparts, similar effects can be theoretically expected at organic heterojunctions as well. Organic molecules form van-der-Waals type crystals and domains which are macroscopically anisotropic and polycrystalline or amorphous. Organic molecules are intrinsic semiconductors and at interfaces dipoles are formed, which control the energy level alignment. In order to characterize such structures and compare them to inorganic superlattices and quantum-wells it is necessary to induce charge carriers. In this work this is established either by interfacial doping using high-performance dielectrics in a field-effect transistor structure or by photo-doping by exciting a donor-acceptor bilayer. In both cases C_{60} was chosen as organic semiconductor exhibiting good acceptor properties and an electron mobility in the range of $0.5\,\mathrm{cm}^2\,\mathrm{V}^{-1}\,\mathrm{s}^{-1}$. The fabrication of well-defined few-molecular layers allows probing directly at the interface. Spectroscopic methods and transport measurements are applied for characterization: Photoemission spectroscopy, absorption and photo-induced absorption spectroscopy and light-induced electron spin resonance as well as current-voltage transport characteristics of field-effect transistor structures. The structure and the morphology were characterized by atomic force microscopy and transmission electron microscopy. The results presented show that at organic heterojunctions interfacial dipoles are formed. The origin and magnitude as well as the influence of the dipoles is discussed based on in-situ experiments during doping. It is concluded that dipoles control the energy level alignment at the interface. At high doping levels indications of band-like transport and quantum confinement are found.

Zusammenfassung

Im Bereich der organischen Halbleiter-Elektronik wurden in den letzten Jahren systematisch Fortschritte gemacht, sowohl auf der technologischen als auch auf der wissenschaftlichen Seite. Praktische Anwendungen wie organische Licht emittierende Dioden und organische photovoltaische Zellen sind in vielfältigen Anwendungsbereichen am Markt. In dieser Doktorarbeit wird eine profunde Studie organischer Moleküle präsentiert, die auf Grenzschichteffekte an organischen Heterostrukturen abzielt. Generell werden in organischen Elektronik - Schaltkreisen Grenzschichten als die Schlüsselparameter gesehen, deren Optimierung zu Hochleistungsanwendungen führt. Diese Arbeit legt daher den Schwerpunkt auf die Charakterisierung von schicht- weise aufgetragenen Heterostrukturen organischer Moleküle. In anorganischen III-V Halbleiter - Heterostrukturen werden Supergitter and Quantum Wells geformt, die zu Quantum - Confinement und 2D - Effekten führen. Obwohl sich organische Halbleiter in vielen Aspekten von anorganischen Systemen unter-scheiden, kann man ähnliche Effekte erwarten. Organische Halbleiter bilden van-der-Waals Kristalle oder Domänen aus, die makro- skopisch gesehen anisotrope Eigenschaften haben. Weiters sind sie intrinsische, undotierte Halbleiter. Um diese Strukturen genau zu charakterisieren und mit anorganischen Systemen zu vergleichen, ist es notwenig Ladungsträger zu injizieren. In dieser Arbeit wird dies sowohl mit Grenzschichtdotierung, wobei hochisolierende Dielektrika in Feldeffekttransistor - Strukturen verwendet werden, als auch mit Photodotierung ermöglicht. Hier werden Donor - Akzeptor Doppelschichten mittels Laser angeregt. In beiden Fällen wird C_{60} als Halbleitermolekül untersucht, nachdem es sich mit guten Akzeptor - Eigenschaften auszeichnet und eine hohe Ladungsträgermobilität im Bereich von $0.5\,\mathrm{cm^2\,V^{-1}\,s^{-1}}$ aufweist. Die Herstellung von definierten Schichten mit Dicken in Dimensionen der Moleküllänge erlaubt die Charakterisierung direkt an der Grenzschicht. Spektroskopische Methoden und Transportmessungen werden für die Untersuchung angewendet. Darunter fallen Photoemissionsspektroskopie, (photoinduzierte) Absorptionsspektroskopie sowie Transportmessungen in Feldeffekt Transistoren.

Die Struktur und die Morphologie wurden mittel Atomkraftmikroskopie und Transmissionselektronenmikroskopie untersucht. Die Resultate der Arbeit zeigen, dass sich an den organischen Heterostrukturen Grenzschichtdipole ausbilden. Die Ursache und das quantitative Ausmaß sowie der Einfluß der Dipole wird diskutiert basierend auf in-situ spektroskopischen Experimenten beim Dotiervorgang.

Die Schlußfolgerung der Resultate ergibt, dass Dipole die Energieangleichung an der Grenzschicht kontrollieren. Bei hohen Ladungsträgerkonzentrationen gibt es Indikationen für Bandtransport und Quantum - Confinement.

Contents

Acknowledgements

Foremost I thank Professor Niyazi Serdar Sariciftci for his supervision during the past years. Thank you for your generosity and your scientific supervision.

I thank my co-supervisors Gebhard ”Gebi” Matt for your ideas, creativity and support, Helmut Neugebauer for your open ears and scientific discussions and Siegfried Bauer for your assistance and scientific input.

I thank all (former) members of LIOS for fruitful discussions, collaboration and nice time together. I had collaboration and joined projects with many people coming an going in the past years. I especially name Birendra Singh, for motivating me to join LIOS and for companionship during my first years in academia. Special thanks is given to Eric Glowacki for ESR-measurements, Jacek Gasiorowski for help in device characterization, Mateusz Bednorz for FTIR-support, Almantas Pivrikas for support in transport measurements, Beatriz Meana-Esteban for help in electrochemistry and Stefan Schaur for ”mastering” me in advanced writing in Latex.

Special thanks go to Petra Neumaier, Gerad Kalab and Birgit Paulik for administrative assistance and Manfred Lipp for your excellent technical assistance.

I show my appreciation to my diploma students Stefan Schaur, Sandra Kogler and Stefanie Schlager. Thanks for your patience with me.

I am very grateful to the SOMAP-team for the mutual collaboration, for your rich idea&cookie-pool, critical reflexions and scientific discussions.

I thank the epitaxy-group of Professor Helmut Sitter and co-workers in the institute for solid state physics for the support.

I thank the surface-group at Graz University: Professor Mike Ramsey, Georg Koller, Hannes Offenbacher and Anna Track for the fruitful collaboration. Same applies to Professor Lang, Thomas Penz and Markus Sauer in the faculty of physics at Vienna University.

Last but not least I thank my family and especially Petra for your permanent support, patience and understanding.

Motivation

Interfacial effects at organic heterojunctions represent very general termini for a number of quantum-mechanical or wave-mechanical effects at semiconductor interfaces. Particularly interesting are quantum wells structures and superlattices. All these semiconductor heterostructures have an enormous impact to the development of high-performance optoelectronic devices.

The motivation in this work is to replace conventional inorganic III-V systems by organic π-conjugated molecules. The class of organic semiconductors differ in some aspects from their inorganic counterparts. It is particularly challenging to create strategies for organic quantum wells and superlattices and to investigate their electronic properties. The question arises, if organic molecules will behave similar in terms of wave mechanics.

Novel techniques are necessary to fabricate few-molecular layers and well-ordered and defined systems. In-situ spectroscopic techniques are developed for characterizing the interfaces in organic-organic molecular systems. The author believes that a fundamental understanding of interfaces brings organic semiconductors closer to high-performance applications.

Chapter 1

Introduction

Heterojunctions are investigated in organic semiconductor in donor-acceptor systems both bilayers and alternating stacked layers and in thin films on a dielectric in a field-effect transistor structure. In both cases the target is to introduce charge carriers either by photo-excitation or by electrical field-effect doping.

The final aim is to probe few-layer films of organic molecules grown on the dielectric insulator for an organic field-effect transistor and on the dye for a bilayer or alternating stacked layers at the interface.

1.1 Semiconductor heterojunctions

Classic heterojunctions are applied in III-IV compounds from inorganic semiconductors. The fundamental properties is depicted in figure 1.1.

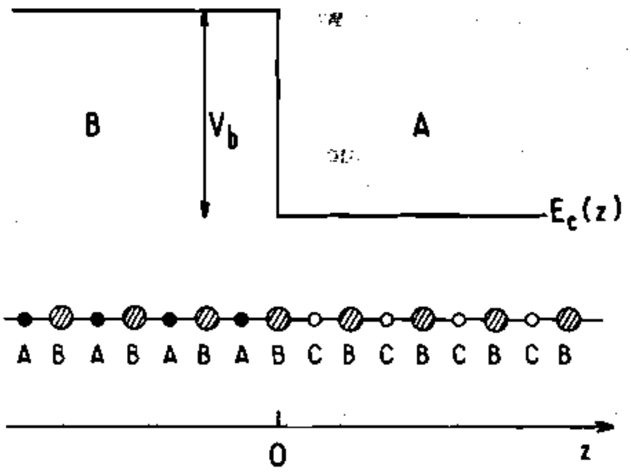

Figure 1.1: 1D sketch of heterojunction formed between two lattice matched A and B semiconductors. Note unterneath the chemical formulae CB and AB. The upper part shows the band edge as function of z-axis. Lower part shows the actual bonds. Figure courtesy of Bastard [1].

At the band edge the energy offset V_b between compound A-B perpendicular to the interface plane (z) is shown (A-B structure). Underneath an ideal semiconductor structure is depicted. At the heterostructure a A-B-C bond is formed. Advanced epitaxial techniques allow the growth of such well-defined junctions in the atomic scale.

Theoretically this picture can be adapted for organic molecules too, e.g. for two different π-conjugated molecules. Here the lattice-match aspect ceases to exist, anyhow the picture can be considered a model system for organics is a first approximation. For the organic heterojunctions the A-B structure is revealed in an organic field-effect transistor or for a simple donor-acceptor structure. The heterojunction model is extended, when alternating layers of semiconductors are deposited. The simplest case represents a A-B-A type structure, forming different heterostructures plotted in figure 1.2. Type I heterostructures (a) form a quantum well for electrons and barrier for holes, which best fits later to presented organic systems. Type II structures address a confinement for both type of carriers for light-emission. Both systems, type A-B and type A-B-A will be studied in this thesis.

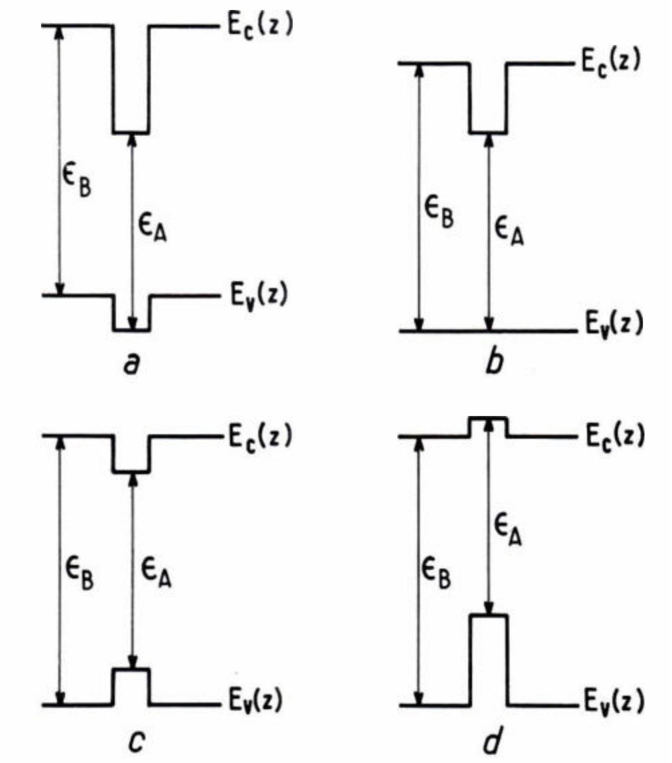

Figure 1.2: Types of semiconductor quantum wells: (a) electrons are confined in A, holes in B. (b) Same as (a) without barrier for holes. (c) Both electrons and holes are confined in A. (d) Inverse quantum well as for (a). Figure courtesy of Bastard [1].

In theory electrons are confined within the barriers V_b (particle in the box).

$$k_w L = \pi p \tag{1.1}$$

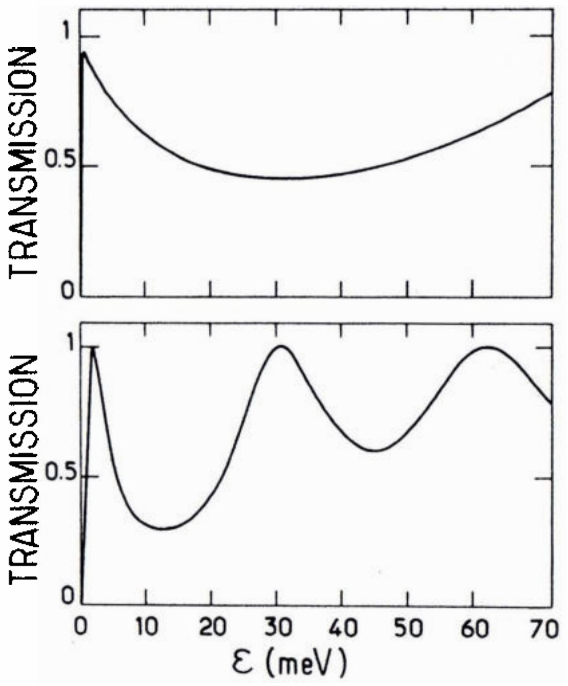

Figure 1.3: Energy dependence of the transmission coefficient $T(\varepsilon)$ in a square quantum well of thickness L=25 nm with tow different energy barriers (top V$_b$=224 meV and bottom V$_b$=150 meV). Figure courtesy of Bastard [1].

Energy levels are a function of the box length L described by the formular for a particle in a box, see equation 1.1, where p is an integer number and k_w the wave-vector propagating within the well. The solution of the wave mechanics reveals constructive interferences, whose discrete energies are called transmission resonances. In well-defined inorganic quantum well structures such features are found in the far and mid infrared, an example is given in figure 1.3.

$$k_w = \sqrt{\frac{2m*}{\hbar^2}\left(\varepsilon + V_b\right)} \tag{1.2}$$

More complex are supperlattice-systems, which ideally represent an infinite sequence of quantum wells. A schematic of a supperlattic of type I heterostructures is presented in figure 1.4. Due to the continuity the wave function in z-direction is changed and discrete energy levels - Bloch states - arise. The energy for the features are limited within the borders of the barrier V_b.

The solution for a III-V semiconductor system is graphically presented in figure 1.5, where actually allowed solutions of the Bloch states are found between $F(\varepsilon) = \pm 1$.

As presented the solutions of wave mechanics of inorganic systems are well developed. In the next chapters organic heterojunctions are checked for similar quantum effects in defined heterostructure systems.

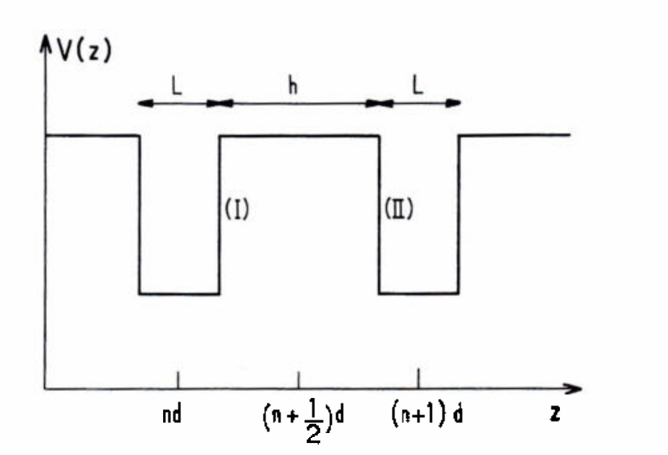

Figure 1.4: Schematic of a superlattice potential energy profile. Just a segment of 2 quantum wells is shown. Figure courtesy of Bastard [1].

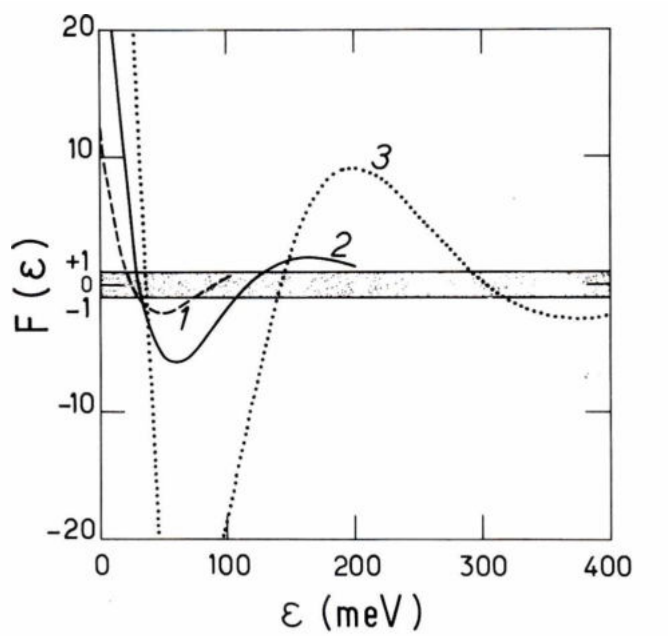

Figure 1.5: Bloch states in idealized superlattice. Three different barrier heights V_b at 100 meV (dashed), at 200 meV (solid) and at 400 meV (dotted) are considered. The discrete energy ε_{qn} for the Bloch wave equation F(ε) is found within the height V_b and 0. The shaded area corresponds to the allowed superlattice states. Figure courtesy of Bastard [1].

1.2 Organic semiconductor molecules for heterojunctions

1.2.1 C_{60}

Fullerenes and especially C_{60} has gained a lot of interest after its discovery by Kroto et al. [2] in 1985. Fullerene is an elementary form of carbon, the structure with the outrangous symmetry named after the artwork of the architect R. Buckminster Fuller leads to unique electronic properties. A vivid picture of an unfolded fullerene has been drawn by Albrecht Dürer (figure 1.6, left). Pentagons are surrounded with hexagons - it belongs to the group of truncated icosahedrons, or more general to the Archimedean solids consisting of at least two different polygons.

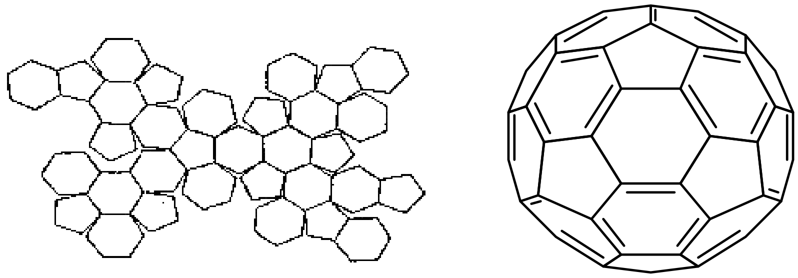

Figure 1.6: Left: Drawing of the "icosahedron trunctum". Courtesy of Albrecht Dürer (around 1500 a.c.). Right: Structure of the C_{60} molecule

The molecular structure is depicted in figure 1.6, right. In carbon-related semiconductor terminology C_{60} is called the zero-dimensional allotrope of sp^2-hybridized carbon, (consequently followed by one-dimensional carbon nanotubes, two-dimensional graphene and three-dimensional graphite).

As an introduction to the electronic structure serves the optical absorption of a solid film presented in figure 1.7. Three characteristic bands arise at 2 eV, 2.75 eV and at 3.54 eV. Further parameters are profoundly discussed by Troullier and Martins [3], Lu et al. [4], Maxwell [5], Ruckman et al. [6] , the band-gap of C_{60} is e.g. 2.4-3.0 eV with the absorption edge at 1.7 eV and the ionization potential of the solid film at 6.5-6.9 eV.

In organic semiconductors C_{60} is considered as the n-type semiconductor transporting electrons. Hole transport has not been observed. Fullerenes can be doped by diverse methods, in particular the C_{60} molecule can be reduced (n-doped) up to six times. Usually chemical doping is performed by reduction with alkali and alkali-earth metals. Both pristine as well as doped fullerenes have been intensively investigated. Alkali-fullerides show metal-like behavior, at higher alkali-metal concentrations Me_xC_{60} (x= 1-6) semiconductors and superconductors are found [7]. By applying electrochemical doping of fullerene solid films up to five reduction peaks are reported in the literature [8, 9]. At interfaces to organic dyes such as π-conjugated polymers (poly-(paraphelylidene) and poly-(alkylthiophene)) or dye

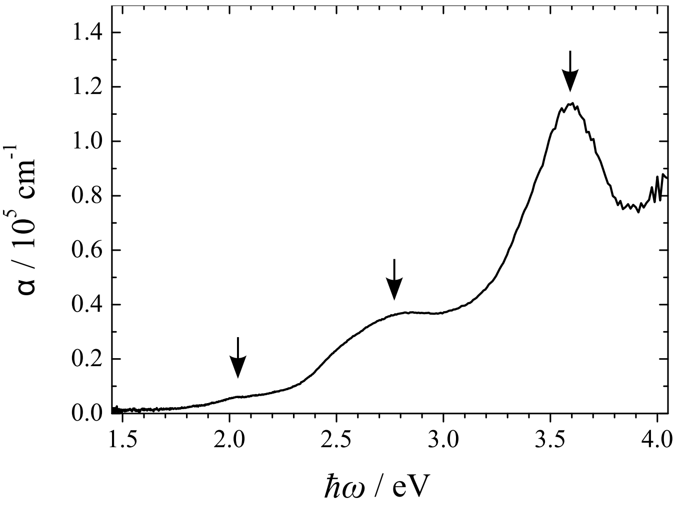

Figure 1.7: Absorption spectra of 15 nm solid film of C_{60}

molecules such as metal-phthalocyanines C_{60} acts as electron acceptor under the illumination with visible light. Sariciftci et al. [10] show the photo-induced electron transfer from a PPV-derivative to the C_{60}. An electron-hole pair is formed at the heterojunction. In fullerene-dye composites photoconductivity and photovoltaic effect is observed [11]. Fullerenes and its derivatives are utilized as electron acceptor molecules in organic heterojunction blends for organic photovoltaic devices (OPV) [12].

Another method to introduce charge carriers is interfacial doping in an organic field-effect structure. OFETs and integrated circuits based on epitaxial grown fullerene exhibiting high electron mobilities have been demonstrated by Anthopoulos et al. [13]. Depending on the morphology of the thin films grown, the values for the mobility of C_{60} vary between 0.1 to $5\,\mathrm{cm^2V^{-1}s^{-1}}$ [14, 15]. In particular photo-doping and interfacial doping of fullerene will be discussed in detail in this work.

1.2.2 Zinc-Phthalocyanine

Here zinc-phthalocyanine is used as the organic donor molecule (dye) in combination with C_{60}. The molecular structure of zinc-phthalocyanine (ZnPc) is depicted in figure 1.8.

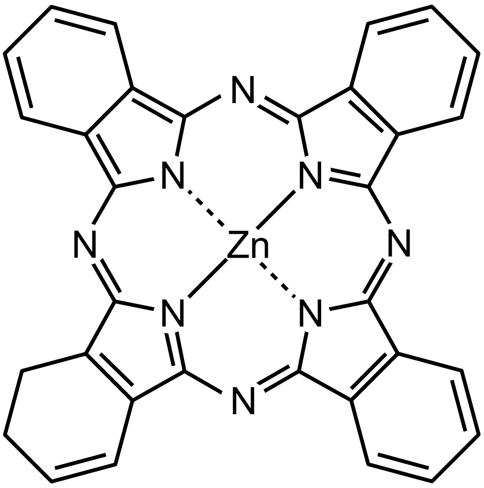

Figure 1.8: Molecular structure of zinc-phthalocyanine.

The metal-organic complex has a planar structure. In this work zinc was used as central atom. ZnPc is used as dye in bilayer heterojunctions.

The absorption in the UV-Vis of a solid thin film on glass is shown in figure 1.9. Characteristic for this molecular family are the intense and well-resolved Q-bands ($\pi - \pi^*$ transition) at 1.75 eV and 1.98 eV and series of bands at higher energies at 3.65 eV of porphyrine ligands. Differently from fullerene the Q-band is found at lower energies. In combination both molecules cover a representative part of the sun spectra. The optical and electrical properties of ZnPc gained interest for implementation to organic photovoltaic devices. One of the first demonstration of a phthalocyanine-based photovoltaic cell is presented by Tang [16] in 1986. The unwaning interest in metal-phthalocyanines emerge from the variety of different central metals for expanding the absorption profile to the near infrared and the efficient charge transfer to fullerene [17].

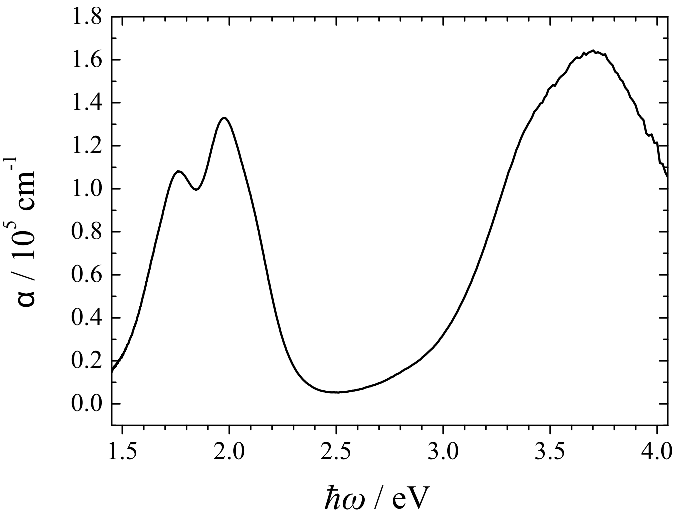

Figure 1.9: Absorption spectra of 15 nm solid film of ZnPc on glass.

1.3 Donor-acceptor type heterojunctions

Donor and acceptor molecular layers are deposited in a stacked layer-by-layer structure. As introduced above two π-conjugated molecules, here ZnPc (acceptor) and C_{60}, are applied. During photo-excitation doping effects are probed at A-B and A-B-A (and multiple) type heterojunctions. A schematic description of the heterojunction and the photo-doping is illustrated in figure 1.10.

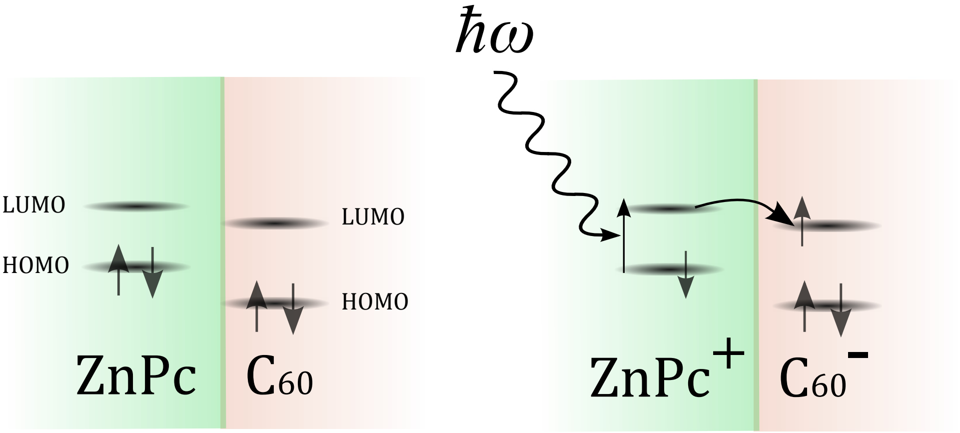

Figure 1.10: Schematic donor-acceptor junction (ZnPc-fullerene). The ZnPc is excited followed by an charge transfer to the fullerene. An electron-hole pair is formed.

The energy levels of the electron donor lie higher than the levels of the acceptor. The difference in the energy levels enables charge transfer. When selectively exciting the donor molecule, electrons are transfered within the LUMOs. The photo-excitation is performed using a pump energy at around 2 eV, which coincides with the absorption maximum of the ZnPc. The corresponding absorption spectra for ZnPc and C_{60} and the excitation energy are depicted in figure 1.11. Multiple layer structures and bilayers are then characterized in-situ during continuous-wave (cw) photo-excitation.

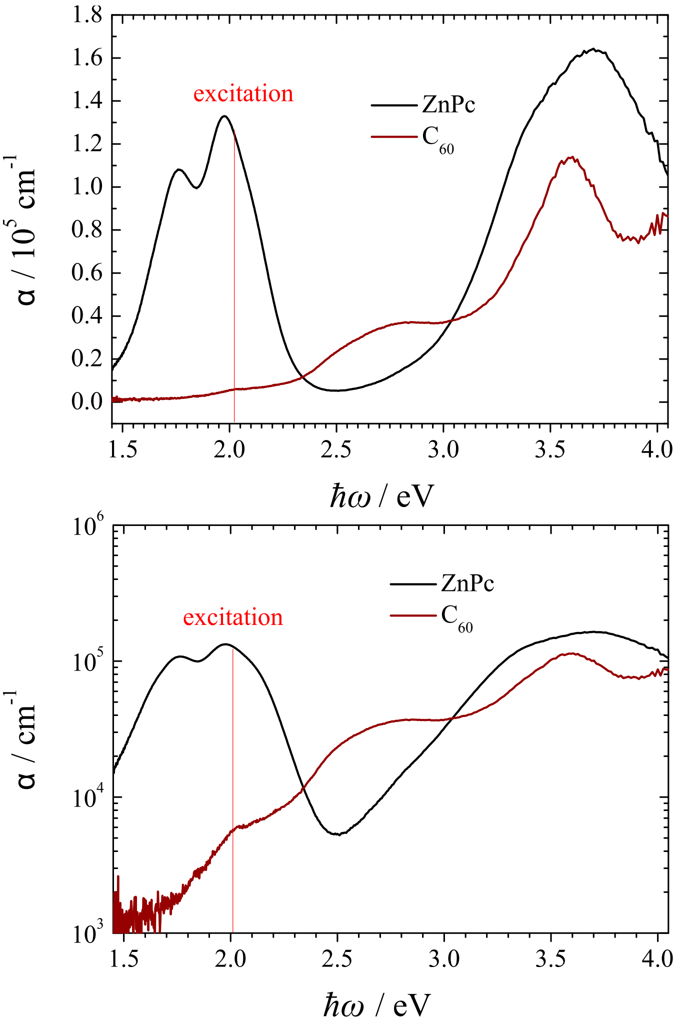

Figure 1.11: Top: Absorption spectra of ZnPc and C_{60}. Bottom: Semilogarithmic plot of absorption. The red line indicates the pump energy selectively exciting ZnPc at the Q-band maximum.

1.4 Heterojunctions in an organic field effect transistor

Another approach to inject charge carriers to an organic system at an organic A-B type heterojunction represents interfacial or electrical-field doping [18]. Here the heterojunction is formed between an insulating layer (dielectric) and the organic semiconductor viz C_{60}. Interfacial doping is enabled using an organic field effect transistor (OFET) device structure, see figure 1.12

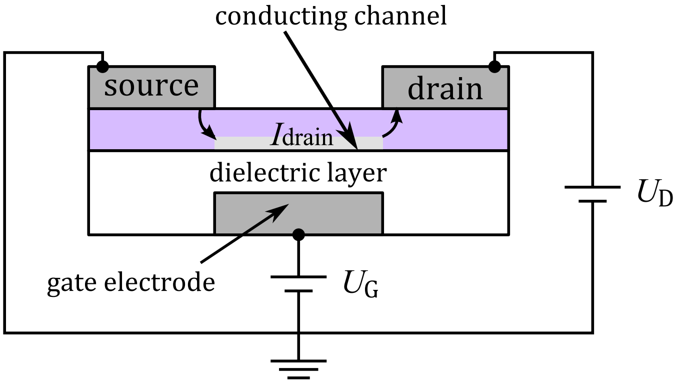

Figure 1.12: Simple schematic of an OFET consisting of source and drain contacts, organic semiconductor with the conductive channel indicated and dielectric insulator. It separates the gate electrode from the channel. Gate and drain voltages (U_g and U_d) are applied using common ground.

A schematic of the operation principle is shown in figure 1.4. The gate voltage is determining the energy levels of the organic semiconductor. Either holes or electrons are transported from source to drain, then gate voltages are applied with respect to the source electrode. OFETs operate in the accumulation regime, which means that the semiconductor is a priori intrinsic.

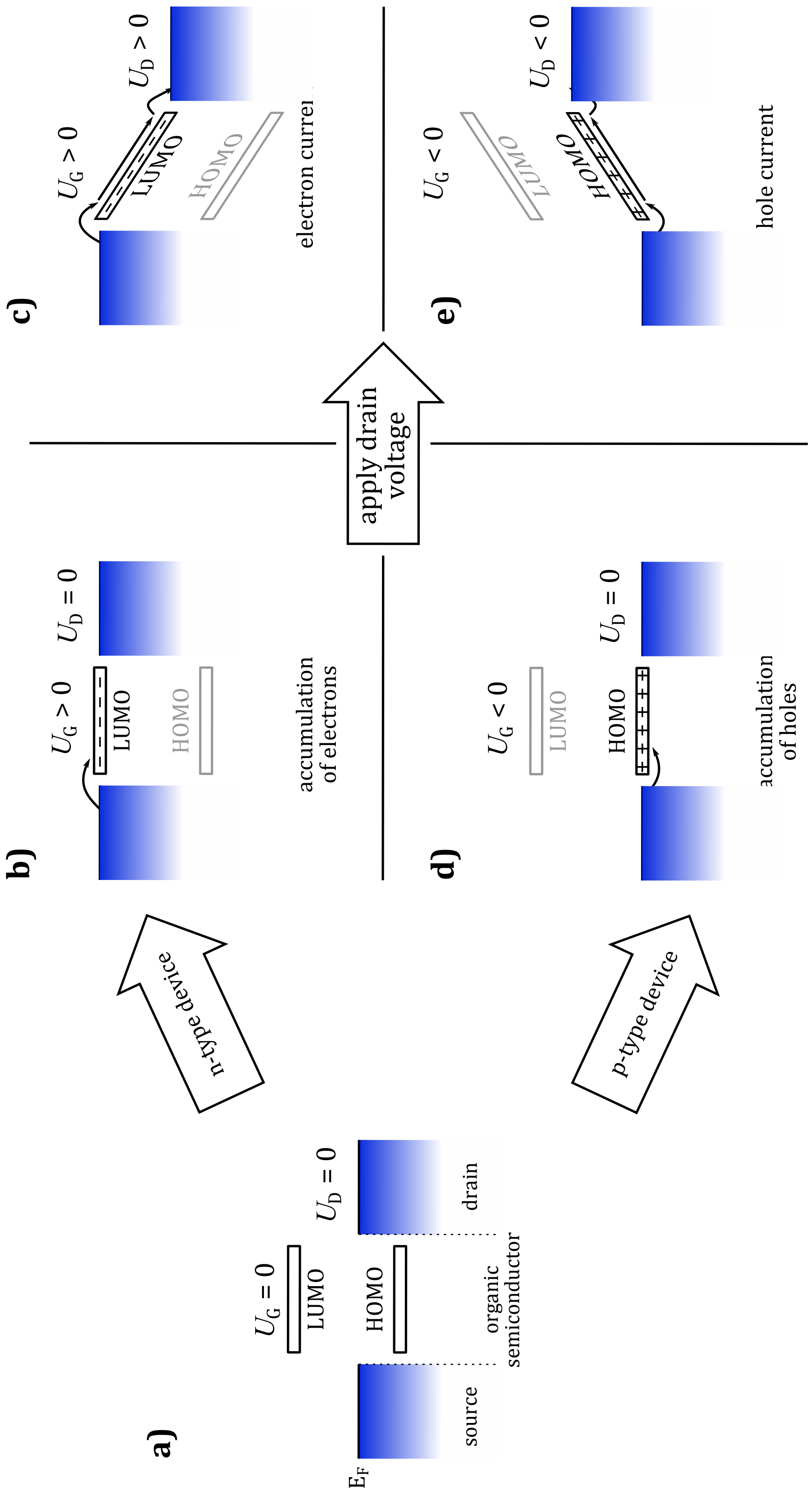
a)
E_F
source
$U_G = 0$
LUMO
HOMO
organic semiconductor
$U_D = 0$
drain
n-type device
p-type device
b)
$U_G > 0$
LUMO
HOMO
$U_D = 0$
accumulation of electrons
c)
$U_G > 0$
LUMO
HOMO
$U_D > 0$
electron current
apply drain voltage
d)
$U_G < 0$
LUMO
HOMO
$U_D = 0$
accumulation of holes
e)
$U_G < 0$
LUMO
HOMO
$U_D < 0$
hole current

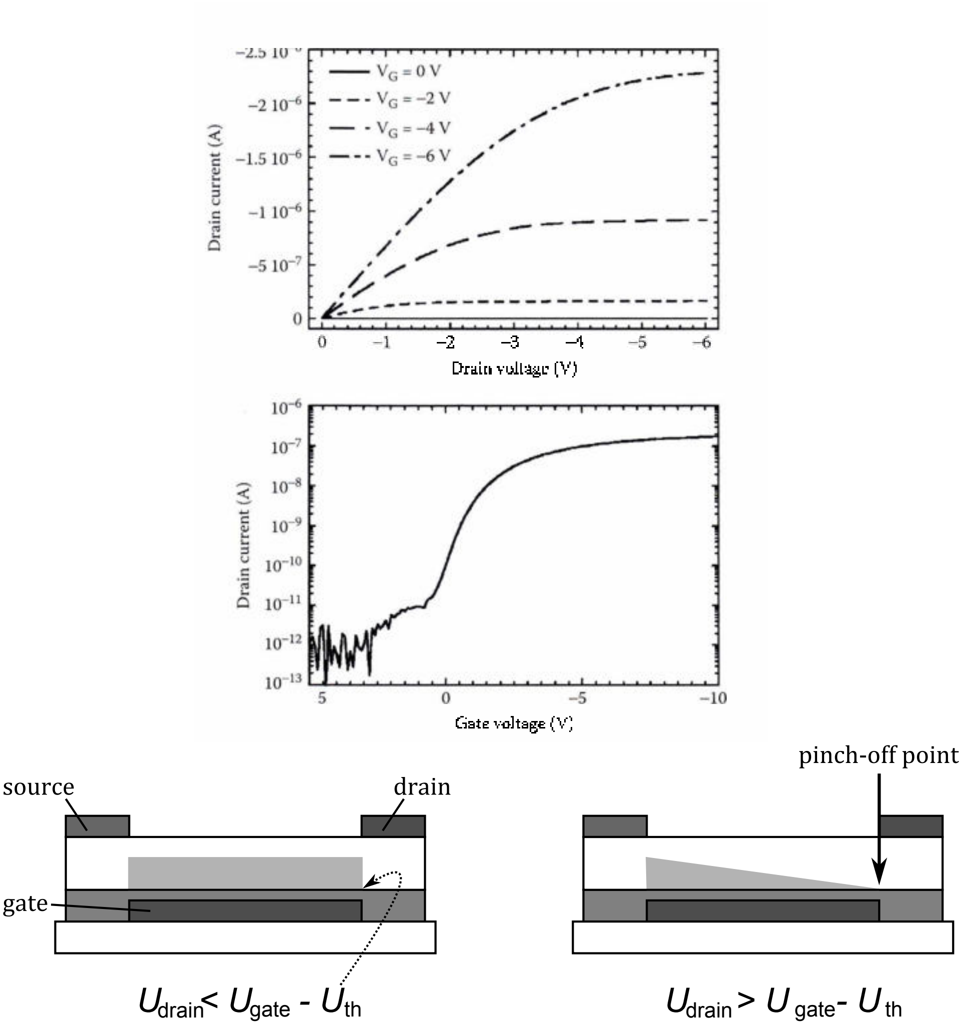

a) linear regime

b) saturated regime

Figure 1.13: Previous page: Energy levels (schematically) during transistor operation: (a) depicts the intrinsic case without gate voltage applied, electrons are accumulated (b) and transported (c) at positive gate voltages ($U_g > 0$). Opposite gate voltages ($U_g < 0$) leads to hole accumulation (d) and transport (e). Current page, top: A typcial output (uppermost) and transport (underneath) current-voltage characteristics of a OFET. Note the saturation in the uppermost output curves. The tranfer characteristics show the depletion and accumulation regime. . Current page, bottom: Along the OFET channel the linear regime (a) reveals a homogeneous and the saturated regime a non-homogeneous (b) field distribution. Figures courtesy of Horowitz [19, 20].

Typical transistor current-voltage characteristics and the field distribution in the conductive channel during accumulation are depicted in figure 1.13. The output curve shows that the current saturates after reaching a pinch-off point. Note the concomitant schematic on the bottom, showing the field distribution in the channel: At low source-drain voltages the channel is not really affected, the situation changes at high drain voltages greater than the gate voltage with respect to source. The channel is pinched off and a depletion zone builds up adjacent to the drain electrode. The center graph illustrates a transfer characteristic. When following the current from depletion (left) to higher gate voltages the transistor switches to accumulation mode. There are four different OFET geometries, which are schematically depicted in figure 1.14. They are divided in staggered structures (a) and (c), where the source-drain contacts are facing only the organic semiconductor. In a coplanar geometry (b) and (d) source-drain contacts are facing both the insulator dielectric and the semiconductor. Both structures exist in a top-gate and bottom-gate geometry [21]. In this work, preferentially the staggered bottom-gate, top-contact structure is applied for characterization. This geometry is adapted to the fabrication method using a metal-metaloxide system.

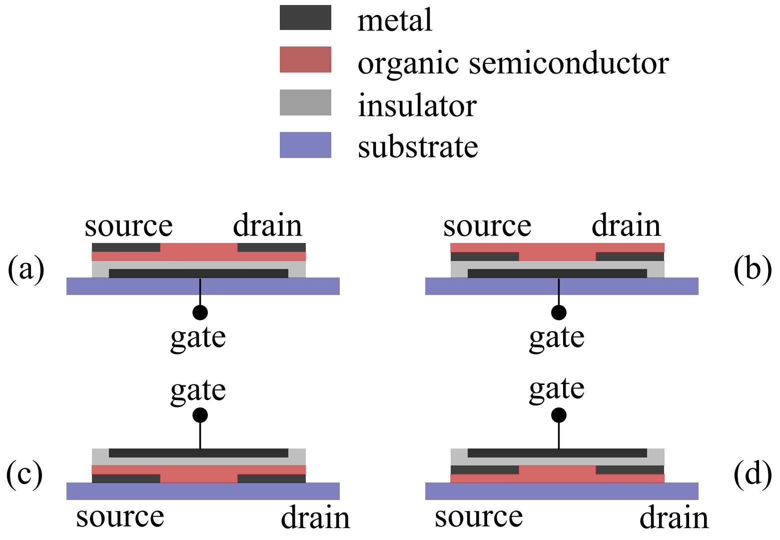

Figure 1.14: (a) Bottom-gate top contact (staggered) and (b) bottom-gate bottom-contact (coplanar) OFET geometries. (c) and (d) represent the corresponding inverted top-gate structures.

The material choice for the organic field effect transistor is crucial, especially all considerations target on the design of the right interface between the organic semiconductor and the dielectric layer. As introduced in section 1.2.1 C_{60} is chosen as semiconductor, therefore the dielectric is adapted for a good alignment.

Two aspects are important regarding dielectric insulators for OFET: It shall have a high dielectric constant ε, the layer shall be as thin as possible and withstand huge electric fields. Materials with dielectric constants greater than $\varepsilon <$ 6 are considered as high-ε dielectrics. The desired geometric capacitance of a high-performance insulator is usually in the range of several $100\,\mathrm{nF\,cm^{-2}}$ with breakdown-fields above 400-500 $\mathrm{V\,\mu m^{-1}}$. The second issue concerns the energy level alignment at the interface with the organic semiconductor, which plays a major role for the final device performance [22]. There are different options to fulfill both requirements. A way to proceed is to combine metal oxides with organic interlayers for a hybrid dielectric structure, see figure 1.15.

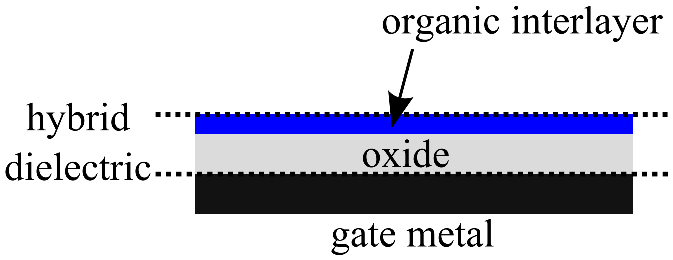

Figure 1.15: Sketch of commonly used hybrid dielectric structure combining inorganic oxides with organic thin films.

Frequently applied examples for hybrid dielectrics combine oxides from valve metals or silicon silicon dioxide and organic layers. The related OFET structures are depicted in figure1.16.

For the interlayer, various organic materials are used. The scope ranges from classical polymeric thin films [21, 23], crosslinkable resins [24, 25] and vapor-deposited small molecules [26–28] to mono-molecular layers of self-assembled molecules (SAMs) [29–32]. In figure 1.17 and 1.18 a number of candidates are presented.

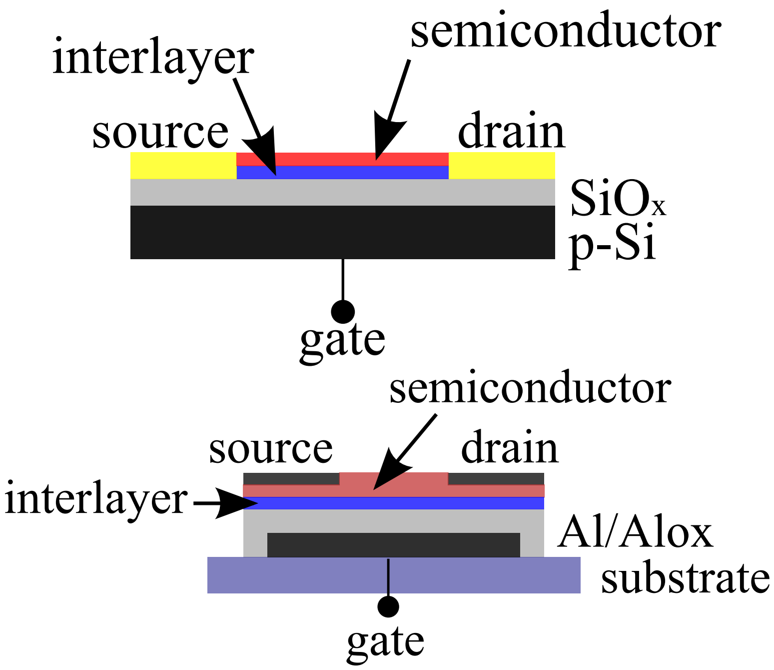

Figure 1.16: Dominant OFET structures used in literature. Right: Schematic of frequently adapted coplanar structured OFET using doped silicon as gate electrode (and as substrate) with thermally grown SiO_2 as insulator. Left: Anodic grown oxide film on a valve metal (here aluminum) directly used in a bottom-gate OFET structure. Note in both cases the organic interlayer applied on top for a combined double layer or hybrid dielectric. The organic semiconductor is deposited on top of the interlayer forming a favorable interface.

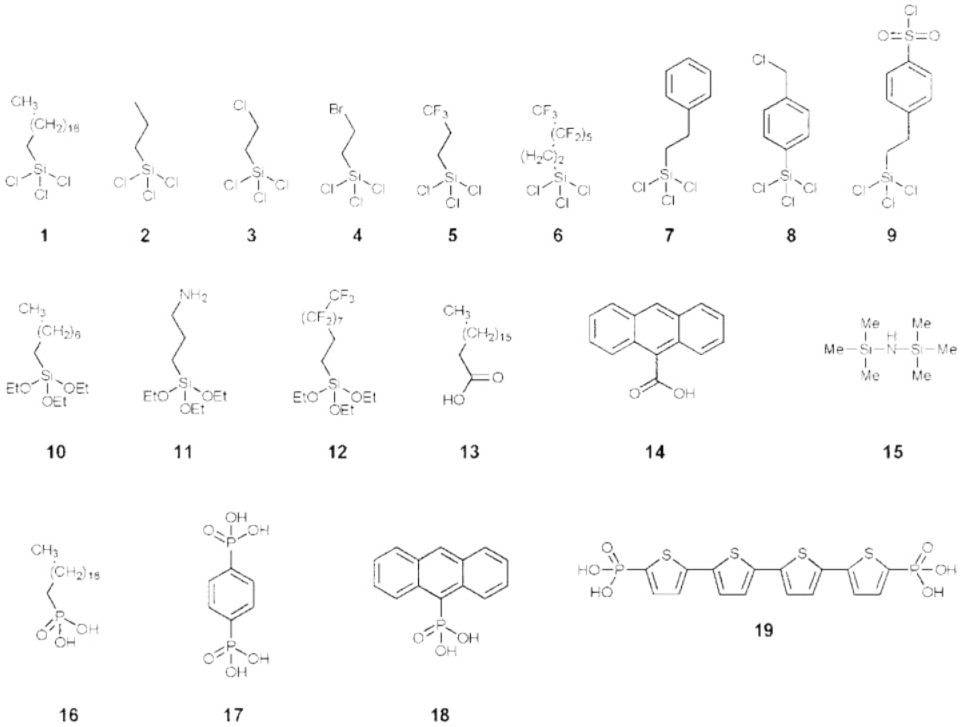

Figure 1.17: Examples of SAM-molecules with different anchoring functionalized groups: Trichlorosilanes (1-9), triethoxysilanes (10-12), carboxylic acids (13,14), hexamethyl-disilazane (HMDS, 15) and phosphonic acids (16-19). Most commonly used compound 1 is known as OTS (octadecyl-trichlorosilane). Figure courtesy of Miozzo et al. [32].

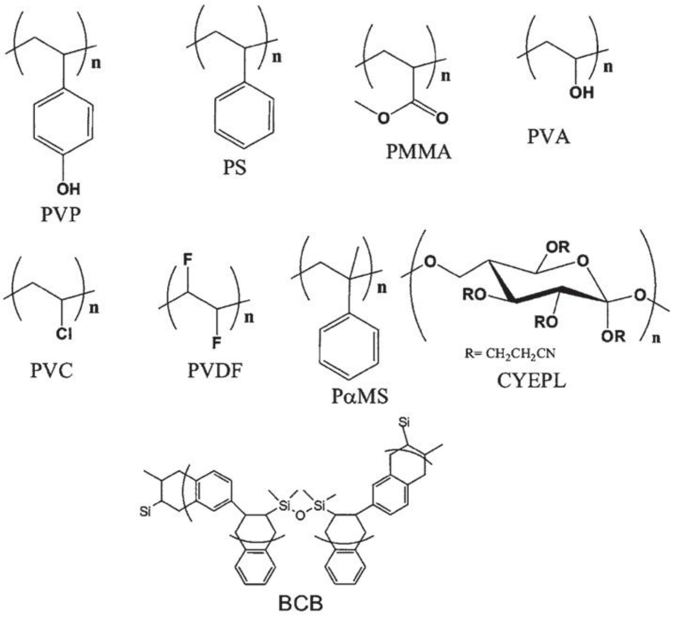

Figure 1.18: Various polymers and resins used for high-performance OFETs. Figure courtesy of Singh and Sariciftci [21].

Chapter 2

Experimental procedures and studies

The experimental chapter describes methods to fabricate well-defined organic-organic heterostructures. They are dedicated to a certain probing technique to characterize electronic properties, which involves means of spectroscopy (sample part) and charge transport measurements (device part). The properties of the heterostructures are controlled by choosing different substrates and different conditions. All materials involved and all techniques applied are described in detail including steps prior the fabrication such as purification treatment and basic material data too.

2.1 Sample preparation

Organic heterojunctions were fabricated by phycial vapor deposition (PVD) at high vacuum, typically at 10^{-7} mbar (Leybold Univex 350 evaporation system). The substrate temperature during deposition was set at 80 K for homogeneous covering. Samples structures and devices are patterned in order to avoid edge effects. Steel shadow masks for metal and organics layers were designed. Metals are deposited in high vacuum (typically at 10^{-6}mbar), which is integrated into a inert gas system with an oxygen- and moisture-free nitrogen atmosphere.

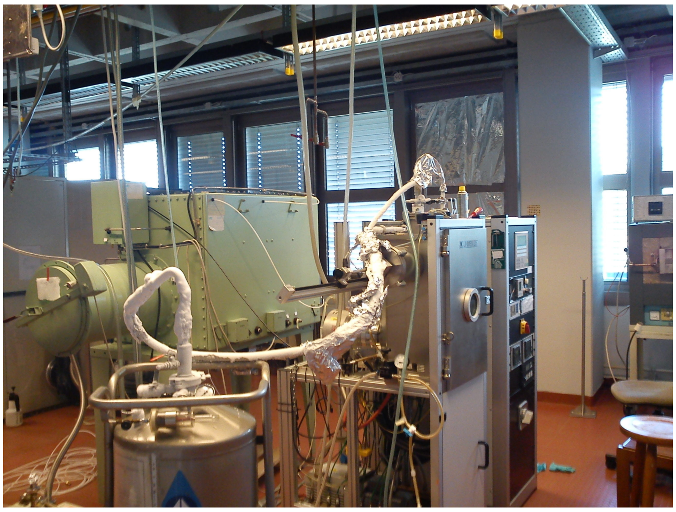

Figure 2.1: Liquid nitrogen cooled substrate holder of PVD high-vaccum system from Leybold.

The organic semiconductors used are purified before thermal evaporation in a re-sublimation step in vacuum (10^{-3} mbar). For C_{60} temperatures around 400 °C are used, the material is sublimated and condensed in a quartz tube. ZnPc is sublimated at slightly lower vacuum (10^{-2} mbar) and at constant nitrogen flow.

C_{60} and ZnPc are evaporated then in vacuum system at $3{\cdot}10^{-7}$mbar pressure. The substrate temperature is controlled before and during the deposition of the organic layer. First, substrates are annealed in the high vacuum several hours. Straight before starting the vacuum deposition the substrate holder is constantly flushed with liquid nitrogen, unless the temperature reaches 80 K. The temperature is controlled using two thermocouples attached on the holder and next to the substrates respectively. The deposition rate is kept constant at $0.5\,\text{Å}\,\text{s}^{-1}$ for both materials. Materials are evaporated then from a quartz crucible in the high vacuum system at around 400 °C in case of C_{60} and 350 °C in case of ZnPc. The evaporation rate is controlled using a calibrated microbalance, the parameters set as followed:

material	C_{60}	ZnPc
density / kg m^{-3}	1.55	1.23
sublimation temperature / K	400	350

Information about organic films grown at 80 K was obtained by cross-section TEM measurements (2.1.1). The homogeneity of few-nm thin films is *the* key requirement for probing interfacial effects.

2.1.1 Photoemission spectroscopy

All films involved for photoemission experiments are prepared ex-situ (outside the ultra high vacuum (UHV) in the photoemission setup). The experiments are performed using a PHOBIOS specs analyzer and He (I) UV lamp (21.2 eV) for UPS and Mg-K_α X-rays (1 253 eV) for XPS. After loading the sample and storing in UHV overnight the surfaces are characterized layer by layer.

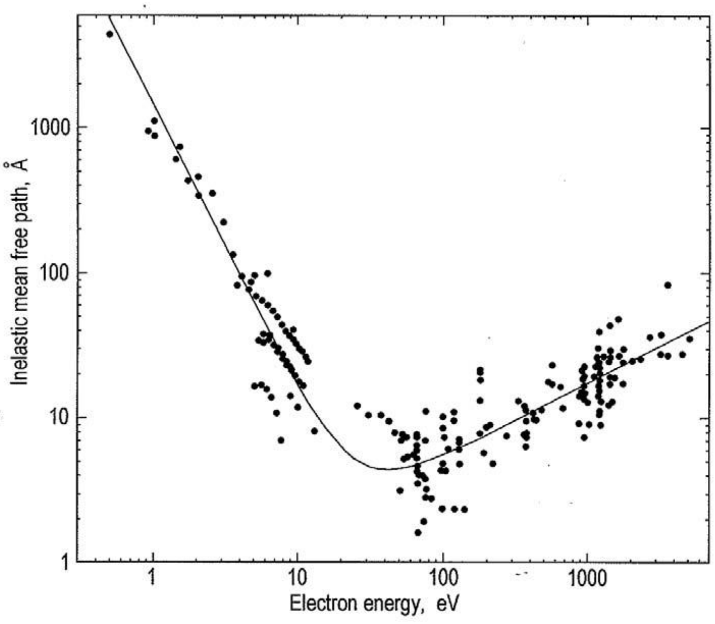

Figure 2.2: Inelastic mean free path as a function of the electron energy. At 21.2 eV He(I) (UPS) the path length is close to the minimum and slightly increased for X-rays at 1253.6 eV Mg-K_α (XPS). Graph taken from Oura et al. [33]

High-quality films are required, which are deposited as described in section 2.1. The target here is to probe the semiconductor close to interface of the hetero-junction, therefore the layer thickness is reduced. Practically the C_{60} films must not exceed 30 Å, which corresponds to a maximum of 3-4 molecular layers: Seen in figure 2.2 the inelastic mean free path for ultraviolet (He (I) lamp excites at 21.2 eV) hardly exceeds 10-20 Å. The surface sensitivity is slightly increased for X-ray photoemission spectroscopy using Mg-K_α radiation at 1253.6 eV. The thickness of the investigated C_{60} layer is measured with cross-section TEM. Fullerene´s unique structure offers an advantage, as the TEM reveals its structure quite distinctive. Sandwiched between samarium (black) and BCB (white) the elementary carbon layer hardly exceeds three layers (see figure 2.3), which is sufficient for the interface study.

In the first step, the quality and electronic properties of each layer is investi-

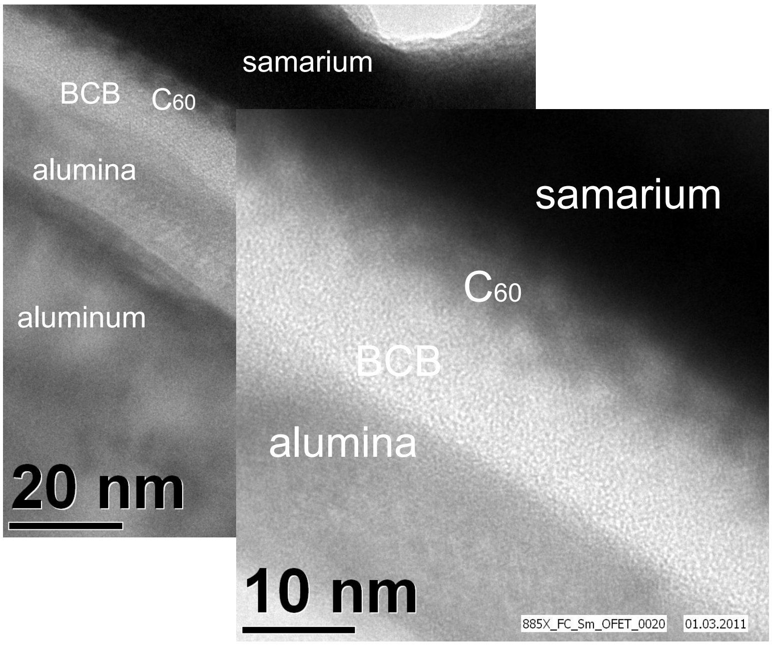

Figure 2.3: TEM pictures of thin C_{60} layer sandwiched between samarium and BCB. The zoom picture resolves the interfaces of fullerene-BCB and fullerene-samarium and the thickness respectively. The diameter is 3-4 nm within the discussed range of the promised PES experiment.

gated. Values recorded are compared to the literature. In a second step the changes of the electronic structure of C_{60} from influences of the organic interlayer are analyzed. The third step represents in-situ photoemission on heterojunctions during interfacial doping and photo-doping. All sample structures are depicted in figure 2.4.

Metal-insulator and metal-insulator-semiconductor structures

Glass (1x1 cm^2) is used as substrate for the samples. First, surfaces of 5 nm of anodized aluminum with/without BCB are investigated, after this 2-3 layers of C_{60} on alumina and on BCB are measured in XPS and UPS. All layers mentioned are prepared as described in sections 2.1 and 2.2.1. The aluminum electrode serve as reference for the Fermi level. A sketch of all investigated samples can be seen in figure 2.4. They are mounted onto the substrate holder with tape and electrically connected to the aluminum using silver paste and carbon tape. The samples are kept in ultra high vacuum (UHV, 10^{-9}mbar) overnight before characterization.

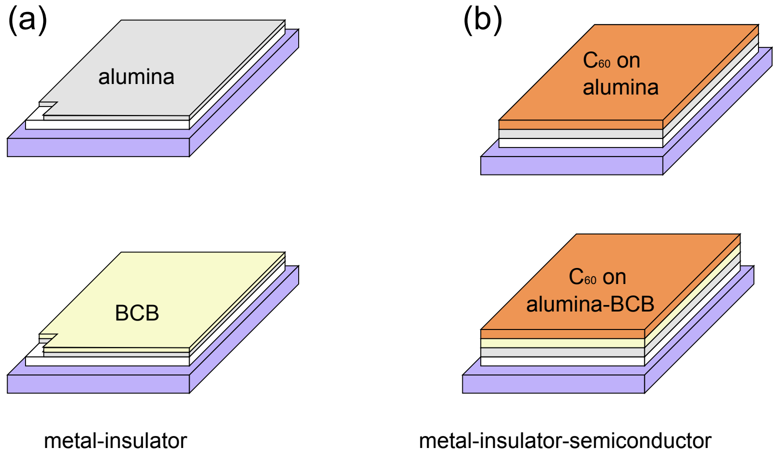

Figure 2.4: Sample structures of (a) metal-insulator (MI) and (b) metal-insulator-semiconductor (MIS) both with and without BCB interlayer.

XPS: electron spectroscopy for chemical analysis

XPS is a sensitive technique to investigate surfaces. Core electrons are excited and emitted with an element specific kinetic energy. Elements on the surface and influences from chemical environment are detected. The penetration depth of XPS is limited by the mean free path of electrons in the solid [34]. From the plot in graph 2.2 an estimation of the depth profile is possible. Together with this the chemical shift induced by different interfaces as well as an element analysis give a clear picture of the organic heterojunction. Before analyzing relative shifts of electron core levels a simple survey scan is performed, where all elements on the surface are identified. The MI samples with and without BCB are probed. Starting with alumina on aluminum, XPS spectra are recorded from 45° off normal emission angle to increase surface sensitivity (figure 2.5).

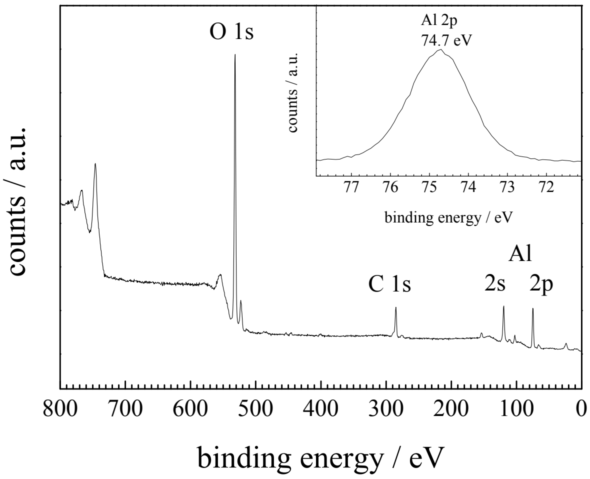

Figure 2.5: XPS survey of anodized alumina exhibiting carbon, aluminum and oxygen. Note the inset showing the Al 2p peak, which is referenced to the literature value of alumina at 74.7 eV.

The spectra are referenced to Al 2p at 74.4 eV. In the inset the Al 2p peak has been scanned with higher resolution. Apart from oxygen and aluminum carbon is observed (C 1s peak), which is attributed to contamination either from adsorbed carbon dioxide (contamination of ambient air) and residual traces of citric acid (from anodization). No further elements are identified on the surface. The survey of BCB is shown in figure 2.6. Here the underlying alumina (Al 2p) is not contributing anymore. The thickness of the polymer obviously exceeds the penetration depth of the incident beam. The molecular structure of BCB is depicted in figure 2.20, the XPS spectrum correlates to the polymer. The surface shows contributions from carbon, oxygen and silicon.

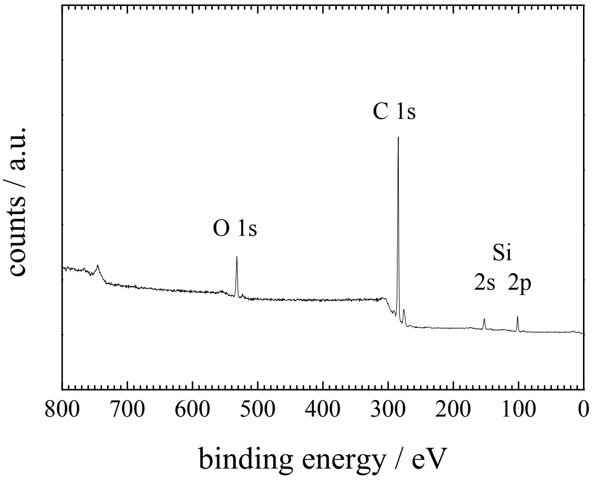

Figure 2.6: XPS survey of BCB surface. As indicated the polymeric interlayer consists of carbon, silicon and oxygen.

The chemical analysis is extended for the semiconductor. A thin C_{60} layer on top of the yet presented layers, in figure 2.7 a thin film is grown on alumina. The presence of the Al 2p feature at 45° off normal emission implies a thickness of fullerene less than the mean free path for electrons at the Mg-K_α energy less than 3-4 monolayers. The spectra presented here meet the expectation in terms of sample quality. The contamination effects found are minor. According to the spectral survey presented in figure 2.7 the results from the TEM (figure 2.3) are reflected: In the comparative plot the element features of alumina (Al 2p and Al 2s) almost disappear after deposition of C_{60}. In a second step after assuring the quality benchmarks discussed above, relative changes in core electron levels can be recorded in more detailed scans. In case of C_{60} the C 1s peak is indeed representative. These results will be presented in the next chapter 3.2.4

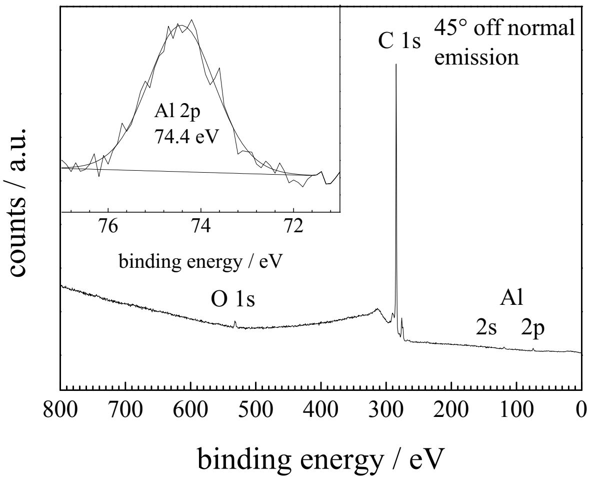

Figure 2.7: XPS survey of C_{60} on alumina. The Al 2p peak is recognized, which indicates that the penetration profile of the technique hardly exceeds the C_{60} layer thickness. The spectra were recorded 45° off normal emission to increase surface sensitivity.

UPS: characterization of DOS and work functions

In contrast to XPS core levels the valence band spectra plus low kinetic energy secondary electrons are recorded in normal emission angles. In a first quality check a reference spectrum of ex-situ UHV prepared C_{60} on a p-Si waver is measured. Both the valence features and the secondary electron cutoff are presented in figure 2.8.

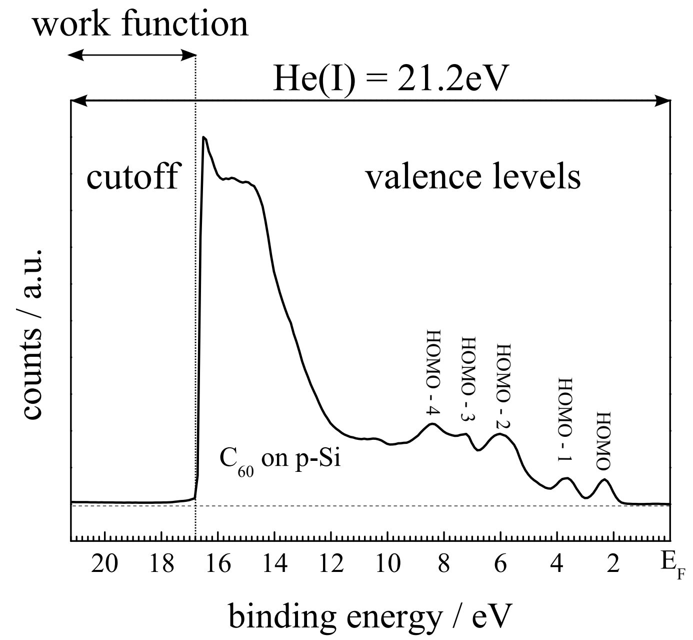

Figure 2.8: UPS spectra of ex-situ UHV prepared C_{60} on p-Si. The DOS features are identified and marked in the graph. Their quality are to in-situ UHV prepared samples from e.g. Sakamoto et al. [35], Cepek et al. [36]. Valence levels and work function obtained by a metal substrate as well as the excitation energy are indicated. All UPS spectra were recorded at the same parameters: normal emission angle, 3-4 nm of C_{60} prepared in the same way.

The valence levels recorded on the p-silicon substrate are significant and informative to check the quality of ex-situ prepared films of the semiconductor. The feature fingerprint of the uppermost C_{60} layer is identified. The quality approaches that of in-situ prepared films Sakamoto et al. [35], Cepek et al. [36].

Another quality check is by the ionization potential (*IP*), which is determined by adding the work function ϕ (cut-off) obtained by a metallic substrate and distance from the Fermi-edge to the peak maximum of the HOMO (marked in the graph 2.8 and illustrated in the sketch 2.9). The value found for C_{60} at 6.5 eV is in agreement with literature values for C_{60}-solid films [6]. The results suggest that the organic layer has sufficient quality for performing further studies on the electronic levels.

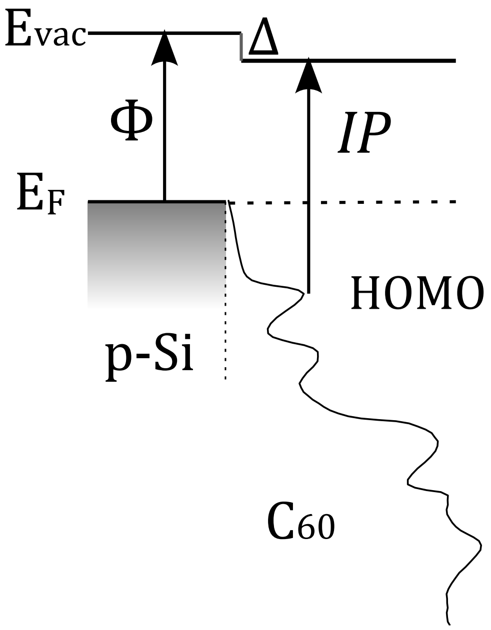

Figure 2.9: Density of states of C_{60} measured on p-Si. The DOS features can be clearly identified. The energy from the HOMO peak to the Fermi energy plus the work function the ionization potential (*IP*) is estimated. In case of C_{60} the *IP* is 6.5 eV. This value is found in the literature too by Ruckman et al. [6].

Quality of metal-insulator-semiconductor structures

A side note here are considerations about quality of the spectra when UPS is performed on a MIS, which is a crucial pre-condition to investigate an organic heterojunction. The question arises, if energy level probing on a thin insulating film e.g. alumina and/or BCB is possible at thermodynamic equilibrium. Sample charging etc. would lead to probing beyond equilibrium condition. In figure 2.10 valence levels and secondary electron cutoff on an MIS and on a reference sample (p-Si) are compared. The direct comparison shows that sensitivity is lost on the MIS substrate. Nevertheless spectra on alumina still exhibit defined fingerprint features of C_{60}. For a crosscheck the ionization potential is measured at 6.5 eV, which suggests that effects from charging are negligible.

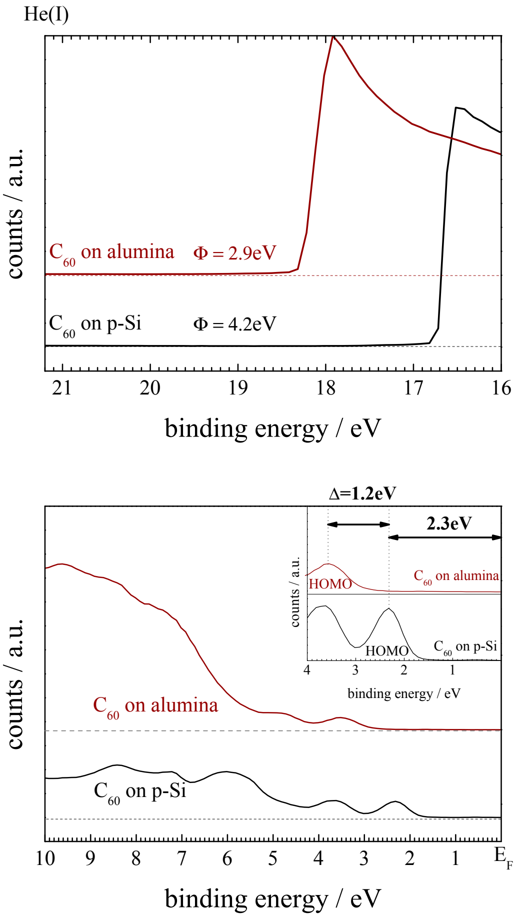

Figure 2.10: Direct relation of C_{60} features probed on p-Si (reference quality) and on an insulator (MIS structure, aluminum-alumina). Though sensitivity is reduced, fingerprint features are identified. In addition the ionization potential is in both cases 6.5 eV (e.g. 4.2 eV+2.3 eV=6.5 eV). Possible charging effects are minor. The shift of 1.2 eV is assigned to dipoles build at interfaces.

In-situ photoemission on a donor-acceptor heterojunction

For in-situ probing of C_{60} at the heterojunction with ZnPc, glass-ITO (1x1 cm^2) is used as substrate, ZnPc (25 nm) and C_{60} (3 nm) are evaporated on top, see figure 2.11. Here ITO serves as internal reference for the sample . A laser diode (Roithner, 150 mW) is mounted on the backside of the holder. During the photo-emission experiment the heterojunction is cw-pumped with the laser at 635 nm from the glass-ITO side.

The active sample area is at least 5 x 5 mm^2, which corresponds to the spatial resolution of the system. Its accuracy allows a precise positioning on the active illuminated area.

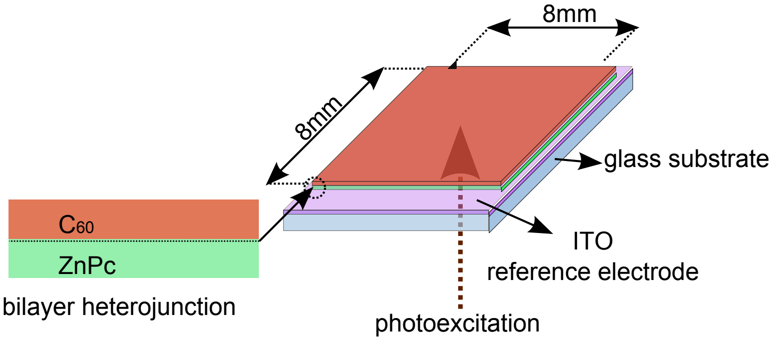

Figure 2.11: Schematic of a bilayer for in-situ probing of photoemission spectra. From the bilayer A-B heterostructure the uppermost C_{60} layer is probed . The heterostructure is photo-excited in-situ from the glass/ITO side.

2.1.2 Photoinduced absorption spectroscopy

The heterojunction ZnPc - C_{60} is investigated during photo-excitation in the mid-infrared. For probing the changes at the interfaces difference spectra are recorded in the dark and during excitation. Alternating layers of C_{60} and ZnPc are grown on top of the rhombohedral ZnSe crystal resulting in a stacked configuration: For each ZnPc layer 5 nm, for each C_{60} 3 nm are deposited, the procedure is repeated seven times. The evaporation parameters are set as described in chapter 2.1. The attenuated total reflection (ATR) element is transparent from the visible region (2.5 eV) to the mid-IR region (50 meV). By applying ATR, the sensitivity is increased: In the graph 2.13 the IR-light is indicated by the red guideline. In total reflection the evanescent wave retrains five times information about the heterojunction. The stacked layer provides multiple interfaces for improved sensitivity.

FTIR-ATR photo-induced absorption (FTIR-PIA) measurements of C_{60} and ZnPc and bilayer blend is performed in a Bruker IFS 66/S FTIR setup. The spectral region in the mid infrared (MIR at 100 meV - 700 meV) are recorded, where changes in the spectral features during photo-doping of a heterojunction are expected. The significance is increased by probing multiple interfaces in the stacked structure. In this case 14 alternating stacked layers are deposited onto the ZnSe crystal.

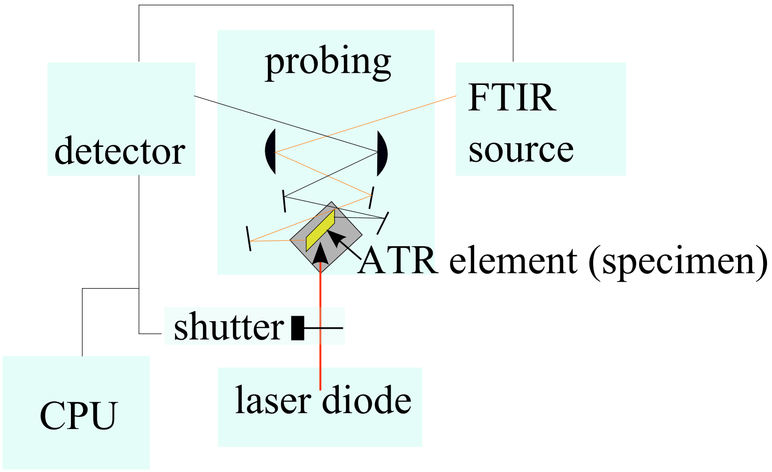

Figure 2.12: PIA setup in ATR-FTIR mode.

The experimental PIA setup and the detailed structure of the ATR reflection element is illustrated in figure 2.12. For scanning the MIR a globar source and a liquid nitrogen cooled MCT detector are used. The spectral limitations of the setup are given by the detector (until 800 meV to minimum 100 meV). The photo-excitation is performed with a laser diode pumping at 1.87 eV and 45 mW. A mechanical shutter (10 s pulse length) chops the laser beam and complementary scans in the dark and under illumination are recorded. The pulse length exactly corresponds to a full

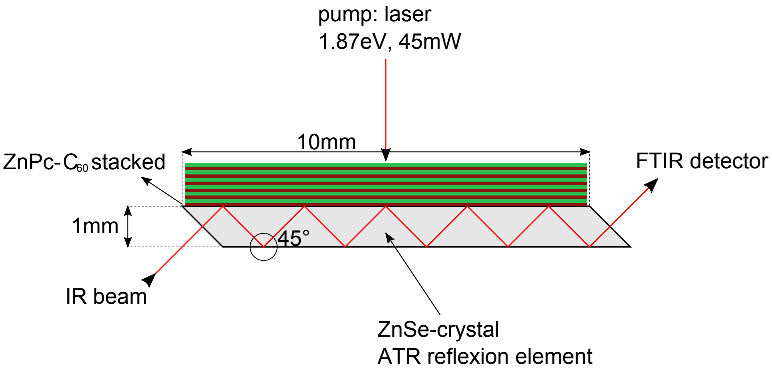

Figure 2.13: Detailed schematic of ZnSe ATR element with heterojunction applied on top.

FTIR-scan, the shutter is locked-in to the TTL signal from the FTIR-spectrometer. 1200 scans ATR-FTIR-scans in the dark ($T_{dark}(\omega)$) and under light ($T_{light}(\omega)$) are recorded and accumulated in order to reduce the noise level (around 35 times). The resulting transmission $T(\omega)$ is plotted as normalized difference spectra following equation 2.1.

$$-\frac{\Delta T(\omega)}{T(\omega)} = \frac{T_{dark}(\omega) - T_{light}(\omega)}{T_{dark}(\omega)} \tag{2.1}$$

Spectra are normalized with the dark scan $T(\omega)$. $\Delta T(\omega)$ corresponds to the photo-induced changes in the heterostructure. For a study on chosen heterojunctions first reference spectra are recorded. Here C_{60} and ZnPc alone are measured. At the very beginning a blank experiment with just the ZnSe-ATR crystal is performed. ZnSe does not contribute to photo-induced changes at the set pump energy (not shown). Afterwards the single material PIA spectra in the MIR are scanned as a reference (figure 2.14). For C_{60} alone no big changes are found, at 700 meV a slight increase is seen. Anyhow, the absorption coefficient (see 1.7) at pump energy around 1.87 eV is already low. A different behavior is observed for ZnPc, where indeed changes are observed. They are important as a preparation step before going to the heterostructure. This work does not focus on single-material spectra, therefore the discussion on the changes in single ZnPc is left to other scientific contributions [37, 38]. Both single material spectra define the energy range, at which probing of interfacial effects in a heterojunction is meaningful between 100-700 meV.

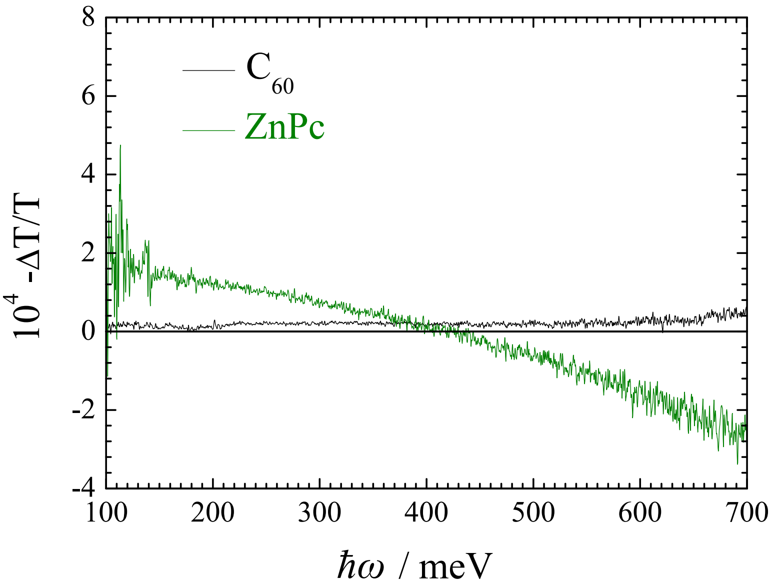

Figure 2.14: PIA spectra of single materials in the mid-infrared. Changes are observed in the ZnPc, with is directly excited at 1.87 eV.

2.1.3 Light-induced electron spin resonance

Similar to the PIA samples, a stacked alternating ZnPc - C_{60} structure is deposited on a quartz substrate. The substrate is mounted onto a glass-rod. The sample is then positioned into the microwave-cavity in a He-cryostat for the ESR-measurement. The successive excitation of the dye is performed through a slit with a He-Ne laser (250 mW, 1.96 eV), which is mounted outside the ESR setup.

Light-induced ESR samples are loaded into the microwave cavity and cooled at 4.5 K. A brief description of the setup is illustrated in the schematic in described in the literature by Scharber [39]. The sample characterized in the dark and during illumination with a continuous wave He-Ne laser (150 mW, 1.96 eV). Similar to the PIA and in-situ photoemission the heterojunction is excited targeting at the electron-transfer from the absorbing dye to the fullerene. Photo-doped molecules are then detected in the ESR.

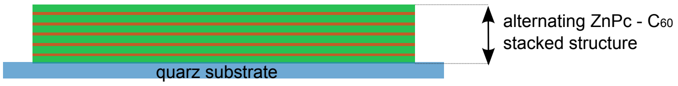

Figure 2.15: Heterojunctions applied to the photoinduced absorption setup in the mid-infrared region. For the reflexion element in ATR mode a germanium crystal is used. ZnPc is photoexcited from the top side.

2.2 Device fabrication

2.2.1 Hybrid dielectrics for field-effect transistors

As introduced in 1.4 a hybrid- or double layer-dielectric consists of a high-ε oxide thin film plus an organic layer applied on top. For the inorganic part obviously valve metal oxides serve as a suitable material for high-ε dielectrics [40, 41]. Generally such oxides can be grown on tantalum, titanium, hafnium or aluminum by various techniques. In this work the oxidation is performed by electrochemical anodization (anodic oxide films). The most abundant element - aluminum - is used. The dielectric constant of the corresponding oxide (alumina) ranges within 7.5-15, it varies with the fabrication method [42]. When electrochemically grown the aluminum-alumina structure apparently results right in the desired gate-dielectric structure for a bottom-gate FET [43–45]. A schematic of bottom-contact FET-structures are shown in figure 2.16. Alumina from anodization is particularly performing well in terms of dielectric strength, the breakdown fields are in the desired performance range between 300-400 V μm^{-1} [46]. A detailed view on film quality shows that the performance is dependent on the growth parameters and treatment afterwards. All steps in fabrication will be discussed in detail underneath. A profound study on anodic aluminum oxidation is the work of Diggle et al. [47]. Several parameters were incorporated from this literature source.

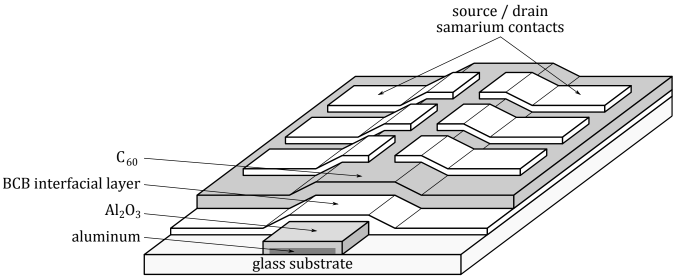

Figure 2.16: Schematic of OFET applying hybrid dielectric. Aluminum-alumina serve as gate and gate oxide respectively.

Anodic aluminum oxide films

100 nm aluminum films are deposited onto glass by thermal evaporation at a rate of 10 Å s^{-1}. A steel shadow mask is used to pattern the aluminum electrode for the resulting OFET.

The electrode is implemented as anode in an electrochemical cell for a galvanostatic oxidation, as depicted in figure 2.17.

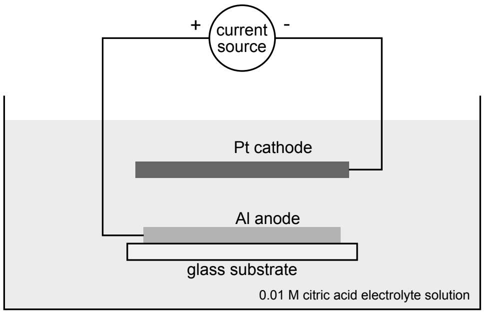

Figure 2.17: Sketch of the electrochemical cell for galvanostatic aluminum anodization.

The cell consists of a platinum counter electrode (CE), as electrolyte serves a 0.01 M citric acid solution, the aluminum - the working electrode (WE) - is facing the platinum cathode and connected to the current source via a coated copper wire. The end is bonded using little amount of indium on the aluminum contact pad, details are illustrated in figure 2.18.

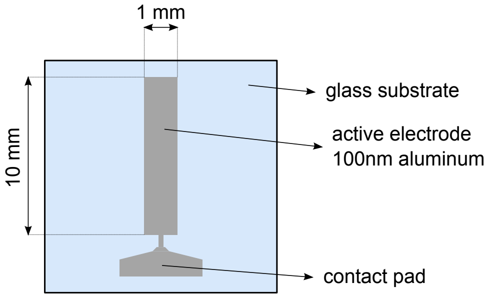

Figure 2.18: Sketch of the electrochemical cell for galvanostatic aluminum anodization.

The contact area is insulated with nail-polish. This configuration guarantees Faraday-currents from the aluminum-oxidation process only, side reactions on the copper or indium are suppressed. Using a defined area and preset current (constant current density j) the thickness is proportional to the anodization time. Voltage drops during anodization are monitored. The chemical reactions on anode and cathode are described as follows:

$$\text{Anode} \qquad 2\text{Al} + 3\text{H}_2\text{O} \rightarrow \text{Al}_2\text{O}_3 + 6\text{e}^- + 6\text{H}^+$$

$$\text{Cathode} \qquad 6\text{H}^+ + 6\text{e}^- \rightarrow 3\text{H}_2$$

The galvanostatic anodization is performed at current densities around $j = 0.6\,\text{mA}\,\text{cm}^{-2}$ leading to a constant growth rate of the oxide. The factor 6 corresponds to the stoechiometric factor from the anode reaction, N_{e^-} is the number of electrons transferred, F is the Faraday constant and A the area.

$$N_{\text{Al}_2\text{O}_3} = \frac{N_{e^-}}{6} = \frac{j \cdot \text{A} \cdot t}{6 \cdot \text{F}} \tag{2.2}$$

The density and the molar mass of alumina are used in the next step to derive the number of aluminum atoms transferred to alumina. By controlling the time the thickness of the oxide can be determined as followed by the equation.

$$\text{d}_{\text{Al}_2\text{O}_3} = \frac{j \cdot M_{\text{Al}_2\text{O}_3}}{6 \cdot F \cdot \rho_{\text{Al}_2\text{O}_3}} \cdot t \tag{2.3}$$

The operation suggested by Majewski [43] applies current densities in the range of $j = 0.6\,\text{mA}\,\text{cm}^{-2}$, all parameters left needed for calculation are found in the "Handbook of Chemistry and Physics" [48], see table underneath (2.2.1). A growth rate as great as 16 nm per minute anodization time is finally derived (equation 2.4).

constant	value	unit
F	96 485	$\text{C}\,\text{mol}^{-1}$
$\rho_{\text{Al}_2\text{O}_3}$	3.97	$\text{g}\,\text{cm}^{-3}$
$M_{\text{Al}_2\text{O}_3}$	101.96	$\text{g}\,\text{mol}^{-1}$

$$\text{d}_{\text{Al}_2\text{O}_3}[\text{nm}] = 16 \cdot t[\text{min}] \tag{2.4}$$

The calculated thickness is crosschecked using cross-section scanning electron microscopy, see figure 2.22. The interface aluminum-alumina can be clearly identified and the alumina thickness is measured. Throughout all anodizations performed the calculated values correspond within a 5 % error to the measurement.

Alumina treatment

After the anodization the oxide is treated for 15 minutes at 80 °C in 18 MΩ-water in an ultrasonic bath and rinsed thoroughly. For drying the substrates are kept in vacuum at 150 °C overnight.

The morphological changes on the surface during the oxide formation and the water treatment afterwards are monitored ex-situ with AFM. Tapping mode topographies were recorded before and after the anodization and water treatment. Figure 2.19 educes changes during the preparation of an 80 nm alumina film on aluminum. The roughness of aluminum is essentially not changed, when 80 nm of oxide is generated when comparing figure 2.19 before and after anodization. On the contrary as prepared alumina before drying exhibits a different morphology. The changes are interpreted as water take-up and formation of voluminous aluminum-hydroxides after treatment with water. After annealing overnight at 150 °C in vacuum the surface roughness decreases again.

The AFM topographies underline the important role of the water treatment after anodization.

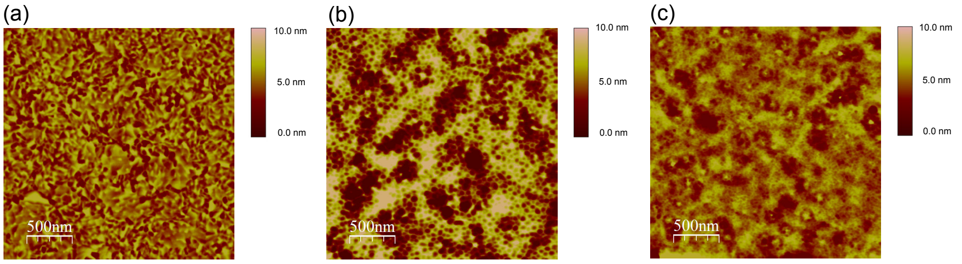

Figure 2.19: AFM topographies (2.5 x 2.5 μm^2) taken of a 150 nm deposited aluminum film on glass (a). (b) After forming an 80 nm film of alumina on top by galvanostatic anodization and water treatment for 15 min at 80 °C the morphology changes. (c) The surface roughness is decreased and pinholes are closed again after drying in vacuum at 150°C overnight for operation as high-ε dielectric in OFETs.

Surface modification with BCB

The alumina surface is modified after drying. As discussed in section 2.2.1 an organic thin-film layer is applied on top of the oxide (organic interlayer or passivation layer). In combination with divinylsiloxane bisbenzocyclobutene (BCB crosslinkible resin, Dow Chemicals, brand name ”Cyclotene”) fullerene transistors with high performance have been demonstrated [24, 49, 50]. The chemical structure is depicted in figure 2.20.

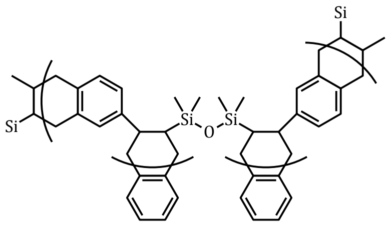

BCB

Figure 2.20: Molecular structure of crosslinked divinylsiloxane benzocyclobutene (BCB).

For its excellent dielectric properties and thermal stability BCB is considered as substitute for silicon dioxide in microelectronic engineering forums [51, 52]. Once cross-linked, $\varepsilon = 2.6$ is constant within a frequency range of $10^1 - 10^5\,Hz$, see figure 2.21.

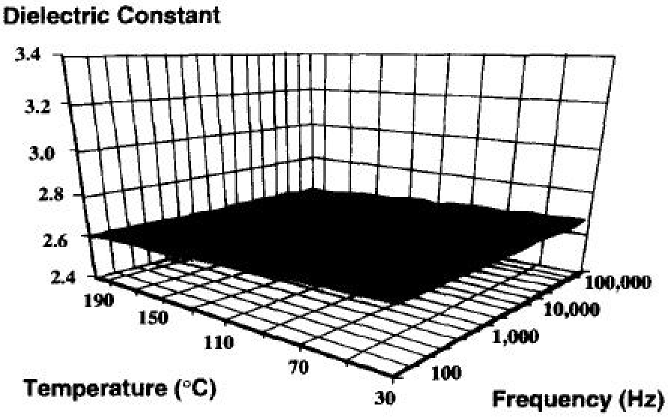

Figure 2.21: Dielectric constant ε as a function of frequency and temperature for BCB. Figure courtesy of Mills et al. [51].

Detailed electronic and interface properties in combination with organic semiconductors are discussed later in section 3.2.1. Apart from electronic and dielectric considerations BCB acts as a surface smoothening layer. By spin-coating the monomer solution on the substrate, thin, homogeneous layers can be achieved. A diluted 0.1 w %BCB-solution in mesitylene is spin-coated on top at a rate of 1 500 rpm and annealed in vacuum at 180 °C overnight. Using this parameters, 6-10 nm layers are obtained.

The final hybrid dielectric insulator is visible in a cross-section TEM picture. In figure 2.22 the aluminum-alumina-BCB structure is recorded on a nanoscale-slice cut from a representative sample. The interfaces between aluminum and alumina as well as alumina and BCB become visible. The alumina thickness measured from the picture are in good agreement with the calculated values from equation 2.4. In this case, the aluminum was anodized exactly 1 minute á 16 nm.

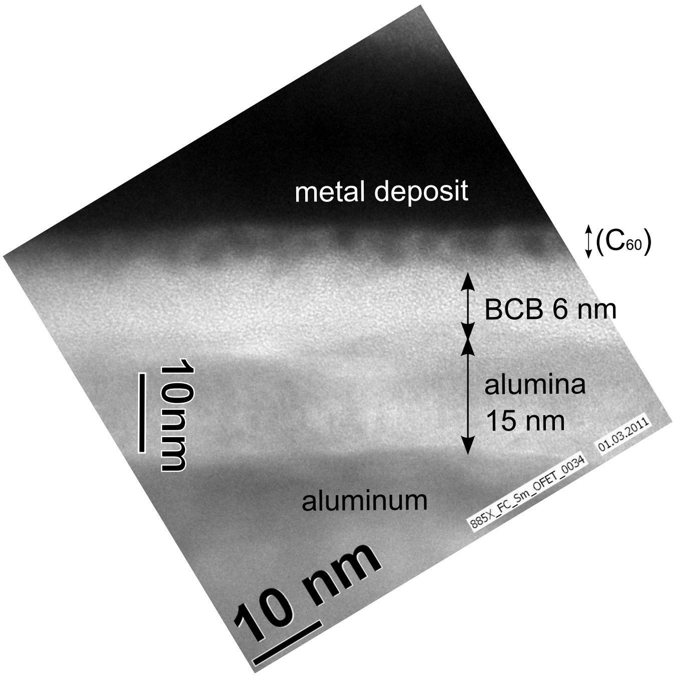

Figure 2.22: Cross section TEM picture of hybrid dielectric. Bottom to top: Aluminum, alumina and BCB have different electron densities, lighter elements appear brighter. The sample is capped with a metal deposit. The molecular thin C_{60} layer will be discussed later in section 3.2.1.

2.2.2 Hybrid dielectric characterization

The dielectric for the organic field effect transistor is crucial for the device performance. As profoundly described in section 2.2.1 alumina and BCB serve as hybrid dielectric insulator to form a A-B type heterojunction 1.1. Before fabricating field effect transistors the dielectric properties of this thin films are ananlyzed using capacitance- and leakage-current measurements. The target is to get information about the breakdown voltage and the leakage currents as well as the displacement currents in the interval of 1Hz - 0.1MHz in the hybrid insulator system.

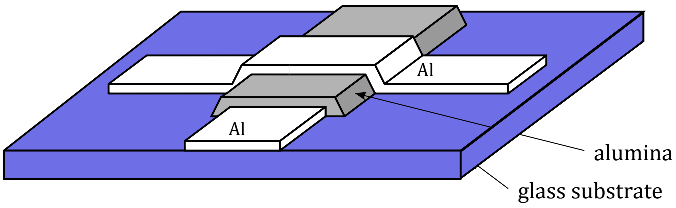

Figure 2.23: Metal-insulator-metal (MIM) device constisting of aluminum and anodized alumina (10 nm) covered with an aluminum top electrode.

Alumina can be grown in different ways, therefore the dielectric properties vary with the fabrication method. It is crucial to analyze leakage currents in the electrical field of anodized alumina alone. Metal-insulator metal (MIM) or here aluminum-alumina-aluminum devices are fabricated as depicted in figure 2.23. The leakage currents are measured in a quasi-static scan (steps of $1\,\mathrm{V}\,\mu\mathrm{m}^{-1}$ per 100 seconds). The thickness of the alumina is 10 nm.

In figure 2.24 the current density as a function of the field is plotted. Up to $350\,\mathrm{V}\,\mu\mathrm{m}^{-1}$ the current density j is close to the detection limit of the source meter. Above $350\,\mathrm{V}\,\mu\mathrm{m}^{-1}$ the current density increases exponentially, at $500\,\mathrm{V}\,\mu\mathrm{m}^{-1}$ there is a change in the slope (seen in a little kink in the graph). The exact analysis of the anodized alumina system is discussed in Kaltenbrunner et al. [53].

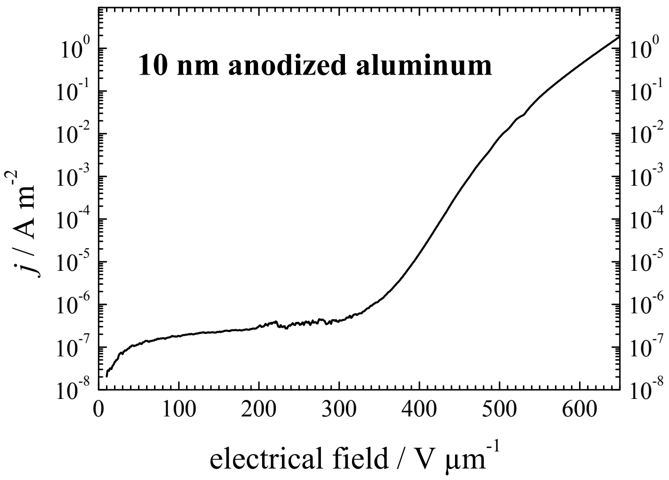

Figure 2.24: Current density as a function of the electrical field applied in a quasi-static measurements at 1 mV per 100 s. Above 350 V μm^{-1} tunneling currents occur. A kink in the exponential region is further seen at 500 V μm^{-1}.

In combination with BCB the bilayer is analyzed by dielectric spectroscopy. The capacitance is measured within a frequency range between 10 Hz to 0.1 MHz. Again a MIM device is used to analyze the structure, which is depicted in figure 2.25.

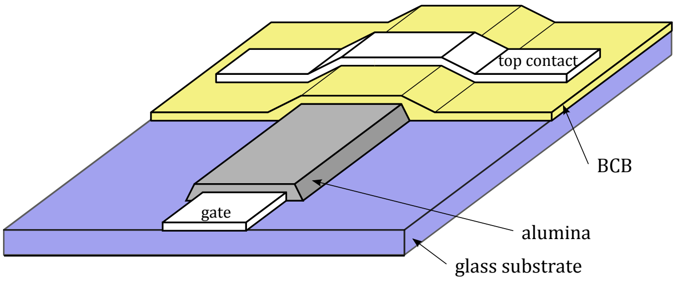

Figure 2.25: Thin layer of BCB (approx. 15 nm) covers alumina (80 nm) on aluminum and is covered with aluminum top electrode for dielectric spectroscopy.

In the graph in figure 2.26 the capacitance C_i of the hybrid dielectric (80 nm alumina and 16 nm BCB) is plotted as a function of frequency. The inset shows the dielectric loss $tan(\delta)$. The dielectric function is approximately a constant. Ionic impurities and pinholes are not present in the hybrid dielectric.

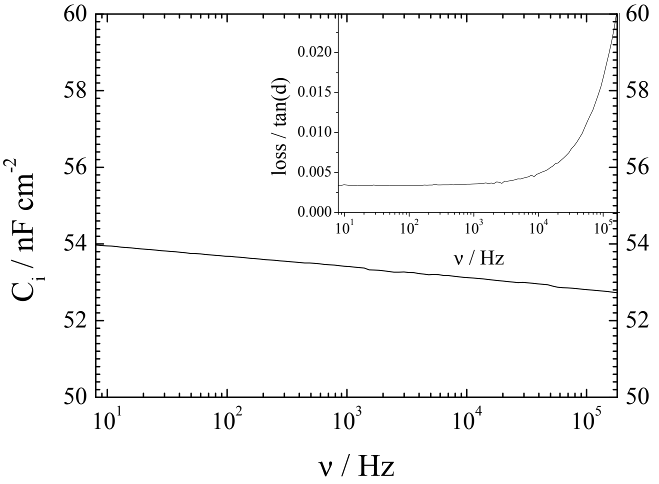

Figure 2.26: Dielectric spectroscopy applied to the hybrid aluminua-BCB structure. The capacitance as well as the loss angle are constant up to the 100 kHz regime.

2.2.3 Contact metals

OFETs need source-drain metal electrodes, which allow efficient electron injection to the organic semiconductor. Usually metals with low electron affinity (*EA*) such as calcium are used. In case of aluminum e.g LiF enhances electron injection to organic semiconductors [54]. For an ohmic contact to C_{60} LiF-aluminum has been shown to be efficient [13, 55, 56]. These contact electrodes exhibit a great sensitivity towards exposure to moisture and oxygen. Even little amounts in the ppm-range have a distinctive influence on the electron injection. Less sensitive is samarium ($\Phi = 2.7$-2.8 eV). The lanthanide has been applied to OPVs and OLED structures and serves as efficient electron injection and extraction electrode [57]. Similar to LiF-aluminum a thin doped layer at the contact interface can be formed [58]. The main difference to calcium, magnesium and LiF-aluminum is the fact that the corresponding samarium-oxide formed on the surface after oxygen and moisture exposure is semiconducting [59].

A thin native oxide layer between metal and semiconductor obviously does not completely inhibit injection to the organic semiconductor. In figure 2.27 complementary OFET characteristics using samarium as source-drain contacts before and after exposure to ambient atmosphere are shown. This device has been characterized in nitrogen atmosphere and exposed to ambient conditions for 60 min. After transferring back to the inert gas system, a moderate decrease in performance is observed. Influences from oxygen and moisture are observed: The threshold voltage is shifted to positve values and the I_{drain} current is decreased. Both effects back the assumption, that an oxide contact-barrier is formed between the metal surface and the semiconductor.

The stability facilitates the practical handling. Practically the lanthanide is thermally evaporated in high vacuum at a rate of $1\,\text{Å}\,\text{s}^{-1}$. In controlled moisture- and oxygen reduced atmosphere, samarium contacts are stable for months.

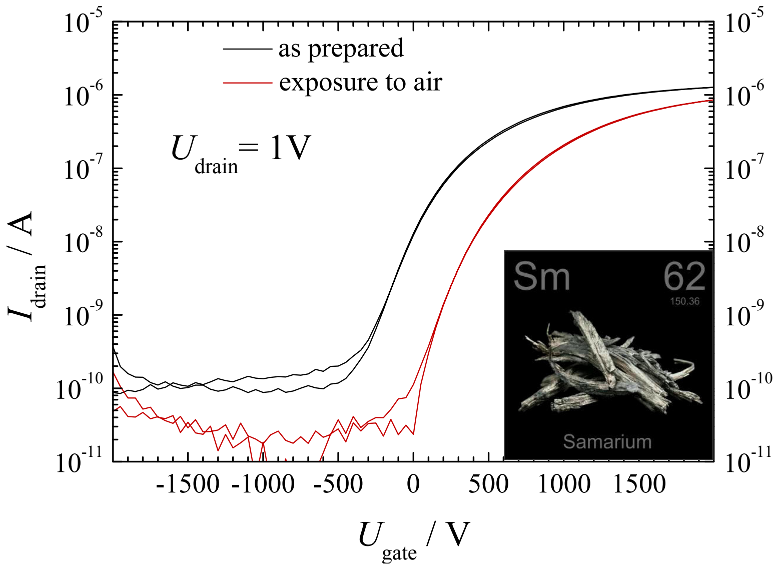

Figure 2.27: C_{60}-based OFET using samarium source-drain contacts. After exposure to air the threshold voltage shift to the positive and currents decrease.

2.2.4 Organic field effect transistors (OFETs)

Field effect transistors are fabricated as follows: 1.5x1.5 cm^2 Glass is used as a substrate, the surface is treated with with 2 % solution of 3:1 mixture NH$_4$OH:H$_2$O$_2$ at 80 °C (base piranha) in the ultrasonic bath. 200 nm of aluminum is evaporated in high vaccuum at a rate of 10Ås^{-1} for the gate. The electrode is placed in the center of the substrate. The aluminum electrode is electrochemically oxidized and modified as described in section 2.2.1. For the organic semiconductor, C$_{60}$ is evaporated on top by thermal evaporation, see section 2.1. Problems from edge effects are avoided by pattering the semiconductor see figure 2.28. The transistor is completed by deposition of samarium source-drain contacts on top.

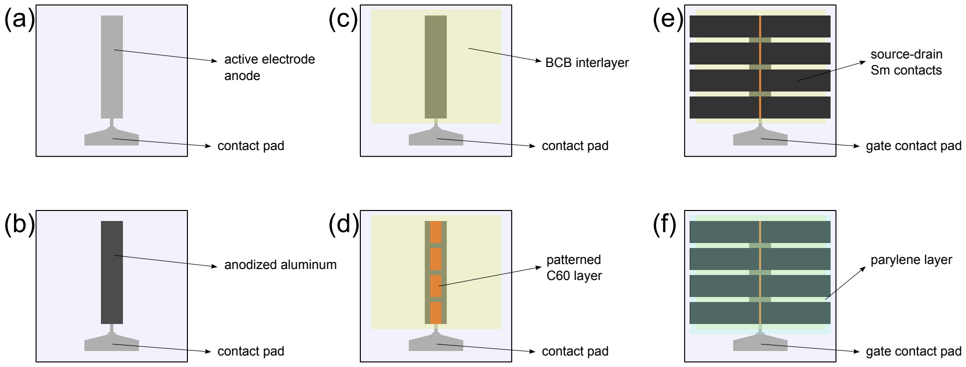

Figure 2.28: OFET fabrication: Evaporation of (a) patterned alumnium and (b) anodization of active area, (c) BCB surface modification and (d) C$_{60}$ deposition of 4 layers through a shadow mask. (e) The deposited source-drain contacts are shown and (f) depicts the finished device with a parylene encapsulation-layer.

For the device patterning generally different steel shadow masks are used. For the transistor, a channel length L equal to 100 μm is used, the channel width W is 2 mm. For spectroscopic investigations and conductivity measurements different dimensions and mask systems are used. Usually the devices are encapsulated with a 5 μm layer of parylene, which is evaporated on top. Before characterization, the electrodes are contacted using silver paste and spring contacts, gold wires or by soldering copper-wires with indium.

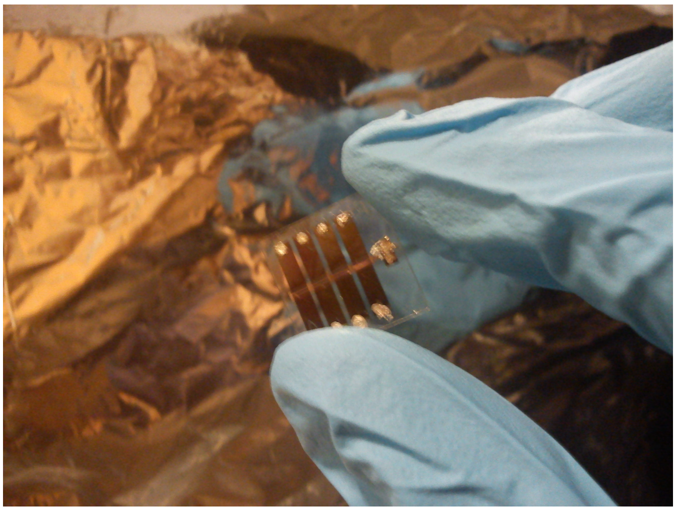

Figure 2.29: Picture of as-prepared OFET. Four source-drain contact share one gate contact.

2.2.5 In-situ photoemission in an OFET channel

A bottom-gate top contact OFETs was fabricated, applying the methods described in section 2.2.4. Instead of using a channel lengths of 100 μm and a width of 2 mm the geometry is expanded to $L = 5mm$ and $W = 5mm$, in order to avoid contributions from the source-drain electrodes. The incident He (I) beam irradiates an circular surface with the diameter d=2 mm within the channel. The photoemission spectra are probed in the center of the broad channel, an illustration is given in figure 2.30.

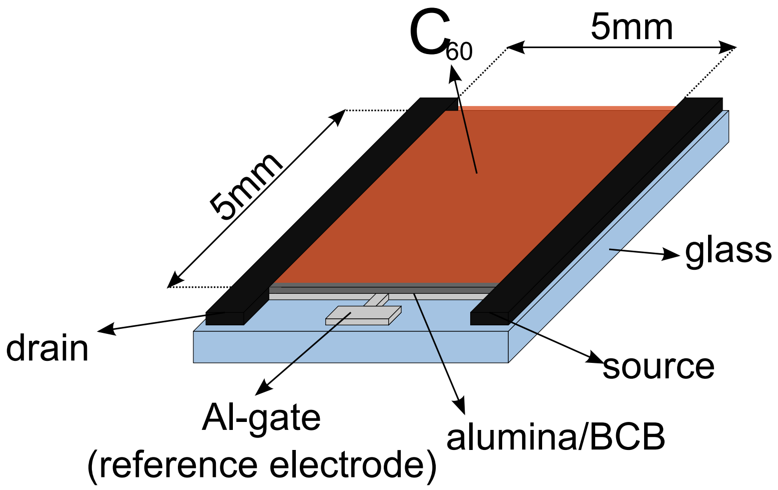

Figure 2.30: Schematic of an OFET with expanded channel geometries. The channel area is adjusted to the spacial resolution (diameter = 2 mm) of the incident UV-beam from the He (I) lamp. Note the gate electrode serves as the reference electrode to the analyzer, source and drain are connected separately for a in-situ OFET operation.

2.2.6 Resistivity measurements

The conductivity of thin C_{60} is probed in an OFET. Instead of just two contacts 6-probe geometry is applied. The gate electrode is adjusted to the 6-probe top electrode. The sample geometry including patterning-steps is depicted in in figure 2.31.

Apart from the different geometry the sample preparation is identical to the fabrication of OFETs as described in chapter 2.2.4. The exact dimensions of the electrodes and layers underneath are depicted in figure 2.32. In addition to source and drain two contacts on each sides (F1-4) are implemented in between. Potential drops perpendicular (xy) and parallel (xx) to the current flow direction can be probed.

The magnetic field is applied perpendicular to the sample plane. The advantage of the 6-probe setup are that contact resistances at the metal-semiconductor junction can be ruled out, as barriers get dominant at lower temperatures. The monitoring of U_{xx} and U_{xy} as a function of magnetic field and temperature can be used for a Hall measurement. With a classic Hall measurement the carrier concentration N_e and the mobility μ can be determined.

$$N = \frac{1}{eU_{xy}} \cdot \frac{IB_z}{d} \tag{2.5}$$

$$\mu = \frac{\sigma}{eN_\mathrm{e}} \tag{2.6}$$

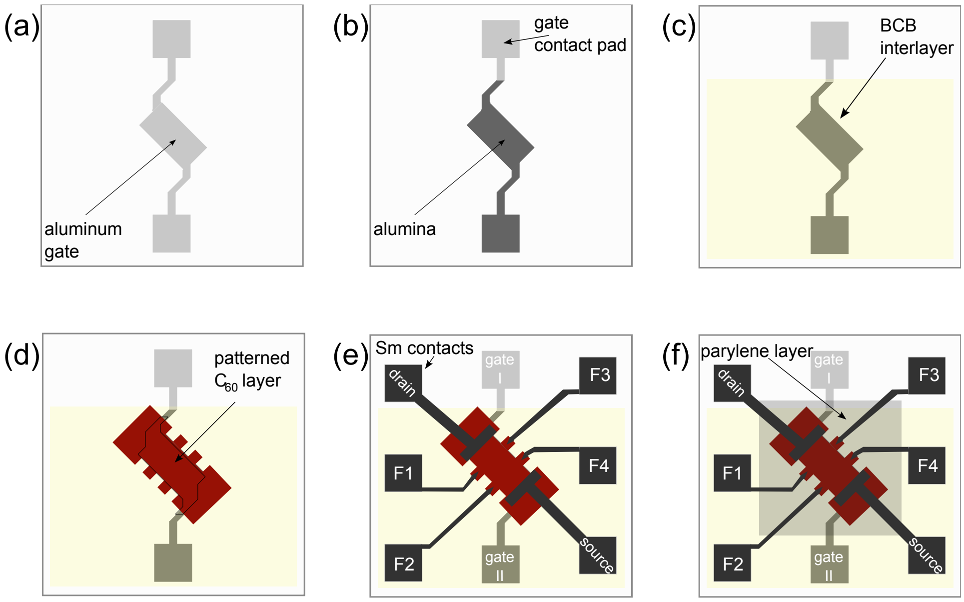

Figure 2.31: Fabrication steps of OFET for 6-probe geometry: (a) Aluminum gate deposition followed by (b) galvanostatic anodization to alumina of indicated areas and (c) spin-coating of BCB-interlayer. (d) The C_{60} layer is covering the gate/gate-dielectric and adjusted to the (e) samarium contacts. Six electrodes are applied as showed in the figure. For encapsulation a 5 μm protection-film of parylene is evaporated onto the channel region (f).

B_z is the magnetic field perpendicular to the surface plane. The sheet conductivity σ is determined from the U_{xx}, e is the electrical charge, d the thickness of the semiconductor and I_x represents the current applied.

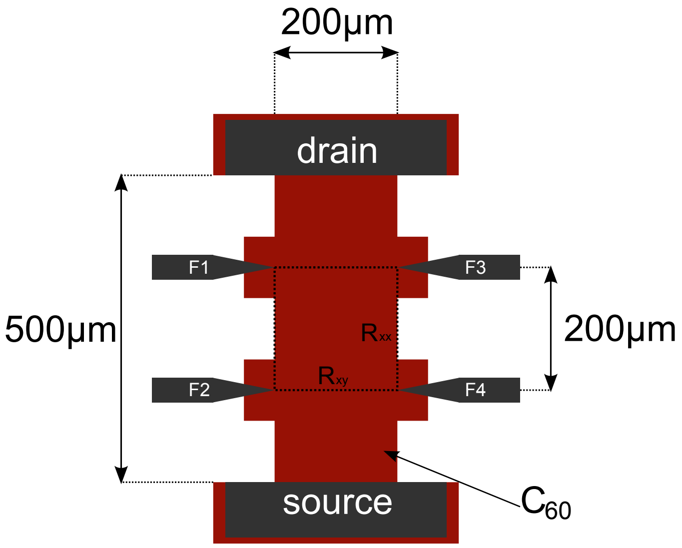

Figure 2.32: 6-probe sample including dimensions (idealized schematic) are shown in the schematic. Note the square in the centre from the potential probes F1 to F4.

Resistivity measurements and magneto-resistance

The conductivity of C_{60} is dependent on the charge carrier concentration as well as on the temperature and the morphology. Since C_{60} films are intrinsic semiconductors, a doping method has to be applied. Here field-effect interfacial doping is applied, which offers advantages as followed:

- The doping is concentrated on the interface between the organic semiconductor and the dielectric (in this case C_{60} and BCB). Using ultra thin films in nm - range and fabrication techniques as described in section 2.2.6, carrier densities in the range of $10^{13}\,\mathrm{cm}^{-2}$ are obtained.
- The doping concentration can be tuned by changing the gate voltage applied.
- Morphological issues play an important role in the characterization of a van-der-Waals type solid state system. Phase transitions occur at lower temperature and grain boundaries in polycrystalline samples limit the significance of the results. Therefore ultra-thin homogeneous amorphous films of C_{60} are applied.

The carrier density N_e is in the ideal case directly proportional to the gate voltage U_{gate}. One restriction in the correlation from equation 2.7 are presence of electron traps in the organic semiconductor (grain boundaries, impurities) and at the heterojunction (impurities, shallow traps in the dielectric materials). Only free charge carriers contribute to the electron transport. Both trap origins are minimized

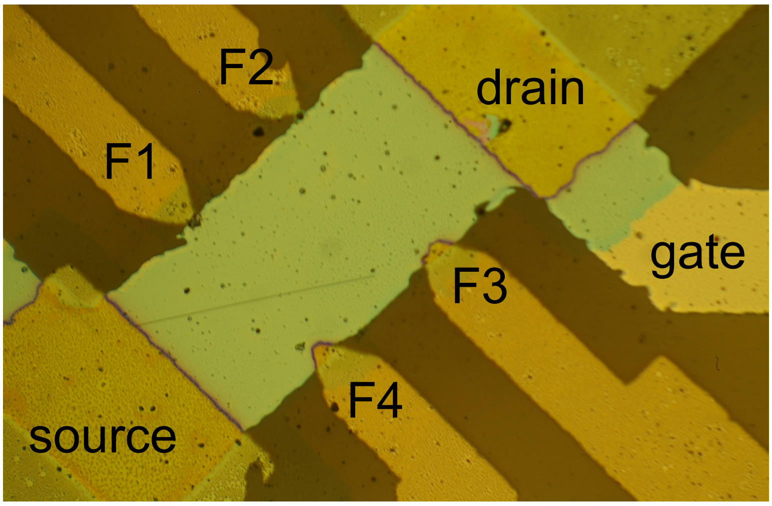

Figure 2.33: 6-probe taken from optical microscope of complete sample. The shape of active layer (20 nm C_{60}) can be recognized. The sample is completely covered with parylene.

by using BCB as trap-free dielectric and thin, homogeneous C_{60} films. The carrier density is calculated from the geometric capacitance of the dielectric:

$$N_e^- = \mathrm{e} \cdot \mathrm{C_i} \cdot (U_{\text{gate}} - U_{\text{th}}) \tag{2.7}$$

Using a dielectric such as presented in figure 2.26 (80 nm alumina, 16 nm BCB) the geometric capacitance is measured at 55 nF cm^{-2}. The theoretical maximum accessible carrier density per unit area $N_{\mathrm{e^-,max}}$ for the alumina-dielectric can then be calculated from the breakdown-field $U_{\text{breakdown}}$.

$$U_{\text{breakdown}} = E_{\text{breakdown}} \cdot d_{\text{alumina}} \tag{2.8}$$

$$N_{\mathrm{e}} = C_i \cdot (U_{\text{breakdown}} - U_{\text{th}}) \tag{2.9}$$

The value for alumina ($E_{\text{breakdown}}$=300 V μ m^{-1}) can be readout from figure 2.24. The resulting theoretical maximal charge density per unit area is around $8{\cdot}10^{12}$ cm^{-2}.

The fabrication of a field-effect device is described in section 2.2.4. The channel resistance is then measured as a function of the gate voltage U_{gate}, the temperature T and the magnetic field B. The measurements are performed as followed:

- The sample is mounted in the cryostat. For contacting 10 μm gold wires are bonded to the contact areas with silver paste. The sample is covered with a copper-cleading and exposed to high vacuum at $1{\cdot}10^{-4}$ mbar. Source and drain are connected to the current source.

The gate contact is plugged to the voltage source. The source serves as ground for the gate. Two electrometers (input resistance 1 GΩ) are connected to the the potential probe contacts F1-4. The geometry of the sample has been depicted in detail in figure 2.32.

- A constant gate voltage is applied to the sample at a constant gate voltage. The interval of gate voltages is limited by the threshold voltage U_{th} (minimum) and by the breakdown voltage $U_{\mathrm{breakdown}}$ (maximum). Both values can be extracted from the OFETs 3.24 and from the dielectric characterization 2.24.
- A constant current $\vec{I}_{\mathrm{x}}$ is applied from source to drain. In order to get reliable results, the current is set at a range of at least 100 nA up to 10 μA. Note the OFET always operates in the linear regime.
- The four-probe system is used to measure the potential drops perpendicular U_{xx} to the current flow. The potentials are monitored at room temperature (300K) for several minutes until the values stabilize. Then the temperature is decreased (and increased) by a defined scan time.
- The magnetic field is applied perpendicular to the surface plain. For the magneto-resistance, the magnetic field is kept constant over a full temperature scan. The setup-limitation is given with a magnetic flux of B=1 T.

2.2.7 Encapsulation techniques

Samples sometimes have to be exposed to ambient atmosphere before mounting in measurement setups. Especially in OFETs for conductivity measurements it is crucial to apply a protection layer. Parylene (thickness in the range of 1-5 μm) serves as an encapsulation layer. Dichloro-di-para-xylylene (parylene) is deposited onto e.g. the OFET. The exact procedure for the chemical vapor deposition technique is described in detail by Sharma et al. [60]. Parylene offers two key advantages: First of all, the layer does not destroy or influence the device performance and the film can be locally removed easily just by rubbing for e.g. contacting. The lifetime in ambient atmosphere for sensitive devices can be extended to several days during transport.

Chapter 3

Results on heterojunctions

3.1 Donor-acceptor heterojunctions

The photo-doping of the heterostructure and the observation of the energy levels in the fullerene is rendered possible by selectively exciting ZnPc. The absorption spectra of the photo-doping process are depicted in figure 1.11. The organic layers deposited in an alternating stacked layer-by-layer structure have different electron affinities (LUMO*), the figure depicts a quantum mechanical description along the z-axis perpendicular to the layer-by-layer structure plane, see figure 3.1. There is evidence, that the alignment at the interfaces enables photo-induced charge transfer [16, 61–64]. Although theoretically comparable some crucial differences to inorganic quantum wells have to be taken into consideration: The question is, if bands are formed within several molecules of fullerenes. In organic molecules no sharp transitions and defined borders as depicted in figure 4.2 are expected. The interfacial properties reveal a gradual transitions. The aim of this work targets on the characterization of the interface during photo-excitation. The final question will be, if evidence of a quantum well of an bi-dimensional system of *organic* molecules can be found.

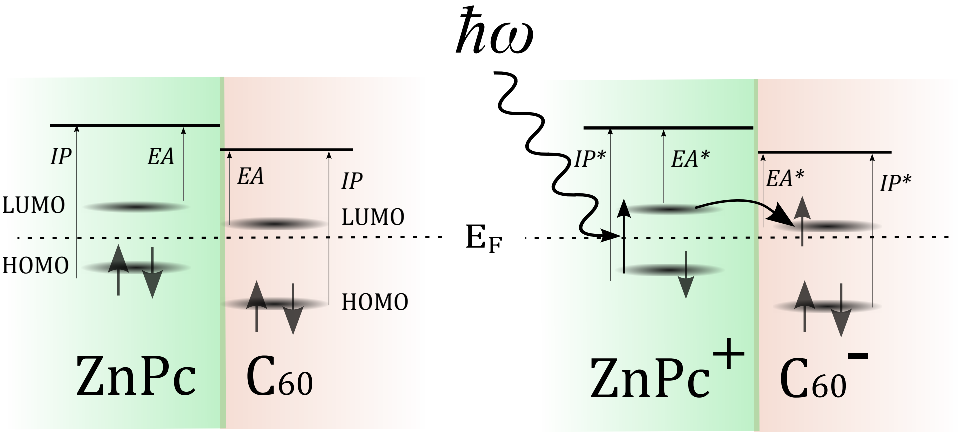

Figure 3.1: Schematic of the photodoping at the ZnPc-fullerene heterojunction. The ZnPc is excited and an electron-hole pair is formed.

3.1.1 Photoinduced photoemission spectroscopy

These experiments apply PES in-situ studies on the photo-doping process. The experiment targets on the appearance of the LUMO in photo-doped C_{60}. Similar to the in-situ study on the OFET, closed 3-4 molecular layers of C_{60} are investigated during doping, this time the layers are grown on top of ZnPc/ITO. Again, a donor-acceptor structure is revealed, the uppermost layer is probed for changes. In a first experiment the energy level alignment of C_{60} on the ZnPc at the donor-acceptor interface is investigated in the dark with features situation (a) in figure 3.1. In figure 3.2 the valence bands and the secondary electron cutoffs for C_{60} on BCB and alumina are related to them on ZnPc. The work function and the position of the HOMO leads to the conclusion, that molecules align similar as observed for BCB or p-Si.

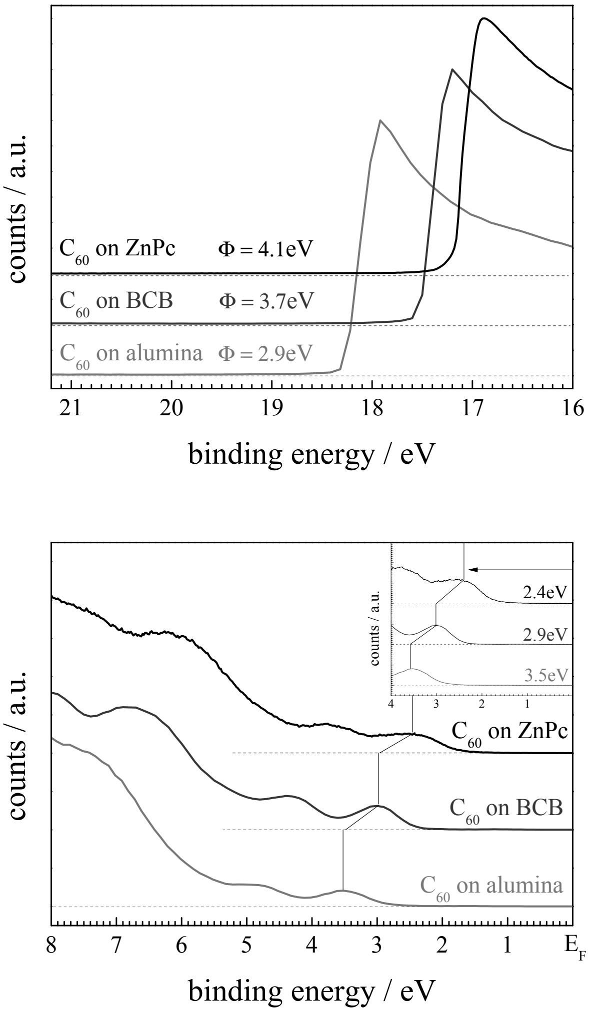

Figure 3.2: Top: Cut-off and work functions indicated for C_{60} at different interfaces. Bottom: Valence levels of C_{60} at different interfaces exhibiting dipole controlled alignment for BCB and even more for ZnPc-interface.

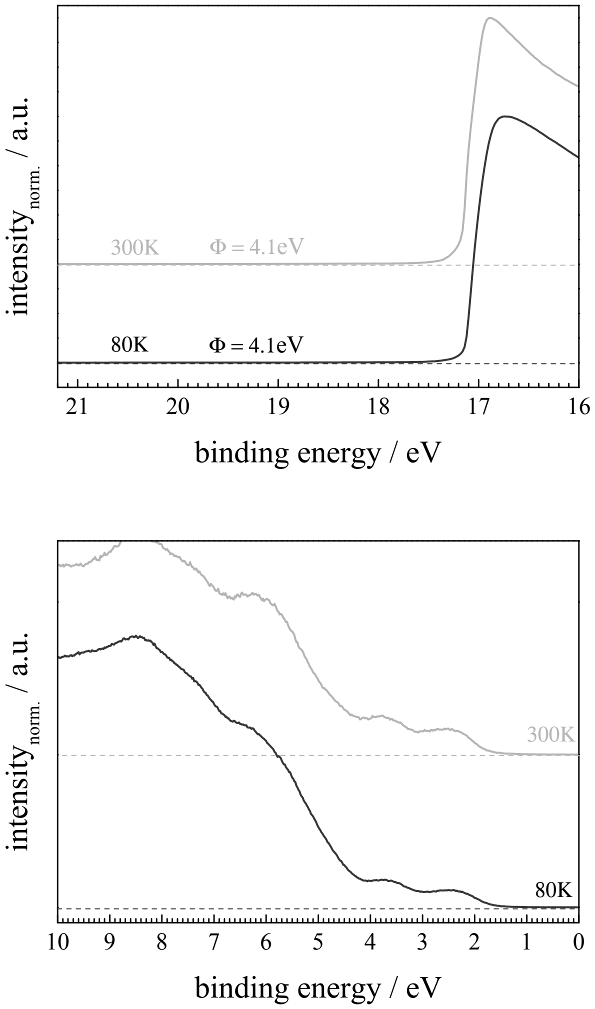

Figure 3.3: Right: Cut-off and work functions indicated at 300 K and 80 K of C_{60} on ZnPc. Left: Valence bands exhibit lower noise for spectrum recorded at 80 K

The next step is the pump-probe experiment by photo-exciting selectively the donor (ZnPc) and measure the changes in the electron acceptor energy levels adjacent to the interface. The valence bands at different pump intensities at 50, 100 and 150 mW are recorded and compared to the dark experiment. The temperature during measuring is set to T=80 K. By lowering the temperature (at T=80 K kT=7 meV) noise is decreased and the lifetime of carriers extended. The changes by temperature in the dark reference spectra are shown in a separate figure (figure 3.3). Minor contributions from the temperature are observed in terms of better defined peaks in the valence levels. Figure 3.4 shows the comparison between dark and photo-excited heterostructures. At the bottom the valence bands in the dark experiment are shown, the pump intensity is then stepwise increased and valence levels are listed upwards in ascending steps of 50 mW.

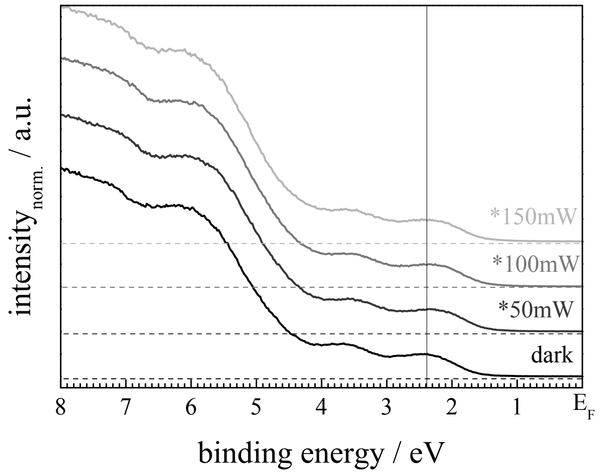

Figure 3.4: Valence levels for C_{60} at different pump intensities. The black line at the HOMO of the dark spectrum indicates the photo-inducted changes in the valence spectra.

The vertical line at the C_{60}-HOMO is a guideline for following up changes induced by pumping. A slight shift of the valence levels to the Fermi-edge is observed. A detailed complementary spectrum is depicted in figure 3.5, where a photo-induced shift in the range of 0.2 eV at the peak maximum and the onset of the HOMO is observed. Additionally the baseline from the HOMO to the Fermi energy is increased, corresponding to the results achieved by in-situ UPS on the transistor (see section 3.2.7). In figure 3.33 the HOMO shifts towards the Fermi energy upon electrical field doping at higher gate voltages. At the same time the baseline between HOMO and Fermi edge increases, anyhow photo-induced features cannot be identified. The LUMO is expected to arise at the same time close to the Fermi edge [35].

The shift of the HOMO towards the Fermi energy indicates a weak effect generated by photo-doping. The result is interpreted as follows: The L-ESR spectra in section 3.1.2 give evidence of a charge separation and the formation of electron hole pairs. In the experiment presented in figure 3.6 as well for the photo-induced absorption (figure 3.9) multiple interface structures (layer-by-layer stacked) are applied. Differently in UPS one single interface can be investigated. Another issue addresses geminate charge carriers pairs, which are located at the interface. The thickness of the in-situ probed C_{60} layer may exceed the mean-free-path for electrons.

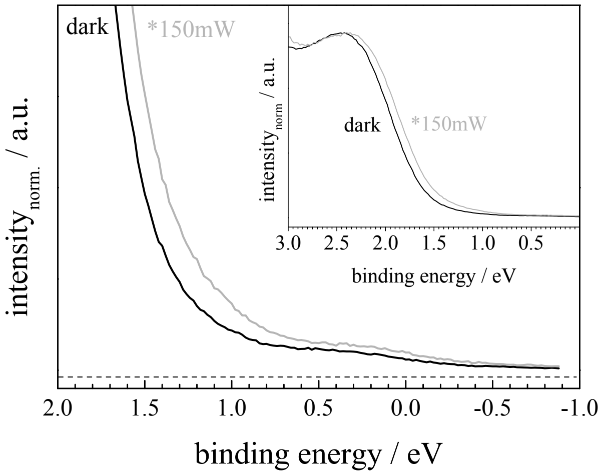

Figure 3.5: Detailed spectra between dark and photo-excited heterostructure. An increase in the baseline is observed.

3.1.2 Photo-induced electron spin resonance at multiple heterojunctions

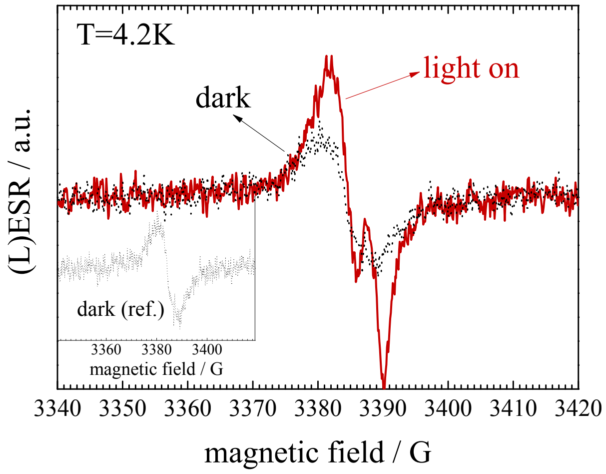

Figure 3.6: The light-induced ESR resonance signal of a ZnPc-C_{60} structure exhibiting distinct features for electron-hole pair formed. The photo-induced effect is immediately vanishes after illumination. Note the reference vigin dark signal in the inset (bottom-left), originating from oxygen induced radicals in the ZnPc dye.

The ultimate proof for the creation of an electron-hole pair at a single junction is not observed. Consequently the heterojunction is extended to a multiple donor-acceptor system. Here, light-induced ESR clearly gives evidence about formation of charge carriers, the formation of an electron-hole pair. The technique excels in terms of high sensitivity: Only radicals with an unpaired spin are detected. The sensitivity is increased by the mulitlayer A-B-A structure. In π-conjugated system radical anions and cations are formed by photo-induced charge transfer. Two signals from each molecule are detected.

The organic alternating stacked layers are measured in the dark and after cw-illumination with a red laser. At 1.96 eV pumping energy selectively the donor molecule are excited leading to charge transfer to the lower lying acceptor state and the formation of an electron hole pair. The ESR signal is recorded during and immediately after the photo-excitation. The spectrum in figure 3.6 shows two distinctive photo-induced signals between 3370-3390 G. Immediately after switching off the laser signals disappear. Actually the higher peak is reduced to the virgin reference spectrum taken before photo-excitation, see inset bottom left. The signal is assigned to doping of ZnPc with oxygen: The samples are exposed to ambient air before loading to the cryostat.

From the L-ESR result a significant photo-induced doping is observed, seen in

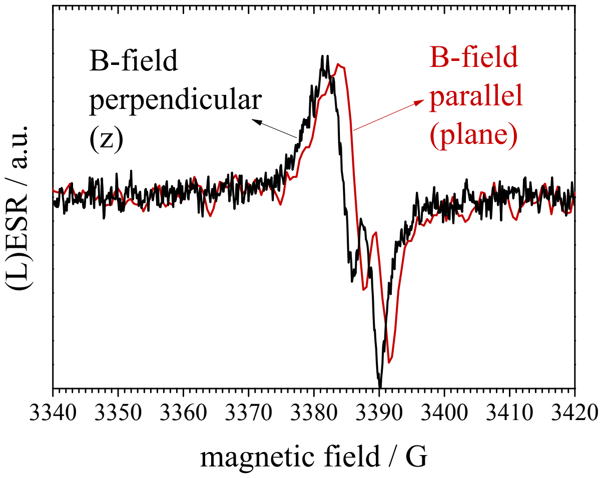

Figure 3.7: L-ESR spectra show two different signals by twisting the sample 180°: Two different magnetic field directions (B_z perpendicular and B_{plane} parallel to the surface plane) are investigated.

two resonance features. The higher peak is assigned to the ZnPc radical cation, the overlapping feature to the C_{60} anion. The photo-induced signal disappears immediately after switching off the laser. The fast recombination differs from results obtained from conjugated polymer-C_{60} heterojunctions, where part of the photo-induced resonance signal remains constant at comparable conditions (T=4.2 K) [10, 65, 66]. The results suggest geminate type of charge carriers close at the interface.

The second information from the L-ESR experiment is the change in the angle of the magnetic field by twisting the sample 180°. In figure 3.7 the B_z resonance perpendicular to the structure plane is found at lower magnetic fields compared to the in-plane resonance signal. The shift is indicated in the detailed figure 3.8 from peak-to-peak, the magnitude is distinctive at ΔB=1.5 G for all features. The difference is attributed to an anisotropy in the sample, which rather originates from the layer-by-layer heterostructure than from the symmetry of ZnPc. More information about the source of anisotropy is gained in the next experiment.

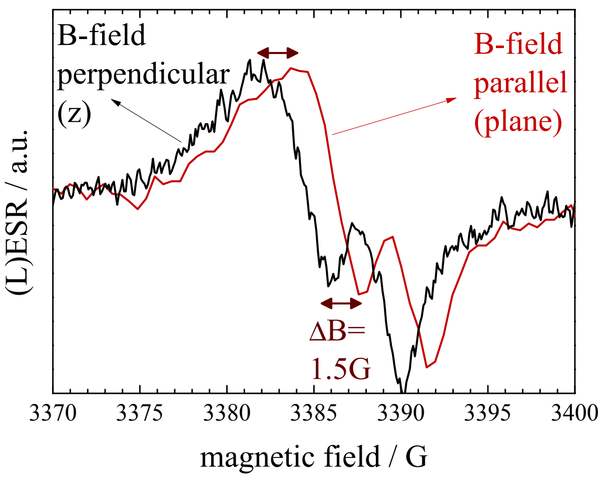

Figure 3.8: Detailed L-ESR spectra taken at two different magnetic field directions: B_z perpendicular and B_{plane} parallel to the surface plane exhibiting an anisotropy in the layer-by-layer structure of indicated 1.5 G.

3.1.3 Photo-induced absorption at an multiple heterojunctions

After evidence of the formation of an electron-hole pair seen in the L-ESR the changes in absorption are measured. The geminate appearance of the photo-induced electron-hole pair is interpreted as spin-spin coupling and consequently strong interactions. In the quantum well the energy barrier V_b is given by the difference in the electron affinities (*EA*s). Values for the LUMOs can be found in literature (most often measured by cyclic voltametry). Anyhow, the author believes that the absolute values do not represent the certainty needed for a precise calculation. Influences from interfacial dipoles at the heterojunction have to be considered, which will be discussed in the chapter on interfacial doped heterojunctions 3.2.4. The main point is in addition the changes in the energy level alignment during photo-excitation, e.g. C_{60} has different acceptor properties in excited state [67]. Similar effect are expected for ZnPc. Therefore the energy border has to be measured directly at the junction.

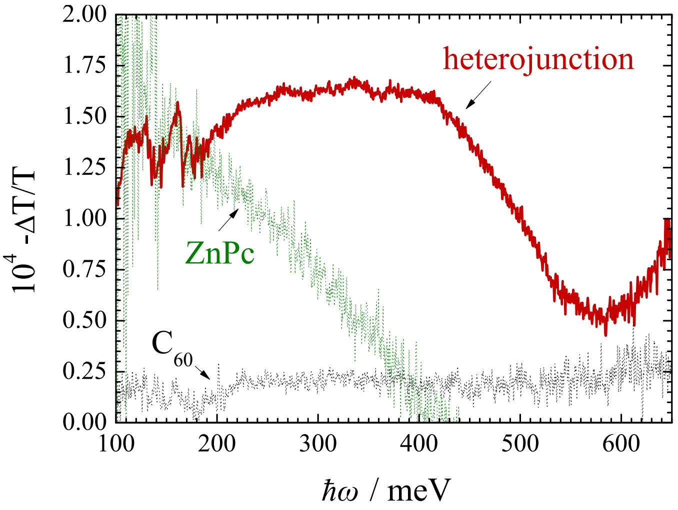

Figure 3.9: Photo-induced absorption spectra in the mid-infrared of a layer-by-layer grown heterojunction (red line). A broad absorption feature is observed in the region between 250-300 meV. Note the difference to the single material spectra for ZnPc and C_{60} (black and olive dots) shown in the background of the graph.

The concomitant shift in the spectra in the angle-resolved L-ESR in figure 3.7 gives rise to an interaction within the heterojunction. The question is now, if an intermolecular feature - a mini-band - would arise during photo-excitation. From ab-initio estimation the energy for this transition is expected in the mid-IR region between 100-700 meV. In section 2.1.2 the experimental details for the feasibility to probe specifically a ZnPc-C_{60} heterojunction are presented.

The heterojunction is photo-excited and in-situ the IR absorption is probed. In the graph 3.9 the changes $-\frac{\Delta T}{T}$ are plotted as a function of energy. In addition to the heterostructure (line), the single material spectra are probed in the same way and presented in the graph (dots). First of all the author states a distinct change between single and heterojunction spectra. Positive values in the heterojunction indicate new features arising. A broad peak in the investigated spectral range is found between 250-300 meV.

The question arise, whether the feature originates from a specific interfacial transition from the quantum well structure or rather from a fullerene anion or ZnPc cation absorption. For clarification a direct comparison with a ZnPc-C_{60} blend (2:1) is performed. In the bulk-heterojunction blend the order of the layer-by-layer heterojunction - the organic quantum well structure - is lost.

In figure 3.10 the blend is compared to the stacked layer-by-layer structure. Interestingly the feature at 300 meV has disappeared (black line). Note at the left side the almost identical increase in the signal in both structures, which is assigned to a specific C_{60} anion absorption [68].

The results look promising. A closer look at the heterojunctions indeed shows a feature arising, which is only found in the layer-by-layer structure - a structure, which reveals closest a multiple type I heterostructure (figure 4.2. The author leaves the discussion open for the scientific forum, whether a bi-dimensional property is observed or not. The energy region around 200-300 meV by all means render the expectations for a miniband transition.

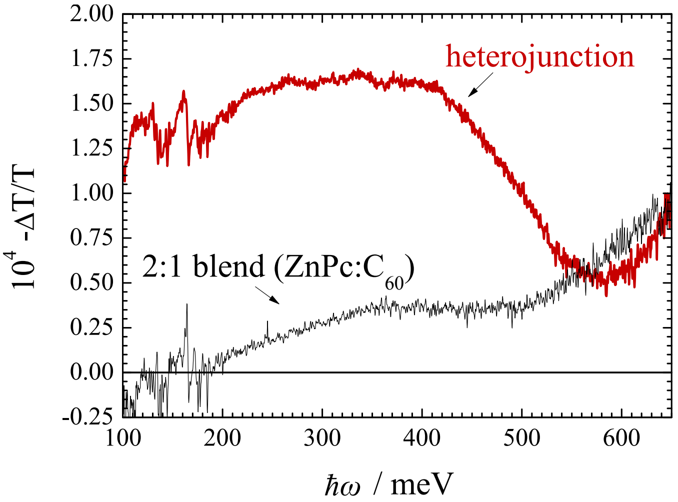

Figure 3.10: Comparison of photo-induced absorption between an ordered quantum-well like layer-by-layer heterojunction and a blend of ZnPc and C_{60}. The feature at 250-300 meV disappears. Note the similar onset in both structures at around 600 meV.

3.2 Heterojunction in an OFET structure

3.2.1 Energy level alignment at a MIS-structure

Metal-organic interfaces are matter of different investigations in organic electronics. Here the energy level alignment at an interface is carefully analyzed. In figure 3.11 a metal-organic interface is shown.

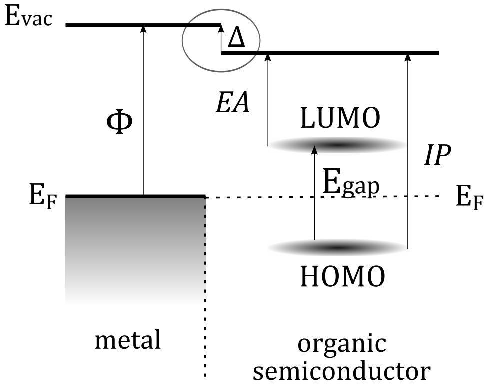

Figure 3.11: Density of states of C_{60} on p-Si. The dipole indicated at the interface is low in this case (0.2 eV).

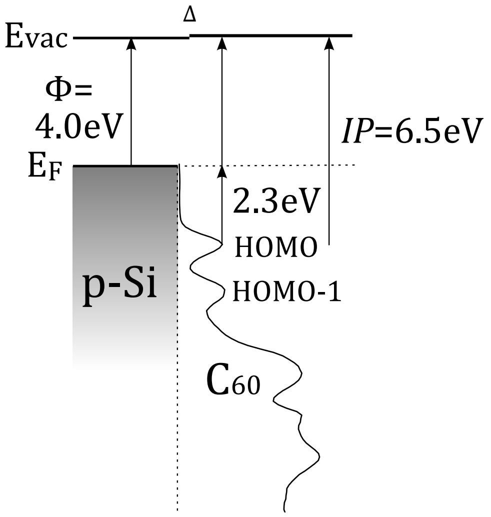

Figure 3.12: Density of states of C_{60} on p-Si. The dipole indicated at the interface is very low in this case (0.2 eV)

The ionization potential (*IP*), electron affinity (*EA*) and metal work function (ϕ) are defined material-specific parameters. The only empiric parameter are dipoles formed at the interface. In the energy diagram the dipole is indicated by a Δ from the difference in the vacuum levels at the interface. Profound surface analysis of metal-organic interfaces have demonstrated, that the energy alignment does not generally follow the Mott-Schottky limit, nor ohmic contact are observed in pristine organic semiconductors [69]. Obviously dipoles Δ control the energy level alignment at the interface [70].

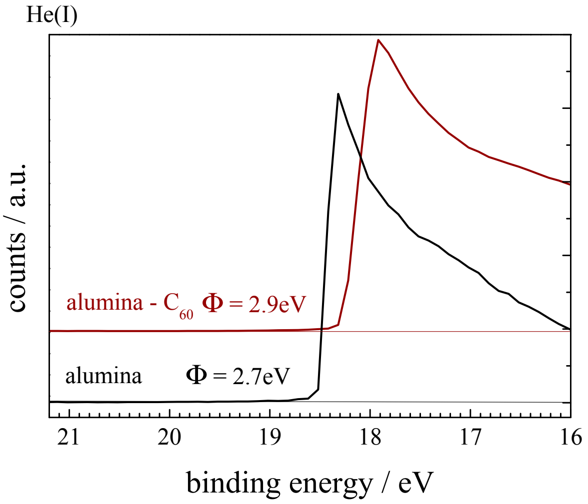

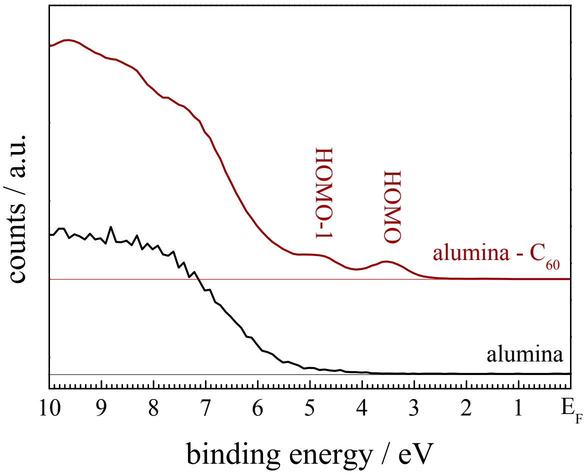

Figure 3.13: Surface scan of MI and MIS structure. The features of C_{60} arise, the changes in work-functions are indicated in the next to the cut-off.

An example for a dipole-controlled interface has already been quoted in this work in section 2.1.1: C_{60} on p-Si. The energy diagram is shown in figure 3.12. Note that the DOS and the p-Si work-function are measured values from UPS.

Here a dipole is found in the range of 0.2 eV. Probably pinning effects dominate this interface, which is a typical phenomenon for fullerenes [55]. The energy situation is completely reshuffled, when an insulating layer is sandwiched in between, for instance, if an organic semiconductor is analyzed in a metal-insulator structure. The question arises, how the insulator influences the energetic situation of the organic semiconductor. A simple MIS structure analyzed in figure 3.13 is aluminum-alumina and C_{60}. Aluminum is oxidized electrochemically and C_{60} deposited on top. The changes from deposition of 3-4 layers of C_{60} are reflected. A résumé is given for all values derived from the UPS spectra in figure 3.14.

Similar to p-Si, the dipole at the interface between the organic semiconductor and insulator is measured at 0.2 eV. However, when the vacuum level of the semiconductor is compared to the metal gate, the dipole arose is huge: It is set at 1.4 eV. The energy level alignment has changed.

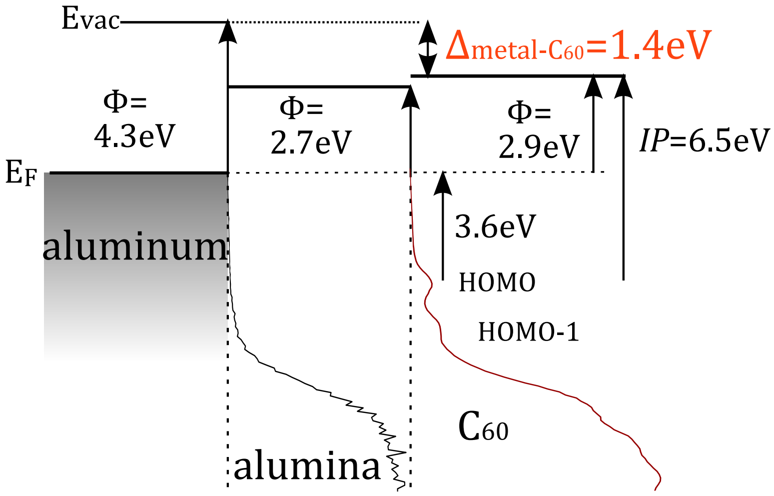

Figure 3.14: Energy diagram containing all energy levels derived from the UPS spectra in 3.13. Different to the metal-semiconductor the dipole between the metal and semiconductor is huge.

3.2.2 From MIS structures to the role of the dielectric in an OFET

The energy situation at the dielectric-semiconductor interface in OFETs is revealed in a MIS structure. There is rather common sense or empirical evidence about the role of organic interlayers in OFETs, anyhow, high-performance devices are demonstrated with interlayers applied [71]. Practically few-molecular organic interlayers are sufficient to drive transistors remarkably to higher performances [72]. The fact that organic interlayers improve the transistor characteristics is investigated and discussed intensively in literature. The interface doping process is distinctively influenced by the energy level alignment of the organic semiconductor at the interface to the dielectric surface. In a first approximation, an organic field effect transistor can be seen as a one-terminal, *interface-driven* device (figure 3.15).

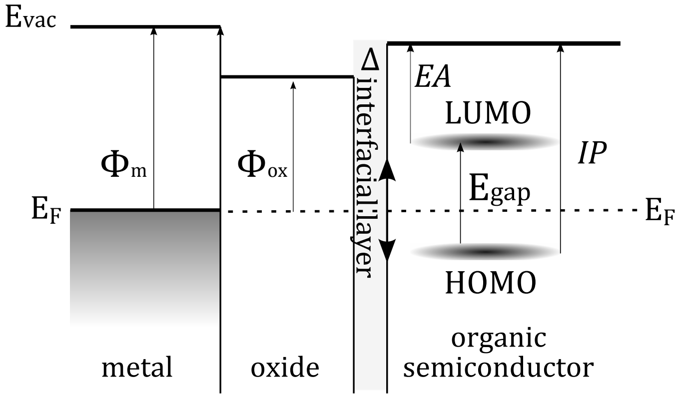

Figure 3.15: Schematic energy diagram of a MIS structure with an organic interlayer between the metal oxide and the organic semiconductors. The dipole controls the position of the HOMO and LUMO level with respect to the gate metal.

When exclusively considering the channel region, energetically remote from source-drain electrodes, the energy level alignment is determined only by the dielectric - semiconductor interface. The gate electrode underneath serves as a reference metal. Consequently if the alignment at the interface is unfavorable as reported for e.g. bare alumina as a dielectric, no matter how much gate voltage will be applied, OFET performances are lousy, even charge transport can be completely disabled [71–73].

The crucial part is now to measure the energy levels as close as possible to the interface. A MIS structure without top electrodes as fabricated in section 2.1.1 serves as a model for a channel region. In order to probe the energy levels at the interface, the semiconductor layer has to be homogeneous, closed and as thin as possible (TEM image 2.3). For a complementary study on the role of a specific organic interlayer - in this case BCB - alumina - layers with and without BCB are compared. The source-drain electrodes are substituted by the analyzer in a photoemission setup, the ”gate” electrode serves as sample reference electrode. The electronic structure of a mounted MIS sample in a photoemission probing system describes then exactly the situation in the OFET channel region.

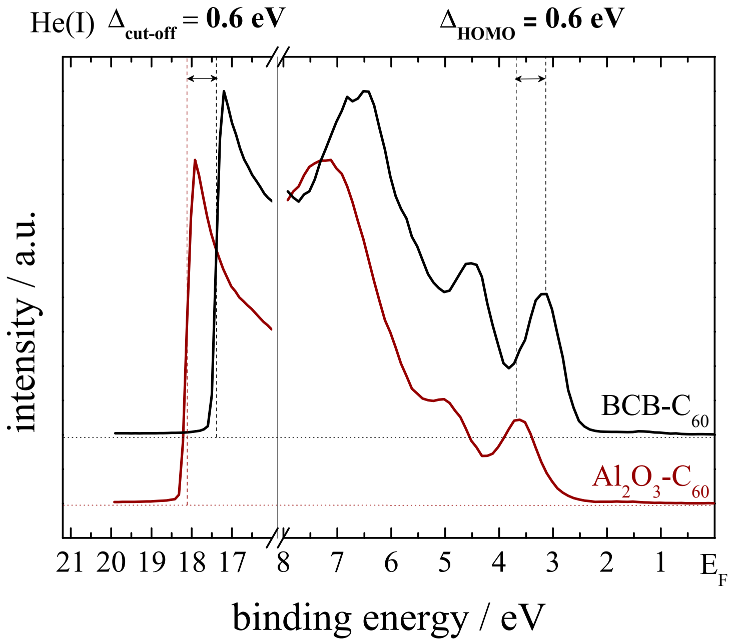

Figure 3.16: Spectra revealing the DOS of C_{60} on BCB (black line) and pristine alumina (Al_2O_3, red line). The features are well defined. A dipole by 0.6 eV controls the position of the entire spectra relative to the gate reference metal (E_F).

The energetic situation on bare alumina has already been investigated in figure 3.14. The in-built dipole Δ with respect to the metal is 1.4 eV. The structure now is compared to a MIS structure with an BCB interlayer.

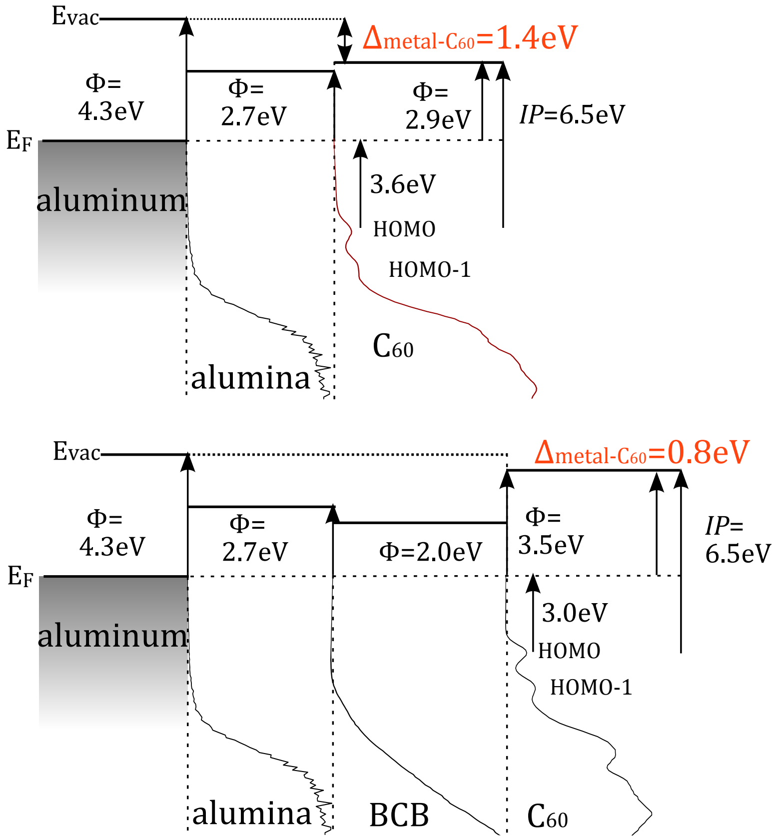

Figure 3.17: Energy diagram of (top) alumina-C_{60} and (bottom) alumina-BCB-C_{60} as measured by PES. Note that all DOS spectra are experimental results by a careful layer-by-layer analysis. As indicated BCB actually shifts C_{60} levels upwards back to a situation as found at e.g. p-Si seen in figure 2.8. The dipole at the organic-organic interface is reduced, compared to the offset between metal-C_{60} the valence levels differ by 0.6 eV.

As clearly seen in figure 3.16 the valence band spectra and the secondary electron cutoff are shifted towards lower binding energies in case of the BCB-structure. The shift is reflected concomitantly in the HOMO (indicated) and in the work function. A crosscheck for the ionization potential yields just minor changes. The energy diagram for the BCB device is compared to the alumina structure underneath in figure 3.17. The energetic structure with BCB interlayer compensates the huge dipole formed before without BCB. The interlayer re-establishes the situation found for the case with p-Si and C_{60}. The results obtained by UPS are distinctive. A 0.6 eV shift induced by a thin organic interlayer is a huge effect. A question mark remains still on the probing system, whether the experiment is performed at thermodynamic equilibrium or not. The energy level analysis is extended to core electrons. Here the Al 2p peak (or the Si 2p peak) is referenced to a literature value [74]. Therefore charging effect can be excluded. With increasing kinetic energy starting with secondary electrons (4-5 eV) up to valence electrons (20 eV) an equal dipole-induced shift is observed. Core electrons (around 280 eV) should reflect the same trend. Since a second excitation source is available (Mg K_α), the changes in the deeper levels are checked as well. For C_{60} as an elementary form of carbon it is convenient to probe changes in the C s1-feature. In this case, the chemical surrounding - the chemical shift - correlates to the dipoles found in UPS. XPS spectra of the C 1s peak of complementary MIS structures are recorded and compared with and without the BCB interlayer, seen in figure 3.18. The peak for the BCB structure has a maximum at lower binding energy. The magnitude for the dipole in the valence levels is not reflected, anyhow the trend of the shift is the same.

The reduced difference in the energy can be explained by the reduced sensitivity of the XPS. The changes are less than 0.1% of the excitation energy. In additon the mean free path for electrons probably exceeds the C_{60} layer thickness for XPS. Contributions of underlying layers might become visible, even if the surface-sensitivity is increased by scanning at 45° off normal emission. The changes, however, correlate to the results obtained by UPS. To sum up, the dipole induced shift is found at the sencondary electron cutoff, at the valence levels and at higher kinetic energies in the C 1s feature of the fullerene.

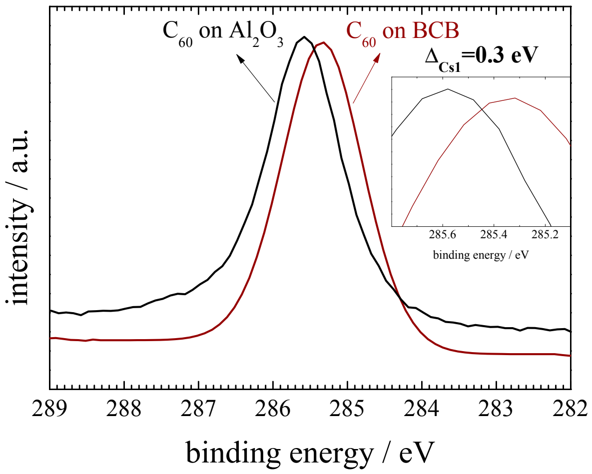

Figure 3.18: C 1s peak (detailed spectra) of C_{60} on BCB and alumina. From the maxima a shift by 0.3 eV is observed, which corresponds to the changes oberserved in the lower energy region (valence bands and cutoff by UPS). The peak at the alumina junction has a lower binding energy.

3.2.3 OFET characterization

Current voltage (IV) characteristics of organic field effect transistors are measured using an Agilent E187 double source unit. The OFET contact areas are connected to the source meter using spring contacts and silver paste. IV-characteristics are recorded either at constant gate voltages (output) and at constant drain voltages (transfer). The IVs of a typical C_{60} -based FET is presented in figure 3.19. The output curves increase first linearly to a certain point, at which they saturate. The segue from linear to saturation is described as the pinch-off point, which is seen in figure 3.19 and defined as follows:

$$U_{drain} = U_{gate} - U_{th} \tag{3.1}$$

In the figure pinch-off points at several gate voltages are connected (red line). The curve follows a parabola. The left upper side is the linear regime, the right side is the saturation regime.

At drain voltages below the pinch-off point ($U_{drain} < U_{gate} - U_{th}$), the channel formed is homogeneous. The IVs have ohmic behavior, therefore this region is called the ”linear regime”. Beyond the pinch-off point, the channel is non-homogeneous, the field distribution causes a pinch-off of the channel and a formation of a depletion-region. The IVs saturate. Increasing the drain voltage U_{drain} will not influence the current. The carrier distribution in all the regimes and the pinch-off is schematically drawn in figure 3.20.

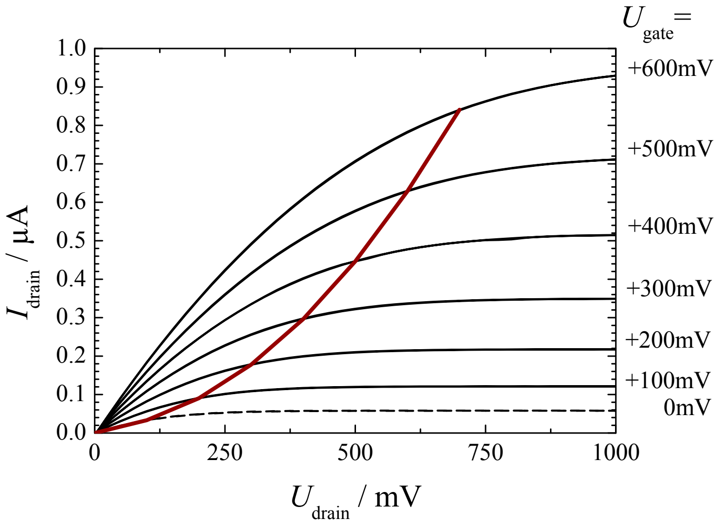

Figure 3.19: Output *IV*s of C_{60} -based FET at different gate voltages. Note the parabolic red line at the pinch-off point separating the linear from the saturated regime.

For the linear regime the transistor current is following a simple formula with the geometric capacitance C_i, mobility μ and channel length L and width W (material and geometric parameters) and the voltages applied (U_{drain} and U_{gate}). The threshold voltage U_{th} will be discussed later.

$$I_{drain} = \frac{W}{L} \cdot \mathrm{C_i} \cdot \mu \cdot U_{drain} \cdot (U_{gate} - U_{th}) \tag{3.2}$$

The formula for the linear regime is derived from the drift equation for classic semiconductors in equation 3.3.

$$\sigma = eN_{\mathrm{e}^-} \cdot \mu \tag{3.3}$$

σ is the sheet conductivity, $\mathrm{eN_{e^-}}$ the carrier concentration and μ the moblity. In an OFET the carrier concentration is determined by the gate voltage applied.

$$eN_{\mathrm{e}^-} = C_i \cdot (U_{gate} - U_{th}) \tag{3.4}$$

The current from source to drain (I_{drain}) is then a function of carrier concentration and the field across the electrodes (U_{drain}).

$$\sigma = \frac{L}{W} \cdot \frac{I_{drain}}{U_{drain}} = C_i \cdot (U_{gate} - U_{th}) \cdot \mu \tag{3.5}$$

The transfer curve for the OFET presented in figure 3.21 follows the formula with some minor deviations: In the inset, a linear increase of the current as a func-

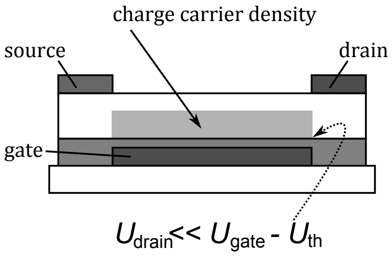

a) linear regime

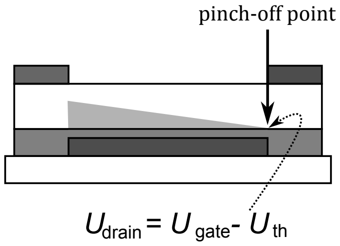

b) pinch-off point

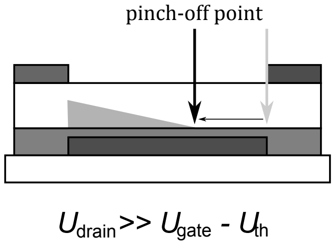

c) saturation regime

Figure 3.20: Schematic of the charge carrier distribution (a) in the linear regime, (b) at the pinch-off point and (c) in the saturated region.

tion of the gate voltage applied is observed. Two parameters are left to be determined: mobility and threshold voltage.

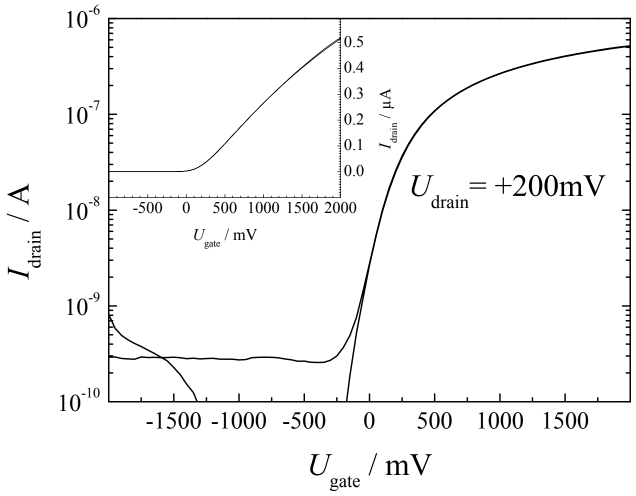

Figure 3.21: Transfer *IV* of C_{60} - based FET exhibiting an on/off ratio of 10^4 within several 100 mV. The inset shows the linear increase of the current as a function of the gate voltage U_{gate} applied.

3.2.4 Deriving threshold voltage and mobility

*IV*s from OFETs allow the extraction of the charge carrier mobility and the threshold voltage U_{th}. In this work all parameters are extracted from the linear regime in OFETs [73]. In order to avoid artifacts from inhomogeneities in the saturation region, drain voltages are kept one order of magnitude lower than gate voltages applied see figure 3.20.

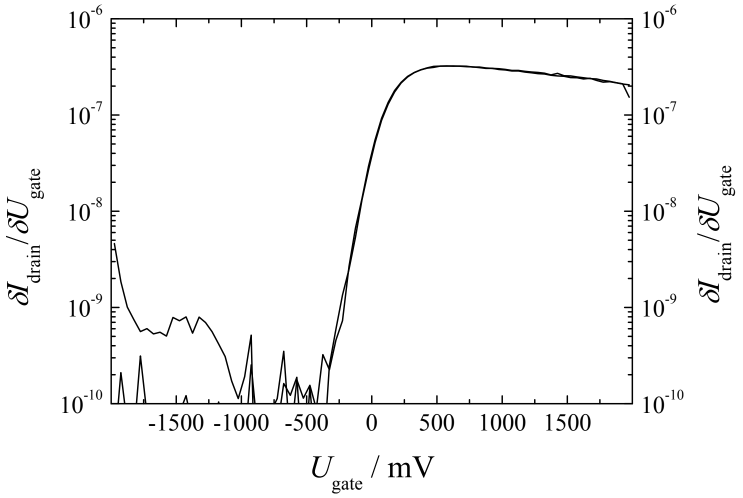

Figure 3.22: First derivative of the transfer *IV*. In the accumulation regime the plateau corresponds to the mobility of the organic semiconductor.

For the extraction of the threshold voltage U_{th} a transfer characteristic is recorded, which is depicted in figure 3.21. The threshold voltage is defined as the point, at which the transistor turns from the depletion (off) to the accumulation (on) mode. This is seen in the graph by a linear increase of the current at positive gate voltages. Ideally π-conjugated molecules are intrinsic semiconductors and therefore the threshold voltage is defined from the interfacial properties at the semiconductor-dielectric interface. It will be shown in this work, that dipoles are formed at interfaces [22]. They control the energy level alignment and consequently parameters like the threshold voltage in an interfacial driven device as field-effect transistors. In order to extract the threshold voltage U_{th}, the second derivative (SD) method is used, which is applied in the linear region as for the threshold voltage extraction [75]. Mobility can be read out from a transfer *IV* as well.

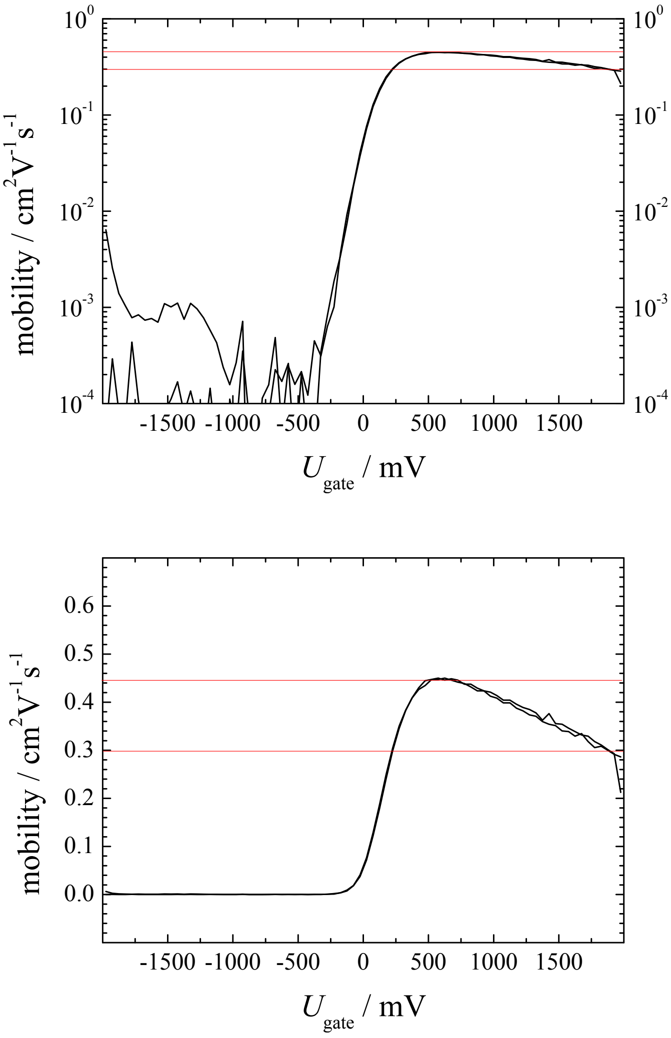

Figure 3.23: Semilogarithmic and linear plot of the mobility as a function of the gate voltage. The method in the linear regime gives a approximation for the charge carrier mobility of C_{60}.

In figure 3.22 the first derivative of the transfer curve is shown. Following the line in the accumulation (positive gate voltage) region, the line should ideally forms a straight line.

$$\frac{\delta I_{drain}}{\delta U_{gate}} = \frac{W}{L} \cdot C_i \cdot \mu \cdot U_{drain} \tag{3.6}$$

Using equation 3.6 the mobility is proportional to the parameter $\frac{\delta I}{\delta U}$. The fact that the derivative is not a constant originates from leakage currents, field-dependent mobility and contact resistances in the OFET. However, for the extraction of the mobility this method serves here as an approximation. The drain voltage U_{drain} is constant, the $\frac{W}{L}$ are geometrical parameters, C_i is the geometric capacitance, for both parameters see section 2.2.4 and 2.2.1. The charge carrier mobility is extracted then as follows:

$$\mu = \frac{\delta I_{drain}}{\delta U_{gate}} \cdot \frac{L}{W} \cdot \frac{1}{C_i \cdot U_{drain}} \tag{3.7}$$

The mobility as a function of the gate voltage is plotted in figure 3.23. In case of C_{60} the mobility value ranges from 0.3 -0.45 $\mathrm{cm^2\,V^{-1}\,s^{-1}}$. The inflection point from the transfer curve (figure 3.21) is considered as a secure characterization of the threshold voltage U_{th}. The peak maximum of the second derivative corresponds to the threshold voltage, the plot with the peak is shown in figure 3.24. In case of C_{60} and BCB the threshold voltage is around zero.

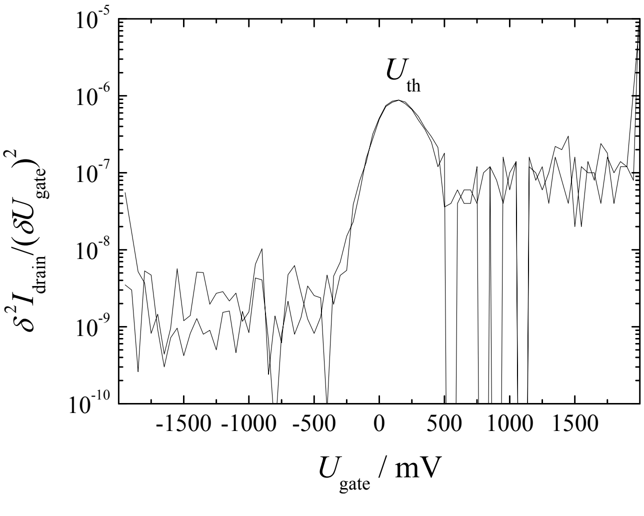

Figure 3.24: Second derivative of transfer *IV* for determination of the inflection point. The peak maximum corresponds to the threshold voltage U_{th}.

3.2.5 Resistivity measurements of OFET

The sheet resistivity of C_{60} during doping is measured as a function of temperature. As already rolled up in the experimental section, a transistor in a 6-probe geometry is used to characterize the potential drops at a constant current I_{drain} applied. Similar to the OFET, the transistor remains in the linear regime: At a given gate voltage U_{gate} (e.g. 30 V) the current saturates above the pinch off point at $U_{gate} - U_{th} = U_{drain}$, which means the current is limited by the gate potential.

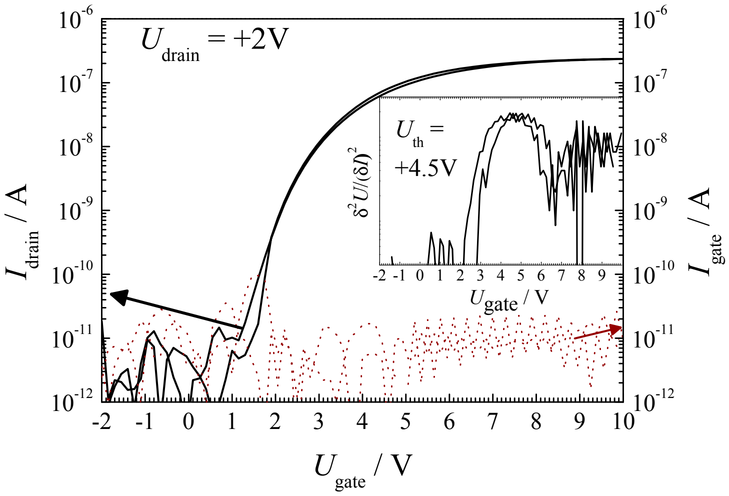

Figure 3.25: The 6-probe FET structure (see figure 2.32 and 2.33 is measured as an OFET (the inner contacts F1-4 are disregarded). The OFET operated with a hight driving voltage coming from the disadvantageous channel geometry (W/L $\leq$ 1, here 0.4). The *IV*s show ideal behaviour. Note the leakage currents (dotted red line, scale right side) close to the noise level of the setup. Inset: Threshold voltage observed at +4.5 V in the linear regime.

The sheet resistivity R_{xx} is measured as a function of the potential drop U_{xx} at the source-drain electrodes. The parameters for deriving the resistivity are set according to the geometry of the sample in figure 2.32:

$$R_{xx} = \frac{area}{length} \cdot \frac{U_{xx}}{I_x} \tag{3.8}$$

Geometrical parameters are set as follows, see table 3.2.5 too: The length is 200 μm, the cross sectional area is 200 μm x 20 nm thickness of the C_{60} film. Here 20 nm of C_{60} were deposited. The current applied was 4μA, the potential drops measured along the 200 μm length ranged between 1 to maximum 12 V. The gate potential U_{gate} is measured at 30V. The threshold voltage for this device is determined from a transfer characteristic, see figure 3.25. The peak maximum (inset) varies between +4.5±0.2 V.

The resistivity is measured between 280 K and 227 K. At the lower temperature (corr. 4.4 1000 K^{-1}) a huge potential drop is observed, which is attributed to a phase transition in C_{60} [76]. Below this point no values were recorded for setup-limitations. The resulting resistivity R_{xx} of C_{60} is plotted as a function of the temperature. The resistivity is measured with and without magnetic field (1 T, perpendicular to the sample plane), the resulting curves are presented in figure 3.26.

parameter	value	unit
gate voltage	30	V
length L	200	μm
cross sectional area $W \cdot d$	200 x 0.02	μm^2
magnetic field B	1	T
upper temperature limit	280	K
lower temperature limit	227	K
applied current I_x	4	μA

From the graph in figure 3.26 a negative organic magneto-resistance effect (neg. OMR effect) is observed. For the curve without magnetic field (black line) the resistivity increases within the measured range by a factor of 10. On the contrary when comparing to the resistivity with magnetic field the observed temperature effect is smaller (red curve). At 280K the resistivity is even slightly higher, after the intersection it remains almost constant until 227K.

The difference in the resistivity can be attributed to a negative OMR effect. The results indicated significant changes induced by the magnetic field. The study here represents a preliminary state of the characterization of disordered organic thin films in an OFET geometry. Anyhow, further experiment at lower temperatures and a wider range of measured potential drops perpendicular and parallel to the current direction might clarify the situation of transport in disordered van-der-Waals type molecular films as here with C_{60}.

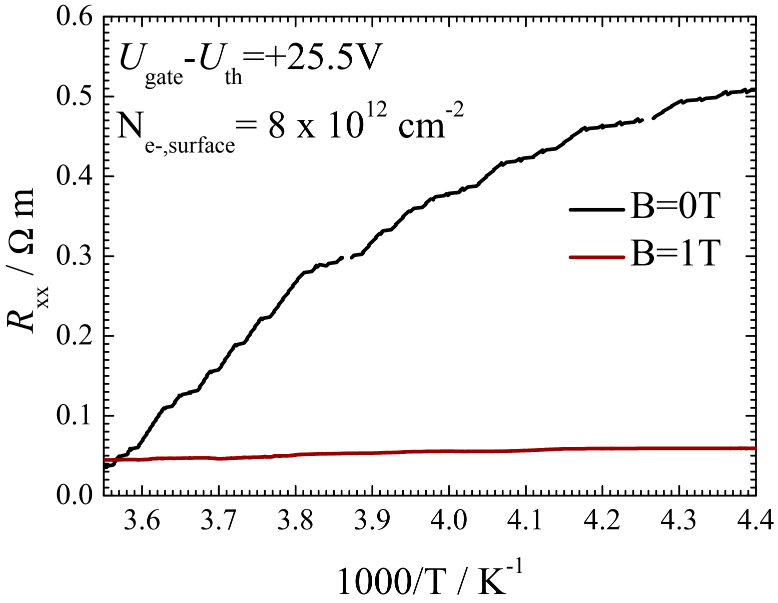

Figure 3.26: 4-probe measurement applied to the OFET presented in figure 3.25 of resistivity versus 1000/T. The OFET was scanned once without magnetic field (black line) and once with magnetic field (red line). A negative OMR effect is oberserved.

3.2.6 Correlation of interfacial dipole with threshold voltage

The energy level analysis at the interface opens the question, how different built-in dipoles influence the performance of an OFET. A direct measure of the OFET performance has to be found, which can be related to the interface analysis investigated with photoemission spectroscopy. In section 3.2.3 parameters and formulas describing the transistor characteristics are introduced and actually two parameters are presented as key issues for OFET performances: Mobility μ and threshold voltage U_{th} (equation 3.2). Mobility on the one hand is considered rather as bulk property of the semiconductor itself, on the contrary the threshold voltage is considered as an interfacial parameter.

Different groups have empirically proven influences of e.g. of the organic interlayer to the threshold voltages [50, 72, 77–80]. Therefore, the very same structures measured by photoemission in the previous section are implemented to an OFET. Transistors with and without BCB interlayers are fabricated. In order to guarantee comparable situations, thin dielectric layers serve as gate insulators and the very same fabrications techniques are applied. The device structures are illustrated in figure 3.27.

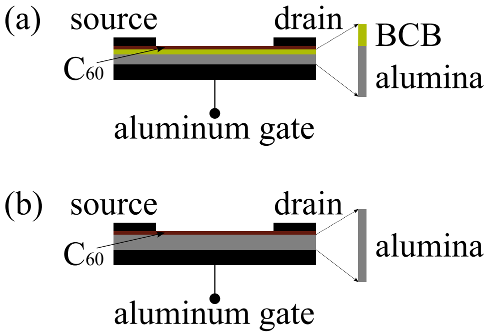

Figure 3.27: Schematic of OFET structures with (a) and without (b) BCB interlayer. Note that both structures have the same geometric capacitance.

The performance of the transistors are demonstrated in figure 3.28 underneath. The transfer characteristics of both structures are plotted, the black line represents the device with BCB, the red line is assigned to the device without BCB. The threshold voltage is extracted then from the transfer *IV*s seen in the corresponding plot with the 2nd derivative and the peak maxima indicated (figure 3.29).

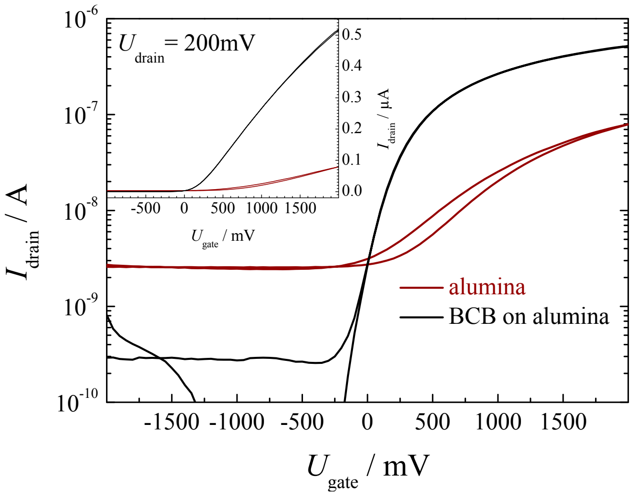

Figure 3.28: Comparison of OFET transfer characteristics with (black) and without (red) BCB in semilogarithmic and (inset) linear plot. The performance drops in terms of lower on/off ratio, arising of hysteresis and apparently higher onset (threshold) for accumulation if BCB is missing.

(a) Sm contact **ΔU_{th} = 0.6 V**

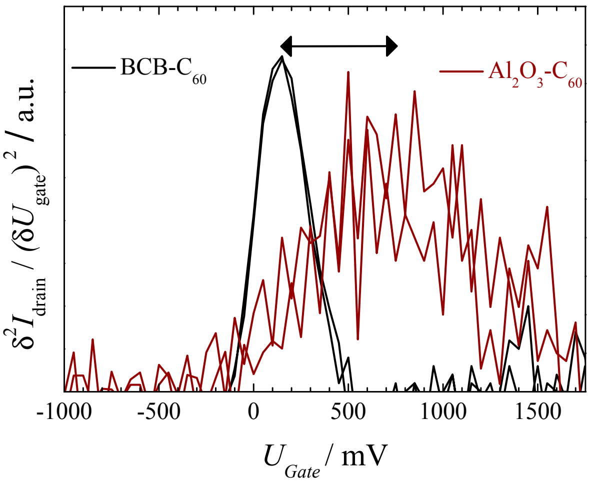

(b) LiF/Al contact **ΔU_{th} = 0.8 V**

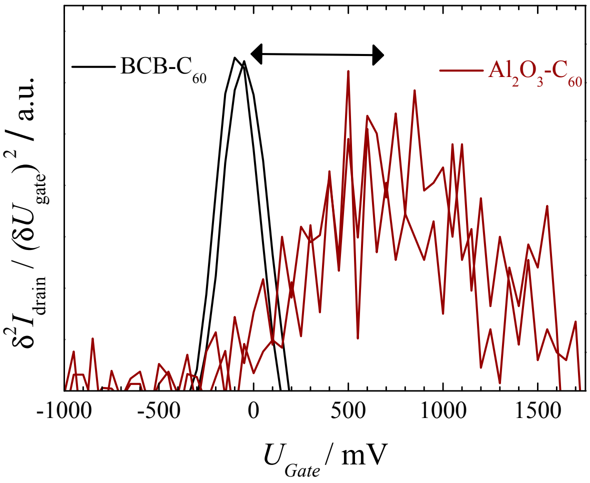

Figure 3.29: Top: 2nd derivative of plot in figure 3.28. The active role of the BCB is visible by the distinct shift of the peak maximum from around 0.7 V down to 0.1 V. Bottom: Crosscheck of 2nd derivative technique [75, 81] when applying a different contact metal (LiF/Al instead of Sm) to the OFET. The shift of the peak maximum from around 0.7 V down to 0 V is more distinctive in an optimized structure. Figure courtesy of Stadler et al. [22].

The results reflect a general performance drop for the alumina-only device. In view of circuit analysis, the on/off ratio is decreased, hysteresis arises and - the important parameter for this study - the threshold voltage shifts by 0.6-0.8 V to more positive values to the right side. In case of the BCB-hybrid structure, the threshold is found around 0 -0.1 V. The alumina only device exhibits a peak maximum around 0.7 V. The peaks are indicated in the graph. The results reflect the results obtained by photoemission. BCB-interlayers introduce a dipole and shift the entire spectra to lower binding energies. In the transistor this is seen by a decrease of the threshold voltage, which is favorable with all aspects of performance analysis.

The study here allows some conclusions for organic interfaces: Dipoles at organic-organic interfaces are usually stronger than between oxide-organic interfaces. The formation of these dipoles can drive organic electronic devices to better performances. The interface study on the organic semiconductor demonstrates a method to measure the role of organic interlayers. The study underlines their active role for interfacial doping: They re-establish the energetic situation as obtained on a metal-semiconductor structure. In view of several literature sources this opens a new insight to interfaces. Organic interlayers are often considered just as passivation layers removing traps from oxide surfaces. Here it is shown, that concrete dipole-dipole interactions are determining the energy level alignment at the interface. Part of the results presented here have been published in organic electronics [22].

3.2.7 In-situ photoemission on an OFET

The interface study combines two different approaches to get information about the energy level alignment. One actual drawback of photoemission studies is the missing information about the unoccupied states. Back in the previous section the MIS structure´s DOS aligned in a distinct way on the hybrid BCB-alumina. The comparison with the threshold voltages has been enabled by only the fact that relative changes Δ in the DOS can be directly adopted to the unoccupied states. The idea is now actively influence the energetic situation by applying a gate voltage and fill up the transport levels (LUMO) and to measure *in-situ* the energetic situation.

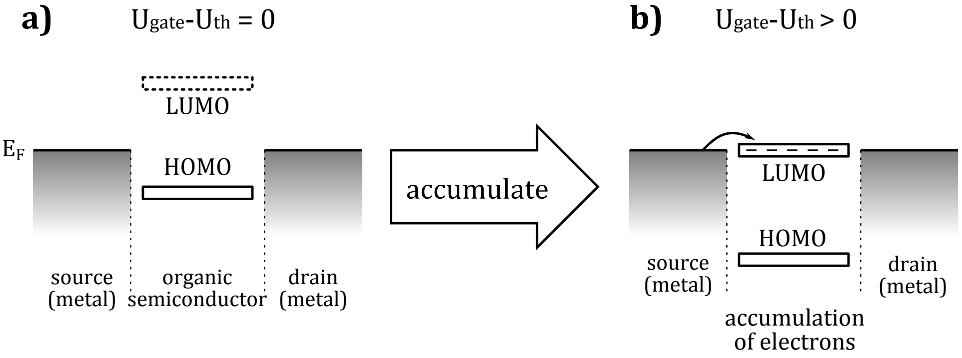

Figure 3.30: (a) OFET at zero potential. The LUMO is indicated, the Fermi level in the ideal case for C_{60} is half of the gap. In (b) the situation after applied bias points at the change in the position of the now ex-LUMO. Charge injection from source is energetically enabled and the semiconductor accumulates with electrons.

In section 2.1.1 the in-situ OFET for the photoemission experiment is introduced. All conditions are fulfilled to derive information about the interface: Well-defined textitfingerprint spectra of ex-situ prepared C_{60} recorded on different thin insulating films. The experiments demonstrated changes by dipole-interactions, which proves the interface sensitivity of the method. The missing part to complete the transistor are the source-drain electrodes on top. Of course, for probing the photoemission spectrum, the excitation by the incident photon-beam has to be confined to the channel region. Contributions from source-drain contacts have to be avoided, therefore they are placed aside at the edge of the sample and contacted with a separated wire. The detailed sample preparation, installation and probing method is presented in the experimental section 2.1.1. The geometry has to be adapted to the spatial resolution of the incident excitation beam in the setup. The beam of the He(I) lamp takes an area of 2 mm^2, therefore the channel length is expanded to 5 mm, which allows some latitude within. At the same time C_{60} layers have to homogeneously cover the surface for an operating transistor and for a meaningful photoemission spectrum. The source-drain contacts are deposited at the edges.

The energetic picture in view of source (=/and drain) splits up into two situations, both depicted in figure 3.30.

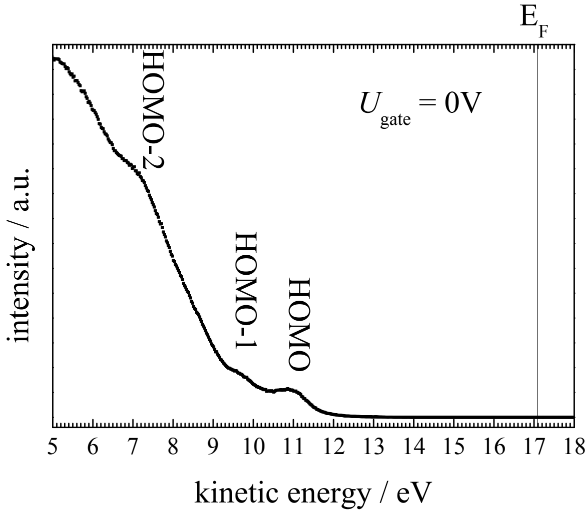

Figure 3.31: Spectrum of C_{60} recorded in the OFET channel. The reference obtained by a metal is rather ill-defined on the gate dielectric. The kinetic energy KE is plotted instead of the binding energy. The reference Fermi energy from the setup is indicated at 17.1 eV. The fingerprint features of C_{60} (HOMO, HOMO-1, HOMO-2) are defined in the valence features of the uppermost C_{60} layer.

In case (a) the LUMO is at a certain energy above the HOMO, the position of the unoccupied states can be estimated by adding the band-gap to the HOMO. The gap energy is obtained by scanning-tunneling-spectroscopy (STS) measurements. Depending on the surface values for the energy vary within 2.5 to 3.6 eV [4, 82–84]. Anyhow, the information is not satisfying and the position of the LUMO not accurate. In (b) after formation of a conductive channel, the position of an - in this case - ex-LUMO is defined, because electrons are injected from the source electrode. Therefore the ex-LUMO has to be close to the Fermi-energy of the metal. The concentration is defined by the gate voltage applied. Exactly the situation depicted here is evoked in a transistor during operation: As a function of the corresponding gate voltages the energy level alignment is recorded with in-situ photoemission spectroscopy. In the first step case (a) is measured, UPS spectra on the OFET structure is presented in figure 3.31.

The fingerprint features of C_{60} are identified (HOMO, HOMO-1, HOMO-2). The peaks are smeared out and shifted to higher kinetic energies, as mentioned the definition of the Fermi edge is ill-defined. In absence of a reference the kinetic energy of electrons is plotted instead. The internal setup reference is indicated in the graph at KE=17.1 eV. When the sample is carefully biased step by step, the transistor channel is accumulated with charge carries and the changes are successively monitored by the UPS. The gate electrode potential - at the same time the Fermi level reference for the organic compounds - is not changed in the entire experiment, the source (and drain) electrode potentials are decreased with respect to gate. Changes observed are attributed to injection of charge carriers to the semiconductor.

The in-situ spectra in figure 3.33 represent UPS scans at different doping concentrations of the fullerene in the channel. The source potentials are stepwise decreased, while the gate electrode - at the same time the reference electrode for the UPS - is kept constant with respect to the spectrometer analyzer. Following the results in figure 3.33, first a reference spectra at 0 V gate is recorded, where C_{60} features as discussed are found. Here in this plot the HOMO is actually shown. When the gate voltage is increased in steps of 5 V, apparently new features arise at higher kinetic energies. The baseline shifts upwards at +5 V. At +10 V potential difference a peak at 16 eV close to the Fermi level is recognized in the magnified curve attached. Until here the intensity of the new features is low compared to the HOMO. The situation is changes at +15 V, where the new feature grow to almost comparable intensity. The Fermi edge is indicated throughout the graph at 17.1 eV from the internal reference.

The results are comparable to potassium doped C_{60} presented by Sakamoto et al. [35], see figure 3.32 especially at low K-concentrations the some analogies are found: In both cases the ex-LUMO arise close to the Fermi edge, actually around 0.5-1 eV below the internal reference. The HOMO position is changed in the same way: First the peak shifts towards the Fermi energy by increasing gate voltages and interestingly turns back partly to higher kinetic energies at higher doping concentrations.

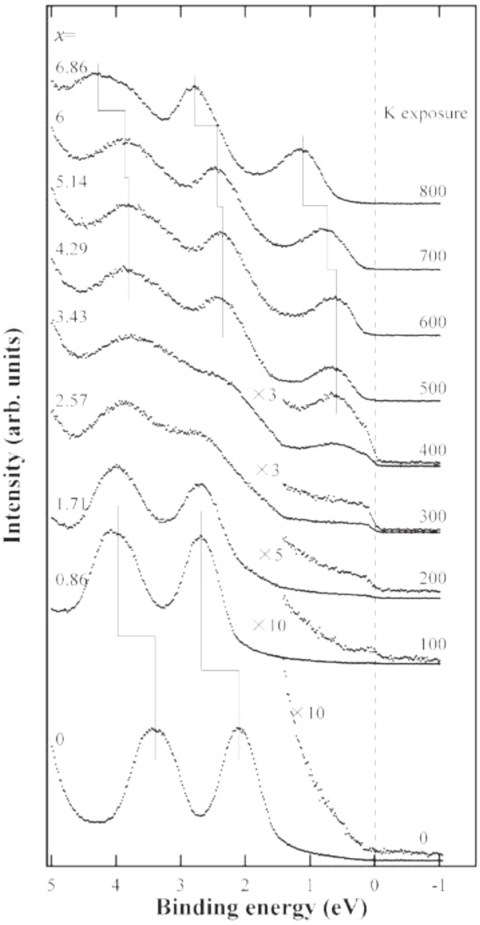

Figure 3.32: After gradual K exposure (time indicated) of C_{60} on Cu-substrate new features are observed close below the Fermi edge. They are attributed to the anion C_{60}^{-1}. The results presented in figure 3.33 for interfacial doping are showing a similar effect. Figure courtesy of Sakamoto et al. [35].

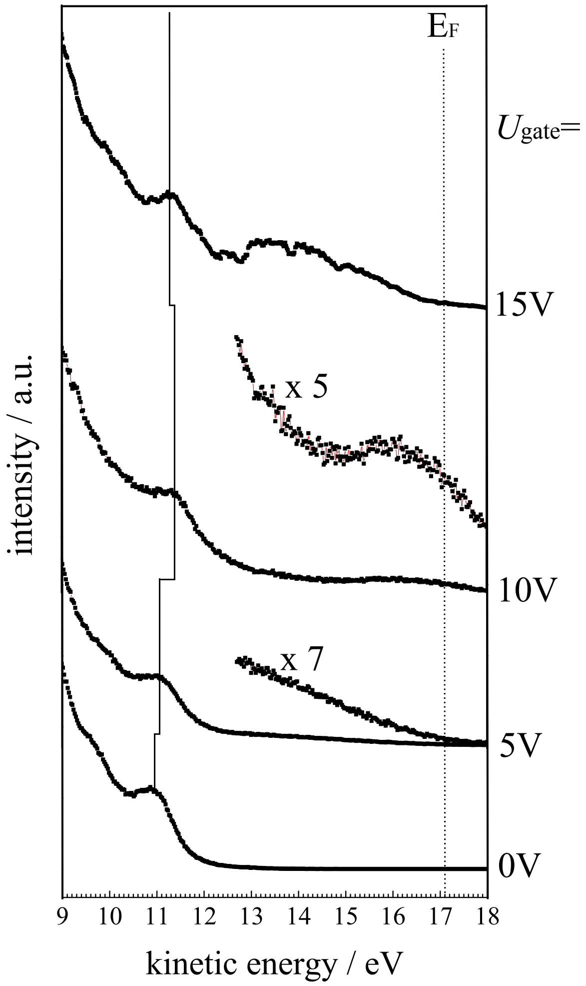

Figure 3.33: Spectrum of C_{60} recorded as a function of the gate voltage applied. After exceeding the threshold of the sample at 5 V a new feature close to the Fermi edge arise. The peak at 16 eV is defined and attributed to the ex-LUMO of the fullerene transport level. The HOMO peak apparently drifts towards the Fermi edge (indicated in the graph). At higher doping concentration the ex-LUMO peak shifts towards the HOMO.

To the authors opinion the in-situ spectra are the transport bands (the ex-LUMO) of fullerene. The feature arises close to the Fermi edge (about 1 eV at KE=16 eV). The experiment is reproduced several times. Although the ex-LUMO is smeared out, a clear peak is observed. When considering the quality of ancestor DOS features in figure 3.31, the peak quality is good. Acutally another reason for the noise level is the sample geometry. The source-drain electrodes act in the in-situ UPS as lense, obviously low-kinetic energy electrons are deflected. Therefore the limit for the gate voltage is set at 15 V (corresponding KE of 15 eV). Anyhow a crosscheck of the reliability of the ex-LUMO feature can be done at 15 V_g. The difference (peak-to-peak) from HOMO to (ex-)LUMO is found at 2.5 to 3 eV, which is in agreement to the results observed by Sakamoto et al. [35] and various other groups Lu et al. [4], David et al. [83], Johansson et al. [84]. The corresponding plot in figure 3.34 is presented underneath.

The fact that unoccupied state become visible in an OFET channel indeed provides an insight to the interfacial doping mechanism. Similar to potassium-doped C_{60} a feature arise close to the Fermi edge. The shifts at increased doping concentrations follow a similar trend, although the exact analysis of the in-situ spectra is not fully developed. From the spectra another issue is clear, which aims at the energy level alignment. Indeed the reference for the semiconductor in the channel is given by the gate electrode solely.

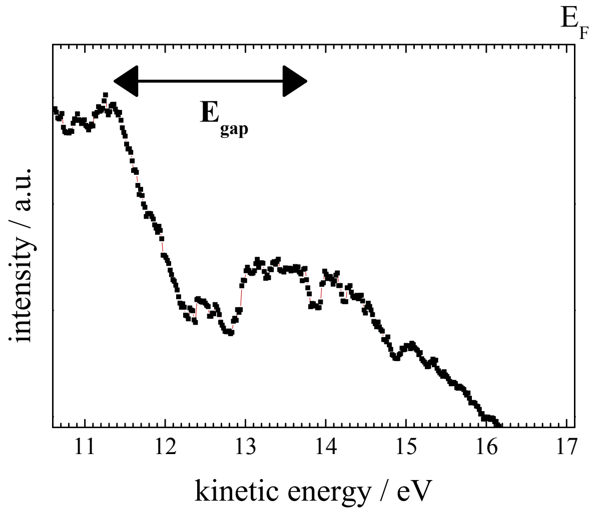

Figure 3.34: Spectrum of C_{60} recorded at U_{gate}= +15V. Two different peaks are observed, thought especially the new feature close to the Fermi energy (17.1 eV) is smeared out, a peak-to-peak value is estimated given at a range between 2.5 to 3 eV. This value is in analogy to results reported in the literature from potassium-doped C_{60} and furthermore in agreement with STS measurements on the E_{gap} on single molecules [4, 83, 84].

Chapter 4

Discussion

A-B type heterojunctions

A number of results on organic heterojunctions have been presented. The first point of contact for a discussion concerns the simplest case of an organic heterostructure - the bilayer. The electronic structure - the density of states - is investigated in this work directly by in-situ photoemission. The technique gives direct access to the uppermost layer of a bilayer heterojunction. The results obtained from the characterization of an interfacial doped transistor channel, where charge carriers are located at the interface, show the presence of free electrons. Ultra-thin films are probed, which are in the range of 2-3 monolayers. The carrier concentration by interfacial doping is in the order of maximum $10^{13}\,\mathrm{cm}^{-2}$. One has to add that the heterojunction (BCB and C_{60}) has been optimized using trap-free interfaces and high-performance hybrid-dielectrics, which allow to apply large fields and large carrier concentrations. The results are seen in the presence of the (earlier) unoccupied states (ex-LUMO).

Organic quantum-well

A different picture is obtained from photo-doped donor-acceptor A-B type bilayer heterostructures. Here obviously free charge carriers are absent, at least the changes in the DOS during photo-excitation are minor. Though the onset of the HOMO shifts slightly towards the Fermi edge, unoccupied states as in the interfacial doped OFET structure are not found in the uppermost C_{60} layers. Thus photo-induced carriers have to be located at the interface, tightly bound. The results are in agreement with different considerations of the exciton binding energies [85]. Once an electron-hole pair is formed at the bilayer heterojunction, apparently no further driving force is present to separate them. At the same time the recombination rate is fast (figure 4.1). The major outcome of the bilayer heterostructure is clear. Photo-excited electron hole-pairs are bond, whereas in an OFET injected carriers are free in the conduction band.

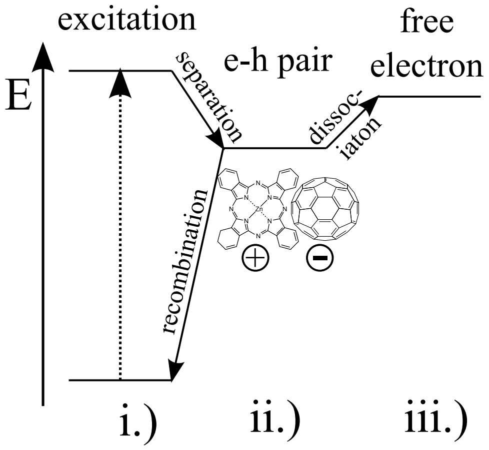

Figure 4.1: Different stages in photoexcited donor-acceptor heterostructure: i.) excitation, ii.) formation of electron-hole pair and iii.) free electron.

When extending the bilayer with an additional donor layer, a potential well structure type donor-acceptor-donor is obtained. In theory in a quantum well (A-B-A) structure, electrons are confined within the barriers V_b (particle in the box). When adapting the structure from inorganic to organic molecules, the well is formed in the conduction bands of the acceptor molecules. Precisely the energy levels of ZnPc and C_{60} form a potential well for electrons and a barrier for holes. A schematic of the organic system is depicted in figure 4.2. In confined systems energy levels would be a function of the box length L. The wave-vector k_w propagating within the well is described by the solution of the wave mechanics. Discrete levels would arise, in well-defined inorganic quantum well structures such features are found in the far and mid infrared. Discussing the results on organic semiconductors the question now is, if free electrons are present in the photo-doped organic heterostructure. Definite no carriers are found in the bilayer, which has to be kept in mind in that case. The triple-layer system differs in one aspect to the bilayer. Indeed it can exhibit a field distribution, which enables charge separation. Internal electrical fields can be high and driving force for that process. In case of charge separation and free electrons, quantum confinement is possible. The potential well is present, since the LUMO of the fullerene is below the one of ZnPc. The potential well can be estimated between 300 - 500 meV for V_b.

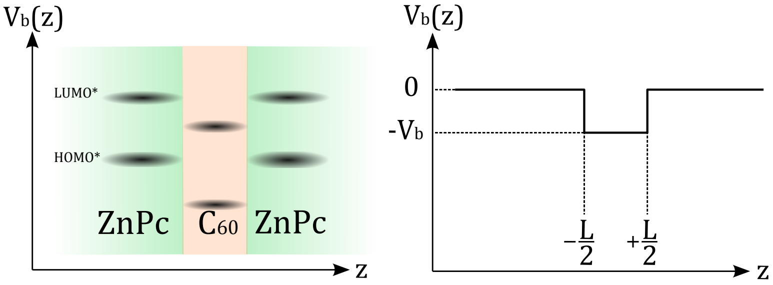

Figure 4.2: Schematic of a layer-by-layer grown potential well structure showing the molecular (left) and the quantum-mechanical energy diagram (right) in z-direction perpendicular to the layer planes.

Organic superlattice

The experiments presented in this work are revealing not only a single donor-acceptor-donor structure, but a multiple stacked layer-by-layer structure. Practically 14 layers are deposited forming a quasi - superlattice. Here due to periodicity Bloch states are introduced (figure 1.4). When assuming that part of all photo-generated carriers are free electrons, effects from quantum confinement could arise. The photo-induced absorption spectra recorded for the mid-IR between 100 - 700 meV exactly target on the observation of quantum confinement. By photo-exciting the donor-acceptor alternating stacked heterostructure a doped multiple potential well structure is formed.

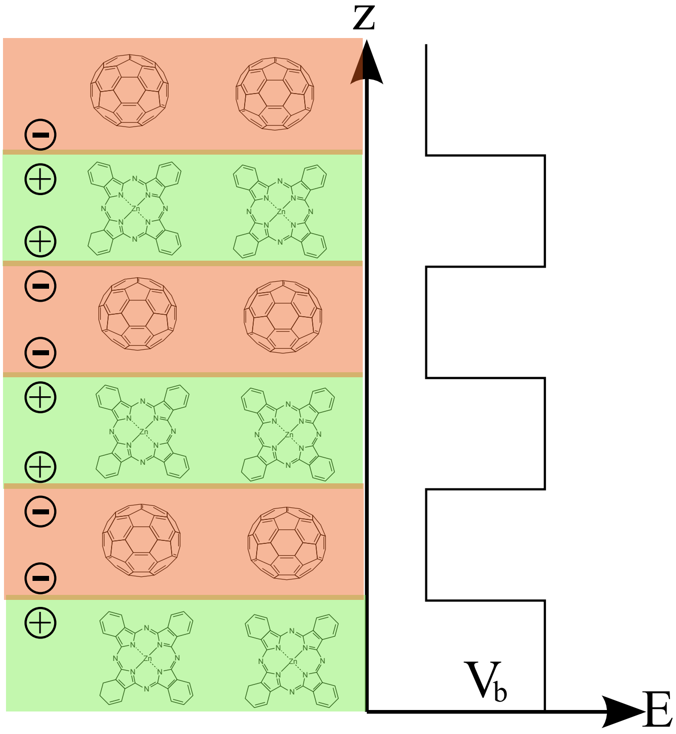

Figure 4.3: Approach for photo-doped quasi-superlattice heterojunction. Alternating layers (left) and potential profile with V_b for the barrier height.

In figure 3.9 actually a broad feature arises with the maximum at around 300 - 400 meV, which is only observed in the superlattice structure. The bulk - heterojunction blend just exhibits noise on the base line.

Anyhow, the onset of the feature is found at around 500 meV. The broadness of the feature is contradicting to the quantum effects discussed. In theory such bands are discrete and sharp. To the authors opinion the superlattice-effect still is evident (figure 4.3), broadness might be introduced due to the nature of organic semiconductors or non-idealities in the heterostructures. The results allow the conclusion, that the order introduced by the layer-by-layer structure affects the electronic properties. One explanation are Bloch levels ε_{qn}. At least energetically the features fit to the ZnPc-C_{60} system. The crucial question is, if free carriers are present. This is speculative from the experiments performed, anyhow further experiments on such quasi-superlattices will give better insight and understanding. Another explanation for the features are polaronic states in the superlattice. Since dipoles are ordered along the z-axis of the quasi-superlattice, a quasi-Bloch effect on polaronic features is possible: In C_{60} usually the polaronic absorptions are found at 500 meV and higher at 1.1 eV. If dipoles now align and interact in a periodic system, the polaron feature could shift to lower energies. The very same effect can be assigned to the ZnPc as well. The shape of the observed superlattice-introduced feature anyhow looks similar to a broad polaron absorption.

Chapter 5

Outlook

At the beginning the motivation in this work was to adapt heterostructures from inorganics to organics. From classic inorganic systems quantum effects such as quantum well structures, superlattices and 2D-effects have been demonstrated. Graphene as the prototype of a 2D system exhibits quantum effects. The author now introduced organic semiconductors for similar structures. Usually organic molecules are not considered for such 2D quantum effect. The crucial part is to introduce free charge carriers to organic systems. Then band transport with high mobilities and maybe even quantum 2D effects are possible. In this work the photo-doped structures have been presented separately from interfacial structures. Future works might merge both techniques, then high carrier concentrations and 2D-electron gases, quantum confinement and superlattices can be realized.

Chapter 6

Curriculum Vitae

Curriculum Vitae

Philipp Stadler

Personal details:

Home: Bluetenstr. 23/164
4040 Linz, Austria
Office: Altenbergerstr. 69
4040 Linz, Austria
Mob:+ 43-650-5150420
e-mail: Philipp.Stadler@jku.at

Education:

04/2007-08/2011 **Doctoral program in engineering and natural sciences:**
Johannes Kepler University Linz, Austria

Topic: “Interfacial effects in organic semiconductor heterojunctions.”

Institute for Physical Chemistry and Linz Institute for Organic Solar Cells (LIOS)

Main focus: surface and interface science, (in-situ) spectroscopy, organic field effect transistors, solid state physics, device physics

09/2000-01/2007 **Diploma program: Technical chemistry and engineering**
Johannes Kepler Universtiy Linz, Austria

Topic for diploma thesis at Linz Institute for Organic Solar Cells (LIOS): “Hysteresis in organic field effect transistors”

Grant from US Airforce labs

Main focus: polymers and bio-inspired materials (DNA) characterized for dielectric layers in organic field effect transistors

Work experience in R&D:

04/2007-08/2011	**Linz Institute for Organic Solar Cells (LIOS) and Institute for Physical Chemistry** Johannes Kepler University Linz, Austria Fabrication of ultra-thin film dielectric for OFET performances at low operation voltages for interfacial and transport studies Dielectric spectroscopy on insulators for FET structures DNA thin-film characterization for OFET structures Fabrication of few molecular layer structures of organic semiconductor molecules for OFETs and alternating hetero-structures Characterization of organic semiconductor hetero-structures during doping by applying in-situ spectroscopy: Light-induced ESR, photo-induced absorption in the FTIR Electrochemical doping and in-situ spectro-electrochemistry on organic molecules AFM, SEM and TEM for morphology studies Cooperation with group of Surface Sciences (Institute for Physics, University of Graz, Austria): Experimental studies by UPS and XPS of ex-situ prepared organic layers together with complementary study with organic field effect transistors. In-situ UPS studies on OFETs Cooperation with group of Material Sciences (Institute for Physics, University of Vienna, Austria): Conductivity (transport) measurements of organic films in OFET structure targeting on observation of Hall-effect.

Other relevant work experience:

2009	**Plastic electronics**, Linz, Austria Surface characterization of polymer nano composits by AFM
06/2005-01/2007	**VAI Siemens, VOEST Alpine**, Volta Redonda, Brazil; Linz, Austria Internships on electrochemical corrosion measurements
2003 & 2004	**DSM Fine Chemicals**, Linz, Austria Analytical quality assurance

Grants for conference participations:

2009-2011 **Grant of University of Linz**

MRS 2010 & 2011 Spring (San Francisco)

2006-2007 **Upper Austrian Government student grant**

ICSM 2006 (Dublin), Optical Probes 2007 (Turku)

2008-2009 **Excellence student support grant of the University of Linz**

MRS 2009 Spring (San Francisco), ICSM 2008 (Recife), E-MRS Spring 2008 & 2009 (both Strasbourg), IWEPNM 2009 (Kirchberg i. Tirol)

Lectures (teaching and undergraduate co-supervision)

2007-2011 **Exercise in Physical Chemistry**

Interactive teaching of basic quantum-mechanics and thermodynamics for bachelor and master program

Master thesis **Supervision of master students at LIOS**

Stefan Schaur (graduated 2010), “Electrochemical doping of pentacene”

Sandra Kogler (graduated 2011), “Charge-modulation spectroscopy”

Stefanie Schlager (ongoing), “Organic Schottky-contacts”

Skills:

Languages:	German – first language
	English – fluent
	Spanish – school knowledge (4 years)
	Portugues – basic knowledge
PC knowledge:	Operating systems: Windows, Linux
	Programmes: MS Office, Origin, ChemDraw, Latex, Inkscape, LabView, TestPoint
Further education:	Curriculum for young academics 2009-2010 (Human resource management Johannes Kepler University)
Driver’s licence:	Car and motorcycle

Interests:

Singing (bass) in jazz chorus “United Voices”
Swimming, hiking, all kind of outdoor activities
Travelling: individual journeys

References:

N. Serdar Sariciftci
Linz Institute for Organic Solar Cells (LIOS)
Institute for Physical Chemistry
Johannes Kepler University Linz
Serdar.Sariciftci@jku.at

Siegfried Bauer
Institute for Applied Physics, Soft Matter Physics
Johannes Kepler University Linz
siegfried.bauer@jku.at

Michael G. Ramsey
Institute for Physics, Surface Science
University Graz
ramsey@uni-graz.at

Reghu Menon
Department of Physics
Indian Institute of Science, Bangalore
rmenon@physics.iisc.ernet.in

List of Publications

Philipp Stadler

Publications:

2011

1. M. Ullah, A. Pivrikas, I. I. Fishchuk, A. Kadashchuk, P. Stadler, C. Simbrunner, N. S. Sariciftci, H. Sitter ”Effect of source-drain electric field on the Meyer-Neldel energy in organic field effect transistors”, *Applied Physics Letters,* accepted
2. B. Meana-Esteban, P. Stadler, S. Schaur, H. Neugebauer, N. S. Sariciftci “Vibronic aspects in p- and n-doping of pentacene”, *Journal of Physical Chemistry A*, in preparation
3. S. Schaur, P. Stadler, B. Meana-Esteban, H. Neugebauer, N. S. Sariciftci “Electrochemical doping for lowering the contact barrier in organic field effect transistors”, *Synthetic metals*, in preparation
4. M. Kaltenbrunner, P. Stadler, A. W. Hassel, N. S. Sariciftci, S. Bauer “Anodized aluminium oxide thin films for low-voltage organic non-volatile memory elements with excellent charge retention” *Advanced Materials*, submitted

2010

5. M. Ullah, I. I. Fishchuk, A. Kadashchuk, P. Stadler, H. Sitter, C. P. Simbrunner, V. N. Poroshin, N. S. Sariciftci, A. Pivrikas “Dependence of Meyer-Neldel energy on energetic disorder in organic field effect transistors”, *Applied Physic Letters*, 96, 213306 (2010)
6. P. Stadler, A. M. Track, M. Ullah, H. Sitter, G. J. Matt, G. Koller, T. B. Singh, H. Neugebauer, N. S. Sariciftci, M. G. Ramsey “The Role of the Dielectric Interface in Organic Transistors: A combined Device and Photoemission Study”, *Organic Electronics*, 11, 207-211 (2010)
7. S. Sangeeth, P. Stadler, S. Schaur, N. S. Sariciftci, R. Menon ”Interfaces and traps in pentacene organic field-effect transistors”, *Journal of Applied Physics*, 108, 117303 (2010)

2009

8. P. Stadler, A. Fuchsbauer, G. Hesser, N. S. Sariciftci, G. J. Matt, H. Neugebauer, T. Fromherz “Negative differential resistance in C60 diodes” *Springer Proceedings in Physics: Interface Controlled Organic Thin Films*, 129, 189 (2009)

2008

9. P. Stadler, G. Hesser, T. Fromherz, G. J. Matt, H. Neugebauer, N. S. Sariciftci ”Current filamentation and negative differential resistance in C60 diodes”, *Physica Statu Solidi (b)*, 245, 2300-2302 (2008)
10. A. Pivrikas, P. Stadler, H. Neugebauer, N. S. Sariciftci ”Substituting the postproduction treatment for bulk-heterojunction solar cells using chemical additives”, *Organic Electronics*, 9, 775 (2008)

2007

11. P. Stadler, K. Oppelt, T. B. Singh, J. G. Grote, R. Schwoediauer, S. Bauer, H. Piglmayer-Brezina, D. Bäuerle, N. S. Sariciftci “Organic field-effect transistors and memory elements using deoxyribonucleic acid (DNA) gate dielectric” *Organic Electronics,* 8, 648-654 (2007)

2005

12. T. B. Singh, N. Marjanovic, P. Stadler, M. Auinger, G. J. Matt, S. Günes, N. S. Sariciftci “Fabrication and characterization of solution-processed methano-fullerene-based organic field-effect transistors” *Journal of Applied Physics*, 97 083714 (2005)

Oral presentations (first author only)

EMRS 2011 Spring Meeting Nice (France)

- P. Stadler, B. Meana-Esteban, S. Schaur, H. Neugebauer, N. Serdar Sariciftci
  ”Electrochemical doping of pentacene: From spectroscopic investigations to application”

MRS 2011 Spring Meeting San Francisco (USA)

- P. Stadler, A. M. Track, H. Neugebauer, G. Koller, M. G. Ramsey, N. Serdar Sariciftci
  ”In-situ photoemission on organic field effect transistors”, (invited)

TPG 2010 Rudolstadt (Germany)

- P. Stadler, A. M. Track, M. Ullah, H. Sitter, G. J. Matt, H. Neugebauer, N. S. Sariciftci, G. Koller, M. G. Ramsey
  ”Correlation between the energy level alignment and device performance in organic heterostructure interfaces”

ICSM 2008 Recife (Brazil)

- P. Stadler, T. B. Singh, T. D. Anthopoulos, H. Yang, L. Yang, N. Marjanovic, G. J. Matt, N. S. Sariciftci, M. Cölle, D. M. de Leeuw, A. M. Ramil, H. Sitter
  ”Integrated circuits based on C60 field effect transistors”

EMRS Spring Meeting 2008 Strasbourg (France)

- P. Stadler, A. Fuchsbauer, A. Pivrikas, H. Neugebauer, N. S. Sariciftci
  ”Current filamentation in C60 diodes”

ICSM 2006 Dublin (Ireland)

- P. Stadler, T. B. Singh, R. Schwoediauer, S. Bauer, J. G. Grote, N. S. Sariciftci
  ”Bio-organic field-effect transistor memory element”

Poster presentation (first author only)

MRS Spring Meeting 2010 San Francisco (USA)

- P. Stadler, A. M. Track, M. Ullah, H. Sitter, G. J. Matt, T. B. Singh, H. Neugebauer, N. S. Sariciftci, G. Koller, M. G. Ramsey
  ”Correlation between organic field effect transistor performance and electronic band level alignment”

MRS Spring Meeting 2009 San Francisco (USA)

- P. Stadler, A. M. Track, M. Ullah, H. Sitter, G. J. Matt, T. B. Singh, H. Neugebauer, N. S. Sariciftci, G. Koller, M. G. Ramsey
  ”Interface engineering in organic thin film transistors”

EMRS Strasbourg 2009 (France)

- P. Stadler, A. M. Track, M. Ullah, H. Sitter, N. S. Sariciftci, M. G. Ramsey
  ”Fermi-level shift in of fullerene by interfacial interactions”

IWEPNM 2009 Kirchberg i. Tirol (Austria)

- P. Stadler, A. M. Track, H. Neugebauer, N. S. Sariciftci, M. G. Ramsey
  ”Energy level alignment at organic-organic interfaces”

Optical Probes 2007 Turku (Finland)

- P. Stadler, G. J. Matt, A. Pivrikas, H. Neugebauer, N. S. Sariciftci ”Morphology and transport studies in evaporated C60 films grown at various substrate temperatures”

DPG Meeting 2007 (Regensburg)

- P. Stadler, T. B. Singh, R. Schwoediauer, S. Bauer, J. G. Grote, N. S. Sariciftci “Hysteresis in bio-organic field-effect transistors”

Chapter 7

Further Reading

L. A. Dissado and J. C. Fothergill. *Electrical Degradation and Breakdown in Polymers*. The Institution of Engineering and Technology, 1992. ISBN 0863411967

F. M. Mirabella, editor. *Internal Reflection Spectroscopy: Theory and Applications.* Marcel Dekker, Inc., New York, 1993. ISBN 0824787307

S. M. Sze. *Semiconductor Devices: Physics and Technology*. John Wiley & Sons, New York, 2nd edition, 2002. ISBN 0471333727

G. Hadziioannou and P. F. van Hutten, editors. *Semiconductiong Polymers: Chemistry, Physic and Engineering.* Wiley-VCH,Weinheim, Germany, 2000. ISBN 3527295070

J. P. Rust and J. J. Fitzgerald, editors. *Dielectric Spectroscopy of Polymeric Materials.* American Chemical Society, Washington DC, 1997. ISBN 0841234868

Z. Bao and J. Locklin, editors. *Organic Field-Effect Transistors.* CRC Press Taylor & Francis Group, Boca Raton, FL 33487-2742, 2007. ISBN 0849380804

F. M. Mirabella and N. J. Harrick. *Internal Reflection Spectroscopy: Review and Supplement.* Harrick Scientific Corp., Ossining, New York, 1985. ISBN 0933946147

N. J. Harrick. *Internal Reflection Spectroscopy.* JohnWiley & Sons, London, 1967. ISBN 0470352507

G. Bastard. *Wave mechanics applied to semiconductor heterostructures.* Halsted Press, New York, 1992. ISBN 2868830927

S.-S. Sun and N. S. Sariciftci. *Organic Photovoltaics Mechanisms, Materials, and Devices.* CRC Press Taylor & Francis Group, Boca Raton, 2005. ISBN 082475963X

N. W. Ashcroft and D. N. Mermin. *Solid State Physics.* Thomson Learning, Toronto, 1976. ISBN 0030839939

H. Klauk, editor. *Organic Electronics, Materials, Manufacturing and Applications.* Wiley-VCH, Weinheim, Germany, 2006. ISBN 3527312641

A. J. Heeger, N. S. Sariciftci, and E. B. Namdas. *Semiconducting and Metallic Polymers.* Oxford University Press Inc., New York, 2010. ISBN 0198528647

Chapter 8

References

[1] G. Bastard. *Wave mechanics applied to semiconductor heterostructures*. Halsted Press, New York, 1992. ISBN 2868830927

[2] H. W. Kroto, J. R. Heath, S. C. O Brian, R. F. Curl, and R. E. Smalley. C60: Buckminsterfullerene. *Science*, 318

[3] N. Troullier and J. L. Martins. Structural and electronic properties of endofullerenes of C60. *Physical Review B*, 46: (1992), 1754–1765. ISSN 01661280. doi:10.1016/S0166-1280(03)00343-9

[4] X. Lu, M. Grobis, K. H. Khoo, S. G. Louie, and M. F. Crommie. Charge transfer and screening in individual C60 molecules on metal substrates: A scanning tunneling spectroscopy and theoretical study. *Physical Review B*, 70: (2004), 115418. doi:10.1103/PhysRevB.70.115418

[5] A. Maxwell. C 1s ionisation potential and energy referencing for solid C60 films on metal surfaces. *Chemical Physics Letters*, 260: (1996), 71–77. ISSN 00092614. doi:10.1016/0009-2614(96)00837-8

[6] M. W. Ruckman, B. Xia, and S. L. Qiu. Adsorption of C60 on Ta(110): Photoemission and C K-edge studies. *Physical Review B*, 48: (1993), 15457

[7] R. C. Haddon. Electronic structure, conductivity and superconductivity of alkali metal doped (C60). *Accounts of Chemical Research*, 25: (1992), 127–133. ISSN 0001-4842. doi:10.1021/ar00015a005

[8] K. Jobst, L. Sawtschenko, G. Paasch, and J. Fink. Electrochemical doping of C60 in the solid state. *Synthetic Metals*, 56: (1993), 3179–3184. ISSN 0379-6779. doi:DOI:10.1016/0379-6779(93)90099-I

[9] H. Neugebauer, C. Kvarnstrom, H. Sitter, C. Jogl, H. Kuzmany, and N. S. Sariciftci. In situ ATR-FTIR spectroelectrochemical comparison of pristine and polymerized C60 films. *AIP Conference Proceedings*, 486: (1999), 16–19. doi:10.1063/1.59848

[10] N. S. Sariciftci, L. Smilowitz, A. J. Heeger, and F. Wudl. Photoinduced electron transfer from a conducting polymer to buckminsterfullerene. *Science (New York, N.Y.)*, 258: (1992), 1474–6. ISSN 0036-8075. doi: 10.1126/science.258.5087.1474

[11] G. Yu, J. Gao, J. C. Hummelen, F. Wudl, and A. J. Heeger. Polymer Photovoltaic Cells: Enhanced Efficiencies via a Network of Internal Donor-Acceptor Heterojunctions. *Science*, 270: (1995), 1789–1791. doi:10.1126/science.270.5243.1789

[12] C. J. Brabec, N. S. Sariciftci, and J. C. Hummelen. Plastic Solar Cells. *Advanced Functional Materials*, 11: (2001), 15–26. ISSN 1616301X. doi: 10.1002/1616-3028(200102)11:1⟨15::AID-ADFM15⟩3.3.CO;2-1

[13] T. D. Anthopoulos, T. B. Singh, N. Marjanovic, N. S. Sariciftci, A. Montaigne Ramil, H. Sitter, M. Coelle, and D. M. de Leeuw. High performance n-channel organic field-effect transistors and ring oscillators based on C60 fullerene films. *Applied Physics Letters*, 89: (2006), 213504. ISSN 00036951. doi:10.1063/1.2387892

[14] T. B. Singh, N. S. Sariciftci, H. Yang, L. Yang, B. Plochberger, and H. Sitter. Correlation of crystalline and structural properties of C60 thin films grown at various temperature with charge carrier mobility. *Applied Physics Letters*, 90: (2007), 213512. ISSN 00036951. doi:10.1063/1.2743386

[15] M. Ullah, I. I. Fishchuk, A. Kadashchuk, P. Stadler, A. Pivrikas, C. Simbrunner, V. N. Poroshin, N. S. Sariciftci, and H. Sitter. Dependence of Meyer Neldel energy on energetic disorder in organic field effect transistors. *Applied Physics Letters*, 96: (2010), 213306. ISSN 00036951. doi: 10.1063/1.3435477

[16] C. W. Tang. Two-layer organic photovoltaic cell. *Applied Physics Letters*, 48: (1986), 183. ISSN 00036951. doi:10.1063/1.96937

[17] J. Dai, X. Jiang, H. Wang, and D. Yan. Organic photovoltaic cells with near infrared absorption spectrum. *Applied Physics Letters*, 91: (2007), 253503. ISSN 00036951. doi:10.1063/1.2824836

[18] X. Peng, G. Horowitz, D. Fichou, and F. Garnier. All-organic thin-film transistors made of alpha-sexithienyl semiconducting and various polymeric insulating layers. *Journal of Applied Physics*, 57: (1990), 2013–2015

[19] G. Horowitz. *Organic field-effect transistors*, chapter 2, pages 73–103. CRC Press Taylor & Francis Group, 2007. ISBN 0849380804

[20] G. Horowitz. *Organic Transistors*, chapter 1. Wiley-VCH, Weinheim, Germany, 2006. ISBN 3527312641

[21] T. B. Singh and N. S. Sariciftci. Progress in Plastic Electronics Devices. *Annual Review of Materials Research*, 36: (2006), 199–230. ISSN 1531-7331. doi:10.1146/annurev.matsci.36.022805.094757

[22] P. Stadler, A. M. Track, M. Ullah, H. Sitter, G. J. Matt, G. Koller, T. B. Singh, H. Neugebauer, N. S. Sariciftci, and M. G. Ramsey. The role of the dielectric interface in organic transistors: A combined device and photoemission study. *Organic Electronics*, 11: (2010), 207–211. ISSN 15661199. doi:10.1016/j.orgel.2009.10.017

[23] H. Sirringhaus. Device Physics of Solution-Processed Organic Field-Effect Transistors. *Advanced Materials*, 17: (2005), 2411–2425. ISSN 0935-9648. doi:10.1002/adma.200501152

[24] T. B. Singh, N. Marjanovic, G. J. Matt, S. Günes, N. S. Sariciftci, A. Montaigne Ramil, A. Andreev, H. Sitter, R. Schwödiauer, and S. Bauer. High-mobility -channel organic field-effect transistors based on epitaxially grown C films. *Organic Electronics*, 6: (2005), 105–110. ISSN 15661199. doi:10.1016/j.orgel.2005.03.006

[25] L.-L. Chua, P. K. H. Ho, H. Sirringhaus, and R. H. Friend. High-stability ultrathin spin-on benzocyclobutene gate dielectric for polymer field-effect transistors. *Applied Physics Letters*, 84: (2004), 3400. ISSN 00036951. doi:10.1063/1.1710716

[26] S. Ogawa, Y. Kimura, M. Niwano, and H. Ishii. Trap elimination and injection switching at organic field effect transistor by inserting an alkane (C44H90) layer. *Applied Physics Letters*, 90: (2007), 033504. ISSN 00036951. doi:10.1063/1.2431713

[27] M. Kraus, S. Haug, W. Brütting, and A. Opitz. Achievement of balanced electron and hole mobility in copper-phthalocyanine field-effect transistors by using a crystalline aliphatic passivation layer. *Organic Electronics*, 12: (2011), 731–735. ISSN 15661199. doi:10.1016/j.orgel.2011.02.001

[28] M. Irimia-Vladu, N. Marjanovic, M. Bodea, G. Hernandez-Sosa, A. M. Ramil, R. Schwödiauer, S. Bauer, N. S. Sariciftci, and F. Nüesch. Small-molecule vacuum processed melamine-C60, organic field-effect transistors. *Organic Electronics*, 10: (2009), 408–415. ISSN 15661199. doi:10.1016/j.orgel.2009.01.002

[29] H. Klauk, U. Zschieschang, J. Pflaum, and M. Halik. Ultralow-power organic complementary circuits. *Nature*, 445: (2007), 745–8. ISSN 1476-4687. doi:10.1038/nature05533

[30] U. Zschieschang, M. Halik, and H. Klauk. Microcontact-printed self-assembled monolayers as ultrathin gate dielectrics in organic thin-film tran-

sistors and complementary circuits. *Langmuir*, 24: (2008), 1665–9. ISSN 0743-7463. doi:10.1021/la703818d

[31] T. Sekitani, T. Yokota, U. Zschieschang, H. Klauk, S. Bauer, K. Takeuchi, M. Takamiya, T. Sakurai, and T. Someya. Organic nonvolatile memory transistors for flexible sensor arrays. *Science*, 326: (2009), 1516–9. ISSN 1095-9203. doi:10.1126/science.1179963

[32] L. Miozzo, A. Yassar, and G. Horowitz. Surface engineering for high performance organic electronic devices: the chemical approach. *Journal of Materials Chemistry*, 20: (2010), 2513. ISSN 0959-9428. doi:10.1039/b922385a

[33] K. Oura, V. G. Lifshits, A. A. Saranin, A. V. Zotov, and M. Katayama. *Surface Science: An Introduction*. Springer-v edition, 2003

[34] M. P. Seah and W. A. Dench. *Surface and Interface Analysis*. 1979

[35] K. Sakamoto, T. Wakita, D. Kondo, A. Harasawa, T. Kinoshita, W. Uchida, and A. Kasuya. Electronic structure of K-doped C60 monolayer films adsorbed on Si(0 0 1)-(2x1) and Si(1 1 1)-(7x7) surfaces. *Surface Science*, 499: (2002), 63–72. ISSN 0039-6028. doi:DOI:10.1016/S0039-6028(01)01794-0

[36] C. Cepek, P. Schiavuta, M. Sancrotti, and M. Pedio. Photoemission study of C60/Si(111) adsorption as a function of coverage and annealing temperature. *Physical Review B*, 60: (1999), 2068–2073. ISSN 0163-1829. doi:10.1103/PhysRevB.60.2068

[37] T. Matsui, Z. V. Vardeny, A. Agrawal, A. Nahata, and R. Menon. Resonantly-enhanced transmission through a periodic array of subwavelength apertures in heavily-doped conducting polymer films. *Applied Physics Letters*, 88: (2006), 071101. ISSN 00036951. doi:10.1063/1.2175482

[38] P. A. Lane, J. Rostalski, C. Giebeler, S. J. Martin, D. D. C. Bradley, and D. Meissner. Electroabsorption studies of phthalocyanine/perylene solar cells. *Solar Energy Materials and Solar Cells*, 63: (2000), 3–13. ISSN 09270248. doi:10.1016/S0927-0248(00)00013-1

[39] M. C. Scharber. *Magnetic resonance studies on conjugated polymers and conjugated polymer fullerene mixtures*. Dissertation, Johannes Kepler University Linz, 2002

[40] A. W. Hassel and D. Diesing. Breakdown of ultrathin anodic valve metal oxide films in metal-insulator-metal-contacts compared with metal-insulator-electrolyte contacts. *Thin Solid Films*, 414: (2002), 296–303. ISSN 00406090. doi:10.1016/S0040-6090(02)00453-4

[41] M. J. Esplandiu, E. M. Patrito, and V. A. Macagno. Characterization of hafnium anodic oxide films: An AC impedance investigation. *Electrochimica Acta*, 40: (1995), 809–815

[42] M. M. Lohrengel. Thin anodic oxide layers on aluminium and other valve metals: high field regime. *Materials Science and Engineering*, 11: (1993), 243–294. ISSN 0927-796X. doi:DOI:10.1016/0927-796X(93)90005-N

[43] L. A. Majewski. A novel gate insulator for flexible electronics. *Organic Electronics*, 4: (2003), 27–32. ISSN 15661199. doi:10.1016/S1566-1199(03)00005-3

[44] L. A. Majewski, R. Schroeder, M. Voigt, and M. Grell. High performance organic transistors on cheap, commercial substrates. *Journal of Physics D: Applied Physics*, 37: (2004), 3367–3372. ISSN 0022-3727. doi:10.1088/0022-3727/37/24/003

[45] L. A. Majewski, R. Schroeder, and M. Grell. One Volt Organic Transistor. *Advanced Materials*, 17: (2005), 192–196. ISSN 0935-9648. doi:10.1002/adma.200400809

[46] A. W. Hassel and M. M. Lohrengel. Initial stages of cathodic breakdown of thin anodic aluminium oxide films. *Electrochimica Acta*, 40: (1995), 433–437

[47] J. W. Diggle, T. C. Downie, and C. W. Goulding. Anodic oxide films on aluminum. *Chemical Reviews*, 69: (1969), 365–405. ISSN 0009-2665. doi:10.1021/cr60259a005

[48] D. R. Lide, editor. *Handbook of Chemistry and Physics*. CRC Press Taylor & Francis Group, 82nd edition, 2001. ISBN 0849304814

[49] X.-H. Zhang, B. Domercq, and B. Kippelen. High-performance and electrically stable C60 organic field-effect transistors. *Applied Physics Letters*, 91: (2007), 092114. ISSN 00036951. doi:10.1063/1.2778472

[50] X. Zhang and B. Kippelen. Low-voltage C 60 organic field-effect transistors with high mobility and low contact resistance. *Applied Physics*, 93: (2008), 13305. doi:10.1063/1.2993349

[51] M. E. Mills, P. Townsend, D. Castillo, S. Martin, and A. Achen. Benzocyclobutene (DVS-BCB) polymer as an interlayer dielectric (ILD) material. *Microelectronic Engineering*, 33: (1997), 327–334. ISSN 01679317. doi:10.1016/S0167-9317(96)00061-5

[52] A. Modafe, N. Ghalichechian, M. Powers, M. Khbeis, and R. Ghodssi. Embedded benzocyclobutene in silicon: An integrated fabrication process for electrical and thermal isolation in MEMS. *Microelectronic Engineering*, 82: (2005), 154–167. ISSN 01679317. doi:10.1016/j.mee.2005.07.005

[53] M. Kaltenbrunner, P. Stadler, R. Schwödiauer, A. W. Hassel, N. S. Sariciftci, and S. Bauer. Anodized aluminum oxide thin films for low-voltage organic

nonvolatile memory elements with excellent charge retention. *Advanced Materials submitted*

[54] C. J. Brabec, S. E. Shaheen, C. Winder, N. S. Sariciftci, and P. Denk. Effect of LiF/metal electrodes on the performance of plastic solar cells. *Applied Physics Letters*, 80: (2002), 1288. ISSN 00036951. doi:10.1063/1.1446988

[55] Z. B. Wang, M. G. Helander, M. T. Greiner, J. Qiu, and Z. H. Lu. Energy-level alignment and charge injection at metal/C60/organic interfaces. *Applied Physics Letters*, 95: (2009), 043302. ISSN 00036951. doi:10.1063/1.3189176

[56] M. G. Helander, Z. B. Wang, and Z. H. Lu. Contact formation at the C60/alkali-metal fluoride/Al interface. *Applied Physics Letters*, 93: (2008), 083311. ISSN 00036951. doi:10.1063/1.2976307

[57] M. Lenes, G.-J. A. H. Wetzelaer, F. B. Kooistra, S. C. Veenstra, J. C. Hummelen, and P. W. M. Blom. Fullerene Bisadducts for Enhanced Open-Circuit Voltages and Efficiencies in Polymer Solar Cells. *Advanced Materials*, 20: (2008), 2116–2119. ISSN 09359648. doi:10.1002/adma.200702438

[58] D. Claves, Y. Ksari, G. Chouteau, A. Collomb, and P. Touzain. Samarium-based fullerides. *Solid State Communications*, 99: (1996), 359–361

[59] A. A. Dakhel. Dielectric and optical properties of samarium oxide thin films. *Journal of alloys and compounds*, 365: (2003), 233–239. ISSN 0925-8388

[60] A. K. Sharma, A. W. Hahn, and M. F. Nichols. Optimizing poly(chloro-p-xylylene) or parylene C synthesis. *Journal of Applied Polymer Science*, 36: (1988), 1555–1565. ISSN 1097-4628. doi:10.1002/app.1988.070360704

[61] M. Brumbach, D. Placencia, and N. Armstrong. Titanyl Phthalocyanine/C60 Heterojunctions: Band-Edge Offsets and Photovoltaic Device Performance. *Journal of Physical Chemistry C*, 112: (2008), 3142–3151. ISSN 1932-7447. doi:10.1021/jp0772171

[62] T. Nojiri, M. M. Alam, H. Konami, A. Watanabe, and O. Ito. Photoinduced Electron Transfer from Phthalocyanines to Fullerenes (C60 and C70). *The Journal of Physical Chemistry A*, 101: (1997), 7943–7947. ISSN 1089-5639. doi:10.1021/jp9714734

[63] T. Tsuzuki, Y. Shirota, J. Rostalski, and D. Meissner. The effect of fullerene doping on photoelectric conversion using titanyl phthalocyanine and a perylene pigment. *Solar Energy Materials and Solar Cells*, 61: (2000), 1–8. ISSN 09270248. doi:10.1016/S0927-0248(99)00091-4

[64] D. Gebeyehu. Bulk-heterojunction photovoltaic devices based on donor acceptor organic small molecule blends. *Solar Energy Materials and Solar*

Cells, 79: (2003), 81–92. ISSN 09270248. doi:10.1016/S0927-0248(02)00369-0

[65] G. Zoriniants, V. Dyakonov, M. Scharber, C. J. Brabec, R. A. J. Janssen, J. C. Hummelen, and N. S. Sariciftci. Light-induced ESR studies in conjugated polymer-fullerene composites. *Synthetic Metals*, 102: (1999), 1241–1242

[66] V. Dyakonov and E. Frankevich. On the role played by polaron pairs in photophysical processes in semiconducting polymers. *Chemical Physics*, 227: (1998), 203–217

[67] J. W. Arbogast, A. P. Darmanyan, C. S. Foote, Y. Rubin, F. N. Diederich, M. M. Alvarez, S. J. Anz, and R. L. Whetten. Photophysical properties of C60. *Journal of Physical Chemistry*, 95: (1991), 11–12

[68] G. J. Matt, T. Fromherz, M. A. Bednorz, S. Zamiri, G. Goncalves, C. Lungenschmied, D. Meissner, H. Sitter, N. S. Sariciftci, C. J. Brabec, and G. Bauer. Fullerene sensitized silicon for near- to mid-infrared light detection. *Advanced Materials*, 22: (2010), 647–50. ISSN 1521-4095. doi:10.1002/adma.200901383

[69] I. G. Hill, A. Rajagopal, A. Kahn, and Y. Hu. Molecular level alignment at organic semiconductor-metal interfaces. *Applied Physics Letters*, 73: (1998), 662–664. doi:10.1063/1.121940

[70] I. G. Hill, D. J. Milliron, J. Schwartz, and A. Kahn. Organic semiconductor interfaces: electronic structure and transport properties. *Applied Surface Science*, 166: (2000), 354–362. doi:10.1016/S0169-4332(00)00449-9

[71] A. Jedaa, M. Burkhardt, U. Zschieschang, H. Klauk, D. Habich, G. Schmid, and M. Halik. The impact of self-assembled monolayer thickness in hybrid gate dielectrics for organic thin-film transistors. *Organic Electronics*, 10: (2009), 1442–1447. ISSN 15661199. doi:10.1016/j.orgel.2009.08.006

[72] L.-l. Chua, J. Zaumseil, J.-F. Chang, and E. C. Ou. General observation of n-type field-effect behaviour in organic semiconductors. *Nature*, 434: (2005), 194–199. doi:10.1038/nature03293.1.

[73] D. Braga and G. Horowitz. High-Performance Organic Field-Effect Transistors. *Advanced Materials*, 21: (2009), 1473–1486. ISSN 09359648. doi:10.1002/adma.200802733

[74] J. F. Moulder, W. F. Stickle, P. E. Sobol, and K. D. Bomben. *Handbook of X-Ray Photoelectronspectroscopy:*. Physical Electronics, 1995. ISBN 096481241X

[75] D. Boudinet, G. Le Blevennec, C. Serbutoviez, J.-M. Verilhac, H. Yan, and G. Horowitz. Contact resistance and threshold voltage extraction in n-channel

organic thin film transistors on plastic substrates. *Journal of Applied Physics*, 105: (2009), 084510. ISSN 00218979. doi:10.1063/1.3110021

[76] H. Peimo, X. Yabo, Z. Xuejia, Z. Xinbin, and L. Wenzhou. Electrical conductivity studies of a pure C 60 single crystal. *Journal of Physics: Condensed Matter*, 5: (1993), 7013

[77] W. Ou-Yang, M. Weis, D. Taguchi, X. Chen, T. Manaka, and M. Iwamoto. Modeling of threshold voltage in pentacene organic field-effect transistors. *Journal of Applied Physics*, 107: (2010), 124506. ISSN 00218979. doi:10.1063/1.3449078

[78] W. Ou-Yang, X. Chen, M. Weis, T. Manaka, and M. Iwamoto. Tuning of Threshold Voltage in Organic Field-Effect Transistor by Dipole Monolayer. *Japanese Journal of Applied Physics*, 49: (2010), 04DK04. ISSN 0021-4922. doi:10.1143/JJAP.49.04DK04

[79] A. Deman and J. Tardy. PMMA - TaO bilayer gate dielectric for low operating voltage organic FETs. *Organic Electronics*, 6: (2005), 78–84. ISSN 15661199. doi:10.1016/j.orgel.2005.03.002

[80] K. P. Pernstich, S. Haas, D. Oberhoff, C. Goldmann, D. J. Gundlach, B. Batlogg, a. N. Rashid, and G. Schitter. Threshold voltage shift in organic field effect transistors by dipole monolayers on the gate insulator. *Journal of Applied Physics*, 96: (2004), 6431. ISSN 00218979. doi:10.1063/1.1810205

[81] A. Ortiz-Conde, F. J. Garcia Sanchez, J. J. Liou, A. Cerdeira, M. Estrada, and Y. Yue. A review of recent MOSFET threshold voltage extraction methods. *Microelectronics Reliability*, 42: (2002), 583–596. ISSN 00262714. doi:10.1016/S0026-2714(02)00027-6

[82] X. Lu, M. Grobis, K. Khoo, S. Louie, and M. F. Crommie. Spatially Mapping the Spectral Density of a Single C60 Molecule. *Physical Review Letters*, 90: (2003), 7–10. ISSN 0031-9007. doi:10.1103/PhysRevLett.90.096802

[83] T. David, J. K. Gimzewski, D. Purdie, B. Reihl, and R. R. Schlittler. Epitaxial growth of C60 on Ag(110) studied by scanning tunneling microscopy and tunneling spectroscopy. *Physical Review B*, 50: (1994), 5810–5813. doi:10.1103/PhysRevB.50.5810

[84] M. K.-J. Johansson, A. J. Maxwell, S. M. Gray, P. A. Brühwiler, D. C. Mancini, L. S. O. Johansson, and N. Mârtensson. Scanning tunneling microscopy of C60/Al(111)-6x6: Inequivalent molecular sites and electronic structure. *Physical Review B*, 54: (1996), 472–475

[85] M. Riede, T. Mueller, W. Tress, R. Schueppel, and K. Leo. Small-molecule solar cells - status and perspectives. *Nanotechnology*, 19: (2008), 424001. ISSN 0957-4484. doi:10.1088/0957-4484/19/42/424001

Eidesstattliche Erklärung

Ich erkläre an Eides statt, dass ich die vorliegende Disseration selbstständig und ohne fremde Hilfe verfasst, andere als die angegebenen Quellen und Hilfsmittel nicht benutzt bzw. die wörtlich oder sinngemäß entnommenen Stellen als solche kenntlich gemacht habe.

Linz, im Mai 2011

Philipp Stadler